

University of Windsor

Scholarship at UWindor

Electronic Theses and Dissertations

Theses, Dissertations, and Major Papers

10-5-2017

Engineering Flow Turbulence for Transport Enhancement

Hao Wu

University of Windsor

Follow this and additional works at: <https://scholar.uwindsor.ca/etd>

Recommended Citation

Wu, Hao, "Engineering Flow Turbulence for Transport Enhancement" (2017). *Electronic Theses and Dissertations*. 7306.

<https://scholar.uwindsor.ca/etd/7306>

This online database contains the full-text of PhD dissertations and Masters' theses of University of Windsor students from 1954 forward. These documents are made available for personal study and research purposes only, in accordance with the Canadian Copyright Act and the Creative Commons license—CC BY-NC-ND (Attribution, Non-Commercial, No Derivative Works). Under this license, works must always be attributed to the copyright holder (original author), cannot be used for any commercial purposes, and may not be altered. Any other use would require the permission of the copyright holder. Students may inquire about withdrawing their dissertation and/or thesis from this database. For additional inquiries, please contact the repository administrator via email (scholarship@uwindsor.ca) or by telephone at 519-253-3000ext. 3208.

Engineering Flow Turbulence for Transport Enhancement

By

Hao Wu

A Thesis
Submitted to the Faculty of Graduate Studies
through the Department of Mechanical, Automotive, and Materials Engineering
in Partial Fulfillment of the Requirements for
the Degree of Master of Applied Science
at the University of Windsor

Windsor, Ontario, Canada

2017

© 2017 Hao Wu

Engineering Flow Turbulence for Transport Enhancement

by

Hao Wu

APPROVED BY:

R. Carriveau

Department of Civil and Environmental Engineering

V. Stoilov

Department of Mechanical, Automotive, & Materials Engineering

S. Ray, Industrial Advisor

Essex Energy Corporation

D. S-K. Ting, Advisor

Department of Mechanical, Automotive, & Materials Engineering

August 10, 2017

DECLARATION OF CO-AUTHORSHIP/PREVIOUS PUBLICATION

This thesis includes 4 original papers that have been co-authored and previously published/submitted for publication in peer reviewed journals/conferences, as follows:

Thesis Chapter	Publication title/full citation	Publication status*
<i>Chapter 2</i>	H. Wu, D. S-K. Ting, S. Ray., Climate change and solar energy opportunities, in: Proc. Energy Nat. Resour., Windsor, 2017	<i>Presented</i>
<i>Chapter 3</i>	H. Wu, D. S-K. Ting, S. Ray., An experimental study of turbulent flow behind a delta winglet, Exp. Therm. Fluid Sci., 88 (2017) pp. 46-54	<i>Published</i>
<i>Chapter 4</i>	H. Wu, D. S-K. Ting, S. Ray., Flow over a flat surface behind delta winglets of varying aspect ratios.	<i>To be submitted</i>
<i>Chapter 5</i>	H. Wu, D. S-K. Ting, S. Ray., The effect of delta winglet attack angle on the heat transfer from a flat surface, Int. J. Heat Mass Transf.	<i>Under review</i>

I certify that I have obtained a written permission from the copyright owner(s) to include the above published material(s) in my thesis. I certify that the above material describes work completed during my registration as graduate student at the University of Windsor.

I declare that, to the best of my knowledge, my thesis does not infringe upon anyone's copyright nor violate any proprietary rights and that any ideas, techniques, quotations, or any other material from the work of other people included in my thesis, published or otherwise, are fully acknowledged in accordance with the standard referencing practices. Furthermore, to the extent that I have included copyrighted material that surpasses the bounds of fair dealing within the meaning of the Canada Copyright Act, I certify that I

have obtained a written permission from the copyright owner(s) to include such material(s) in my thesis.

I declare that this is a true copy of my thesis, including any final revisions, as approved by my thesis committee and the Graduate Studies office, and that this thesis has not been submitted for a higher degree to any other University or Institution.

ABSTRACT

The cooling of solar photovoltaic panels is not only critical, due to the dropping of cell efficiency with the increased temperature, but also challenging, since the heat transfer enhancement must be accomplished without blocking the sun radiation. Longitudinal vortices can be generated by small geometries and last a long distance, thus it is suitable to be applied on solar photovoltaic panels. Delta winglet is one of the most effective longitudinal vortex generators. This work presents four papers, one on the importance of cooling solar panels and three on the investigations and optimizations of the delta winglet. In the first paper, the mitigation effect by solar panels on climate change, as well as the possible beneficial outcomes by employing turbulence generators is discussed. The second paper studies the flow structure of the longitudinal vortex generated by a delta winglet with an aspect ratio of 2 and an attack angle of 30 degrees. It is followed by a paper that investigates the influence of aspect ratio on the flow behavior, and its effect on heat transfer is studied in Appendix A. The final paper presents the impact of attack angle on the heat transfer and correlates the heat transfer with the flow parameters.

DEDICATION

To my family

ACKNOWLEDGEMENTS

I would like first to sincerely thank my advisor Dr. David S.-K. Ting for his supervision and valuable suggestions that guided me in this research for my MA.Sc. at University of Windsor. I would like to thank Mr. Steve Ray for his contributions and support. I would also like to thank Dr. Rupp Carriveau and Dr. Vesselin Stoilov for providing their time and knowledge to keep me on track in my Master's project. As well, I would like to thank Mr. Andy Jenner and Mr. Bruce Durfy for their technical assistance.

This work was made possible by Natural Sciences and Engineering Research Council of Canada and Ontario Centres of Excellence.

TABLE OF CONTENTS

DECLARATION OF CO-AUTHORSHIP/PREVIOUS PUBLICATIONIII

ABSTRACT..... V

DEDICATION..... VI

ACKNOWLEDGEMENTS VII

LIST OF TABLES XI

LIST OF FIGURES XII

CHAPTER 1 INTRODUCTION 1

 1.1 Motivation and Background.....1

 1.2 Thesis Objective and Overview2

 References4

CHAPTER 2 CLIMATE CHANGE AND SOLAR ENERGY OPPORTUNITIES6

 Nomenclature6

 2.1 Introduction7

 2.2 Climate Change Mitigation via Solar Energy8

 2.3 Impact of Climate Change on Solar Energy.....15

 2.4 Conclusion.....19

 Acknowledgments19

 References19

CHAPTER 3 AN EXPERIMENTAL STUDY OF TURBULENT FLOW BEHIND A DELTA WINGLET23

 3.1 Introduction23

 3.2 Experimentation27

 3.3 Data Processing and Uncertainty analysis28

 3.4 Results and Discussion.....31

 3.4.1 Velocity Profile.....31

3.4.2	Turbulence Intensity	38
3.4.3	Turbulence Length Scales.....	42
3.5	Conclusion.....	47
	Acknowledgments.....	48
	References	48
CHAPTER 4 FLOW OVER A FLAT SURFACE BEHIND DELTA WINGLETS OF VARYING ASPECT RATIOS.....		52
4.1	Introduction	52
4.2	Experimentation	54
4.3	Data Processes.....	55
4.4	Results and Discussion.....	58
4.4.1	Time-Averaged Velocity	58
4.4.2	Vortex Structure.....	65
4.4.3	Turbulent Parameters.....	70
4.5	Conclusion.....	81
	Acknowledgments.....	82
	Reference.....	82
CHAPTER 5 THE EFFECT OF DELTA WINGLET ATTACK ANGLE ON THE HEAT TRANSFER PERFORMANCE OF A FLAT SURFACE		84
5.1	Introduction	84
5.2	Experimentation	87
5.3	Data Processes.....	89
5.4	Results	90
5.5	Conclusion.....	107
	Acknowledgments.....	108
	Reference.....	108

CHAPTER 6 CONCLUSIONS	113
7.1 Summary and Conclusions.....	113
7.2 Recommendations	114
APPENDICES	116
Appendix A. The Effect of Aspect Ratio on Heat Transfer.	116
Appendix B. Permissions for Previously Published Works	123
VITA AUCTORIS	124

LIST OF TABLES

Table 1. 1 Parameters of ClearPower CS6P-230P solar panel.	12
Table 5. 1 Boundary conditions for regression.	102

LIST OF FIGURES

Figure 2. 1 Three types of solar electricity generators; PV = photovoltaic, TPV = thermophotovoltaic, CSP = concentrated solar power.	9
Figure 2. 2 Cell temperature and efficiency estimation based on the weather data in Detroit, Michigan for TMY (typical meteorological year).	12
Figure 2. 3 Cell temperature and efficiency with and without TGs.....	13
Figure 2. 4 Solar energy output with and without TGs.....	13
Figure 2. 5 Efficiency enhancement and energy enhancement.....	14
Figure 2. 6 Solar irradiance and efficiency enhancement signal in January.....	15
Figure 2. 7 Cell temperature and efficiency with climate change.	17
Figure 2. 8 Change in energy conversion efficiency caused by different factors.	17
Figure 2. 9 Energy output for unit area solar panel.	18
Figure 2. 10 Change in energy output caused by different factors.	18
Figure 3. 1 Typical vortex generators. α is the angle of attack, c is the chord length, h is the winglet height, and b is the span or width.	27
Figure 3. 2 The experimental setup inside a wind tunnel. The $\delta = 1$ mm winglet is fixed at $1c$ from leading edge, $\alpha = 30^\circ$, $h = 10$ mm, $c = 20$ mm, hot wire at $10h$ downstream of the winglet.	28
Figure 3. 3 Cross-stream velocity vector at 10 winglet heights downstream of the delta winglet.	33
Figure 3. 4 Mean flow angle (degrees) at 10 winglet heights downstream of the delta winglet.	33
Figure 3. 5 Nondimensional vorticity Ω at 10 winglet heights downstream of the delta winglet.	35

Figure 3. 6 The sum of normalized W velocity for each y position at 10 winglet heights downstream of the delta winglet.....	36
Figure 3. 7 Streamwise velocity \bar{U}/U_∞ of inflow, outflow, and the base flat plate case without the winglet, at 10 winglet heights downstream of the delta winglet.	37
Figure 3. 8 Streamwise velocity \bar{U}/U_∞ profile at 10 winglet heights downstream of the delta winglet.	38
Figure 3. 9 Turbulence intensity $u(v,w)_{rms}/U_\infty$ of inflow, outflow, and the base flat plate case without the winglet, at 10 winglet heights downstream of the delta winglet. .	40
Figure 3. 10 Turbulence intensity (u_{rms}/U_∞) profile at 10 winglet heights downstream of the delta winglet.	42
Figure 3. 11 Power spectral densities for point $Y/h = 2.4$ and $Z/h = 1.6$ at 10 winglet heights downstream of the delta winglet.	43
Figure 3. 12 Power spectral densities for point $Y/h = 2.8$ and $Z/h = 0.6$ at 10 winglet heights downstream of the delta winglet.	44
Figure 3. 13 Integral length scale (normalized by h) for u component at 10 winglet heights downstream of the delta winglet.	45
Figure 3. 14 Taylor microscale (normalized by h) for u component of inflow, outflow, and the base flat plate case without the winglet, at 10 winglet heights downstream of the delta winglet.	46
Figure 3. 15 Taylor microscale (normalized by h) for u component at 10 winglet heights downstream of the delta winglet.....	47
Figure 4. 1 Typical vortex generators.	54
Figure 4. 2 The experimental setup inside a wind tunnel and the sketch of the winglet. $\delta = 0.1$ mm, $\alpha = 30^\circ$, $h = 10$ mm, $c = 10, 20, 40$ mm.	55

Figure 4. 3 Normalized streamwise time-averaged velocity contours and cross-stream velocity vectors at AR = 1, 2 and 4.	61
Figure 4. 4 Normalized streamwise velocity at peak deficit locations with respect to aspect ratio.	61
Figure 4. 5 Sum of normalized W velocities at AR = 1, 2 and 4.	63
Figure 4. 6 Normalized streamwise velocities for Inflow and Outflow at AR = 1, 2 and 4. (a) Inflow, (b) Outflow, (c) Inflow and Outflow.	64
Figure 4. 7 Cross-stream velocity vector and dimensionless vorticity contour at AR = 1, 2 and 4.	67
Figure 4. 8 Mean flow angle (between mean flow and streamwise, in degree) contour and cross-stream velocity vector at AR = 1, 2 and 4.	69
Figure 4. 9 Peak mean flow angle (between mean flow and streamwise) and peak vorticity with respect to aspect ratio.	69
Figure 4. 10 The main vortex core locations with respect to aspect ratio.	70
Figure 4. 11 Stream-wise turbulence intensity (u_{rms}/U_{∞}) contour and cross-stream velocity vector at AR = 1, 2 and 4.	72
Figure 4. 12 Stream-wise turbulence intensity for Inflow and Outflow at AR = 1, 2 and 4. (a) Inflow, (b) Outflow, (c) Inflow and Outflow.	74
Figure 4. 13 Stream-wise Taylor microscale (normalized by h) contour and cross-stream velocity vector at AR = 1, 2 and 4.	76
Figure 4. 14 Stream-wise turbulence intensity and Taylor microscale at the main vortex core with respect to aspect ratio.	76
Figure 4. 15 Stream-wise Taylor microscale (normalized by h) for Inflow and Outflow at AR = 1, 2 and 4.	79

Figure 4. 16 Stream-wise integral length scale contour and cross-stream velocity vector.	81
Figure 5. 1 Delta winglet vortex generator.	87
Figure 5. 2 A schematic of the winglet and the experimental setup inside the wind tunnel. t = 0.1 mm; $\alpha = 30^\circ, 45^\circ, 60^\circ$; h = 10 mm; c = 20 mm.	88
Figure 5. 3 Variation of normalized Nusselt number profile with attack angle. (a) 30 degrees, (b) 45 degrees, (c) 60 degrees.	92
Figure 5. 4 Maximum and minimum local normalized Nusselt number for attack angles of 30, 45 and 60 degrees with respect to downstream distance.....	93
Figure 5. 5 The normalized Nusselt number for attack angles of 30, 45 and 60 degrees at downstream distance of (a) 3h, (b) 20h.	95
Figure 5. 6 Dimensionless vorticity contour and cross-stream velocity vector for attack angles of (a) 30, (b) 45, (c) 60 degrees.....	97
Figure 5. 7 Normalized streamwise time-averaged velocity contours and cross-stream velocity vectors for attack angles of (a) 30, (b) 45, (c) 60 degrees.	99
Figure 5. 8 Normalized total turbulence fluctuation (q^2/U_∞^2) contour and cross-stream velocity vector for attack angles of (a) 30, (b) 45, (c) 60 degrees.....	100
Figure 5. 9 The multiple regression results. Lines signify fitted curves, and symbols are measured data.	103
Figure 5. 10 The impact of individual fluid parameters on the heat transfer rate. (a) W/U_∞ , (b) $(\delta - \delta_0)/\delta_0$, (c) $U_{0.4}/U_\infty$, (d) q^2/U_∞^2	106
Figure A. 1 Variation of normalized Nusselt number profile with aspect ratio. (a) AR = 1, (b) AR = 2, (c) AR = 4.	117
Figure A. 2 Maximum and minimum local normalized Nusselt number for aspect ratio of 1, 2 and 4 with respect to downstream distance.	118

Figure A. 3 The normalized Nusselt number for aspect ratios of 1, 2 and 4 at downstream distance of $10h$	119
Figure A. 4 Comparison between calculated and measured Nusselt number. Lines signify calculated curves based on the data in chapter 4, and symbols are measured data.	120
Figure A. 5 The impact of each factor on heat transfer for varying aspect ratio. (a) W/U_∞ , (b) $(\delta - \delta_0)/\delta_0$, (c) $U_{0.4}/U_\infty$, (d) q^2/U_∞^2	122

CHAPTER 1

INTRODUCTION

1.1 Motivation and Background

There are many applications where the effectiveness of convective heat transfer by air is important. Many measures have been propounded and investigated to enhance the convective heat transfer. They can be classified as active, passive or compound [1]. Active methods such as electric or acoustic fields, surface vibration, or mechanical devices require external power to accomplish enhancement, while passive methods promote the heat transfer by making use of a special surface geometry to manipulate the flow. Main flow alteration is one way to manipulate the flow, which includes wavy fins, louvered fins and furrowed channels[2]. The other one is to intentionally introduce secondary flow, like vortices.

Recently, one special issue has started to attract people's attention, the cooling of solar photovoltaic panels. The heat transfer enhancement must be achieved without blocking the solar radiation, thus the surface geometries cannot be applied on the PV panel surface, but only on the border. This situation requires the heat transfer enhancement must be long lasting. Longitudinal vortex is one of the most long-lasting secondary flow inducing measures. Compared with transverse vortex which has its rotating axis normal to the main flow direction, the longitudinal vortex has the rotation axis parallel to the main flow, thus it can be carried farther downstream without significantly decaying. Furthermore, longitudinal vortex shows less flow loss and better heat transfer characteristics than transverse vortices [3,4].

Delta winglet has posted itself as potentially the best longitudinal vortex generator with simple geometry in several comparison studies [3,5–7]. Most of the studies on delta winglet were conducted in a confined flow. To marry the delta winglet with the PV panel, and also better understand the generated longitudinal vortex in a fundamental view, the investigation on the unconfined flat surface must be conducted.

1.2 Thesis Objective and Overview

The objective of the current study is to investigate the wake properties and heat transfer enhancement of a delta winglet in unconfined flow with varying aspect ratios and attack angles. The flow was measured by the triple probe hot-wire anemometer system. Heat transfer measurement was by an infrared thermal camera. Different steps of this research work are explained in the chapters of this dissertation, as follows:

Chapter 1 (Introduction)

The background, objective and an overview of the thesis are given.

Chapter 2

This chapter estimates the possible efficiency boost and energy output augmentation impacts via applying turbulence generators on solar PV by calculating the solar panel efficiency and energy output based on the weather data in Detroit, Michigan, USA. The mitigation impacts of solar energy on climate change and the interplay of climate change on solar PV are investigated. The demand of increasing the cell efficiency due to the total output power decline caused by climate change is brought out.

Chapter 3

In this chapter, the vortical turbulent flow generated by a 10 mm high and 20 mm long delta winglet on a flat surface with an attack angle of 30 degrees is experimentally studied in a wind tunnel. The flow field at 10 winglet heights downstream is measured using a triple wire probe at a Reynolds number of 5000, based on winglet height. Main vortex and induced vortex structures are identified in the form of the cross-stream velocity vector and the vorticity contour. Boundary layer thickness, streamwise velocity distribution, turbulence intensity and Taylor microscale are compared at the inflow and outflow regions as well as in the base flat plate case. The inflow region is postulated to have a larger potential for heat convection; since the vortex penetrated into the boundary layer, the boundary layer thickness increased, while maintaining high turbulence intensity. At the core of both the main vortex and the induced vortex, both the streamwise velocity deficit and the turbulent intensity are enhanced.

Chapter 4

As the next step, the winglets with aspect ratios of 1, 2 and 4 are considered at a Reynolds number based on winglet height of 6000 and an angle of attack of 30 degrees. The streamwise velocity deficit at the main vortex core decreases, while that at the upwash region remains unaltered, with increasing aspect ratio. Moreover, the vortex moves downward and inward and its intensity decreases. The turbulence level decreases with a corresponding increase in Taylor microscale. The integral length is found to be independent of the aspect ratio but scales with the winglet height.

Chapter 5

A new setup is designed and constructed to study the heat transfer effect of delta winglet. The winglet is placed on a flat plate, whose bottom side is uniformly heated by condensing steam at 100°C. The results deduced from thermal imaging indicated that the peak Nusselt number (Nu) increases with the attack angle, and this augmentation can be attributed to the larger share of transverse vortex at larger attack angle. Peak Nu drops sharply in the near downstream. It subsequently decreases more gradually and becomes less sensitive to attack angle farther downstream. This extended heat transfer enhancement is hypothesized to be caused by the longitudinal vortices, which, though decaying but rather slowly and thus, remained over the extent of the studied distance. This prevailing longitudinal vortex induced heat transfer enhancement is explained in terms of the detailed flow characteristics scrutinized via a triple hot wire at 20h. The cooler air brought, by the longitudinal vortex, into the hot plate at Inflow corresponds to the maximum Nu boost, while the outgoing heated air, after ‘hanging out’ near the hot surface, at Outflow correlated with the Nu valley, the small region where the heat transfer is lower than the reference flat plate without the winglet case. Further analysis related the variations in heat transfer with the local near-surface streamwise velocity, out-plane velocity, and turbulence intensity. The specific heat-flow correlations subtly differed between the Inflow and Outflow regions, and thus, the effect of the winglet attack angle.

Chapter 6 (Conclusion)

The final chapter synthesizes the work in previous chapters and summarizes the heat transfer enhancement performance by delta winglet. It also tries to develop some strategies for next steps.

Appendix A.

This section studies the effect of aspect ratio on heat transfer enhancement, to accomplish the study in Chapter 4. The flow measurement data in Chapter 4 was put into the regression results obtained from the data in Chapter 5, for both validation purposes and to better understand how aspect ratio affects the heat transfer by altering the flow structure.

Appendix B.

The written permission from the copyright owner to include the paper in chapter 3 in this thesis is given.

References

- [1] R. Webb, Principles of enhanced heat transfer, 1994, John Wiley&Sons, New York. (1994). doi:10.1016/0140-7007(95)90013-6.
- [2] A.M. Jacobi, R.K. Shah, Heat transfer surface enhancement through the use of longitudinal vortices : A review of recent progress, Exp. Therm. Fluid Sci. 11 (1995) 295–309.
- [3] M. Fiebig, Embedded vortices in internal flow: heat transfer and pressure loss enhancement, Int. J. Heat Fluid Flow. 16 (1995) 376–388. doi:10.1016/0142-727X(95)00043-P.
- [4] M. Henze, J. von Wolfersdorf, B. Weigand, C.F. Dietz, S.O. Neumann, Flow and heat transfer characteristics behind vortex generators - A benchmark dataset, Int. J. Heat Fluid Flow. 32 (2011) 318–328. doi:10.1016/j.ijheatfluidflow.2010.07.005.

- [5] F. Edwards, C. Alker, N. Crompton, The improvement of forced convection surface heat transfer using surface protrusions in the form of (A) Cubes and (B) Vortex generators, in: Proc. 5th Int. Heat Transf. Conf., 1974: pp. 244–248.
- [6] G. Zhou, Q. Ye, Experimental investigations of thermal and flow characteristics of curved trapezoidal winglet type vortex generators, Appl. Therm. Eng. 37 (2012) 241–248. doi:10.1016/j.applthermaleng.2011.11.024.
- [7] L.T. Tian, Y.L. He, Y.G. Lei, W.Q. Tao, Numerical study of fluid flow and heat transfer in a flat-plate channel with longitudinal vortex generators by applying field synergy principle analysis, Int. Commun. Heat Mass Transf. 36 (2009) 111–120. doi:10.1016/j.icheatmasstransfer.2008.10.018.

CHAPTER 2

CLIMATE CHANGE AND SOLAR ENERGY OPPORTUNITIES

Hao Wu[†], David S-K. Ting

Turbulence and Energy laboratory, University of Windsor

401 Sunset Avenue, Windsor, ON, N9B 3P4, Canada

Steve Ray

Essex Energy Corporation

2199 Blackacre Drive, Suite #2, Oldcastle, ON, N0R 1L0, Canada

H. Wu, D. S-K. Ting, S. Ray., Climate change and solar energy opportunities, in: Proc. Energy Nat. Resour., Windsor, 2017

Nomenclature

A	Solar panel area
B	Temperature coefficient
C	Solar irradiance coefficient
DHI	Diffuse horizontal irradiance
DNI	Direct normal irradiance
E	Electric energy output
GHI	Global horizontal irradiance
G_T	Global tilted irradiance
$G_{T,ref}$	Reference solar irradiance
$G_{T,NOCT}$	Solar irradiance at the NOCT
$h_{conductive}$	Heat conductive coefficient
$h_{convective}$	Heat convective coefficient
n	Day of year
NOCT	Nominal operation cell temperature
$q_{radiation}$	Radiation heat transfer
t	Operation time
T_a	Air temperature
T_c	Cell temperature

$T_{a,NOCT}$	Air temperature at the NOCT
T_{ref}	Reference temperature
$U_{L,NOCT}$	Thermal loss coefficient at the NOCT
U_L	Thermal loss coefficient of the solar panel
V	Wind speed
α	Solar absorptance coefficient of the PV layer
β	Tilt angle
γ	Surface azimuth angle
δ	Declination
η	Cell efficiency
η_{ref}	Cell efficiency at reference temperature
θ	Tilt incidence angle
ρ	Ground reflectance
τ	Solar transmittance coefficient of glazing
ϕ	Latitude
ω	Hour angle

2.1 Introduction

Most of the energy consumed by human beings has its origin in fossil fuels. Fossil fuel energy resources are non-renewable and will be exhausted in the next centuries. Furthermore, these fuels discharge greenhouse gas which contributes to global climate change [1, 2]. To simultaneously mitigate climate change and satisfy the growing energy demand, renewable energy is expected to play a greater role in future energy provision. As the most abundantly available energy source, solar power is attracting progressively more attention. 86,000 TW ($1 \text{ TW} = 10^{12} \text{ Js}^{-1}$) of solar energy reaches the Earth's surface [3, 4], while the averaged global energy consumption was just about 17.5 TW in 2010 [5]. Therefore, only harvesting a small portion of the total solar potential would provide sufficient energy for all human needs.

Most solar energy that is harnessed is converted to electricity via solar panels or wind turbines (as we know the wind is generated by the pressure gradient caused by uneven

sun heating). Renewable energy provided 23.7% of the global overall electricity generation in 2015; including 3.7% (433 GW) of wind energy and 1.2% (227 GW) of solar PV [6].

Replacing fossil fuels in our transportation system with electric batteries can lead to significant greenhouse gas reductions and energy savings through increased efficiency. The current 'tank-to-wheel' system of internal combustion engine driven vehicles has an efficiency of approximately 25%. The efficiency of electric battery driven vehicles can reach 90% [7, 8]. For the heavy equipment such as trucks and ships, if we replace typical engines with hydrogen-powered fuel cells with hydrogen produced from electricity, the chain efficiency is assessed at 65% [9-12], more than twice the engine efficiency. Therefore, the energy demand in transportation would be at least halved if the power source is replaced by electricity.

Hu et al. [13] estimated the total power demand in 2100 will be 63 TW. If the energy supply in all sectors (including transportation, building and industry) were to be replaced by electricity (moving away from fossil fuels), the total energy demand could be reduced to 45 TW. Hu et al. [13] also simulated the condition where all urban areas are covered with solar panels. The total power production by solar panels would be 48 ± 1 TW. They suggested that solar power has the potential to satisfy all human demand.

In short, solar power is a potential candidate for future low-carbon energy supply system and climate change mitigation. Solar power, in turn, depends on weather and climate. In the present study, the climate change mitigation by solar energy and the impact of climate change on solar energy are analysed.

2.2 Climate Change Mitigation via Solar Energy

When in operation, both solar panels and wind turbines discharge no greenhouse gas emissions. According to the lifecycle greenhouse gas emission estimates for electricity generators [14], solar panels only discharge 32 g CO₂ per kWh, and for wind this value is 10. Compared with the electricity from coal, whose emission is 1050 g CO₂/kWh, the

existing installed level is reducing 3.94×10^9 tonnes CO₂ for wind, and 2.02×10^9 tonnes for solar panels.

Depending on how electricity is generated from solar energy, there are three major types of solar panels, as shown in Figure 2.1: solar photovoltaic (PV), solar thermophotovoltaic (TPV), and concentrated solar power (CSP). For the PV panels, the solar power knocks loose the electrons in the panels to create electricity flows. TPV generate electricity by converting Infrared Ray directly into electricity via photons. It requires absorbers and selective emitters to convert solar radiance into the working spectrum range. CSP concentrates the solar power via mirrors and lenses to a receiver which produces steam for a turbine to generate electricity [13]. As the solar radiation is exposed to the solar panels, a part of the solar energy is converted into electricity, and the rest is transmitted through the panels and eventually absorbed or reflected by the Earth surface. The efficiency of solar panels ranges from 5% to 40% [15,16]. Due to the better cost performance, solar PV is the most commonly type of solar electricity generators [6].

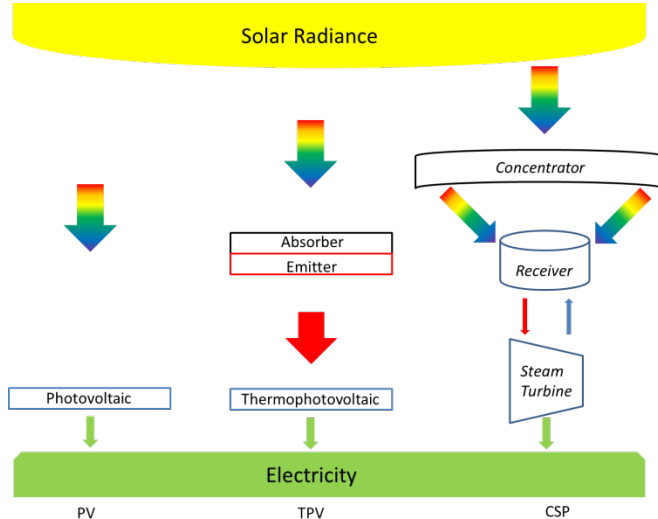


Figure 2. 1 Three types of solar electricity generators; PV = photovoltaic, TPV = thermophotovoltaic, CSP = concentrated solar power.

When the solar radiation reaches the Earth’s surface, it is either absorbed or reflected, and the Earth’s surface and near-ground air is heated. With the introduction of solar panels, the solar energy is redistributed, i.e., a portion of the solar radiation is absorbed by solar

panels and diverted to electricity generation. This would have a cooling effect on the area where the solar panels are installed; e.g., less solar heat is passed through the roof and makes its way into the building.

The solar panel exposed to sun radiation would also be heated up by the transmitted part of radiation. At the same time the solar panel is cooled by natural heat transfer with its surroundings. This heat transfer consists of convection and radiation from two sides of the solar panel and conduction through the frame. The heat transfer is negatively correlated with the ambient (convection) and sky (radiation) temperatures, and is positively correlated with wind speed and turbulence levels [17]. Therefore turbulence generators (TGs) have been applied to cool solar panels which enhance the irradiance-electricity conversion efficiency. With turbulence generated using large vortex structures, convective heat transfer can be enhanced by several times, depending on the method and Reynolds number. For the heat transfer from a flat plate (surrogate solar panels), the overall enhancement by TGs is usually no more than 100% [18-20].

The cell temperature and efficiency can be estimated based on solar irradiance, ambient temperature and wind speed. The cell efficiency can be calculated from [21]:

$$\eta = \eta_{ref} \left[1 - B(T_c - T_{ref}) + C \text{Log} \frac{G_T}{G_{T,ref}} \right] \quad (2.1)$$

where η_{ref} is the cell efficiency at the reference temperature (T_{ref}) and reference solar irradiance ($G_{T,ref}$). T_c is the cell temperature. G_T is the solar irradiance. B and C are the temperature coefficient and solar irradiance coefficient, respectively. The value of C is often assumed to be zero [22], therefore this question can be simplified into:

$$\eta = \eta_{ref} [1 - B(T_c - T_{ref})] \quad (2.2)$$

The cell temperature can be estimated by [23]:

$$T_c = T_a + (NOCT - T_{a,NOCT}) \left(\frac{G_T}{G_{T,NOCT}} \right) \left(\frac{U_L NOCT}{U_L} \right) \left(1 - \frac{\eta}{\tau \alpha} \right) \quad (2.3)$$

where T_a is the air temperature, U_L is the thermal loss coefficient of the solar panel. NOCT is the Nominal Operation Cell Temperature, which is the cell temperature in a standard reference environment, the panel is tilted 45 degrees from the horizontal under an open circuit condition, the solar radiation is 800 W/m², the air temperature is 20 °C,

and the wind speed is 1 m/s [24]. $T_{a,NOCT}$, $G_{T,NOCT}$ and $U_{L,NOCT}$ are the air temperature, solar irradiance and thermal loss coefficient at the Nominal Operation Cell Temperature, respectively. τ is the solar transmittance coefficient of glazing. α is the solar absorptance coefficient of the PV layer. According to Duffie and Beckman [23], the term $(\frac{\eta_e}{\tau\alpha})$ is negligible. The heat loss coefficient for the solar panel U_L can be expressed as:

$$U_L = h_{conductive} + h_{convective} + \frac{q_{radiation}}{T_c - T_a} \quad (2.4)$$

Fouladi et al. [17] found that the conductive and radiance heat transfer is typically small compared to convective heat transfer, therefore they can be ignored. According to Sharples and Charlesworth [25], the convective heat loss coefficient for a flat plate solar panel mounted on a roof can be estimated by:

$$h_{convective} = 3.3V + 6.5 \quad (2.5)$$

where V is the wind speed. Equation 2.3 can be rewritten as:

$$T_c = T_a + (NOCT - 20) \left(\frac{G_T}{800} \right) \left(\frac{9.8}{3.3V + 6.5} \right) \quad (2.6)$$

The electric energy output can be calculated by:

$$E = \eta G_T A t \quad (2.7)$$

where A is the solar panel area and t is the operation time.

In order to have a concrete idea of how the solar panel works and how TGs can enhance the energy output, the performance of a typical solar panel ClearPower CS6P-230P (Canadian Solar, Guelph, Ontario, Canada; Parameters in Table 1) under the weather condition in Detroit, Michigan, USA is calculated following Equations 2.2, 2.6 and 2.7. The weather data is obtained from National Solar Radiation Database [26], including the GHI, DNI and DHI, temperature T_a and wind speed V in TMY (typical meteorological year) with an interval of one hour. The Solar irradiance G_T on solar panel with tilt angle of 45 degrees (to be consistent with NOCT condition) is derived from Duffie and Beckman [23]:

$$G_T = DNI \cos \theta + DHI \left(\frac{1 + \cos \beta}{2} \right) + GHI \rho \left(\frac{1 - \cos \beta}{2} \right) \quad (2.8)$$

where β is the tilt angle, ρ is the ground reflectance (normally around 0.2), θ is the tilt incidence angle, derived from:

$$\cos \theta = \sin \delta \sin \phi \cos \beta - \sin \delta \cos \phi \sin \beta \cos \gamma + \cos \delta \cos \phi \cos \beta \cos \omega$$

$$+ \cos\delta \sin\phi \sin\beta \cos\gamma \cos\omega + \cos\delta \sin\beta \sin\gamma \sin\omega \quad (2.9)$$

where ϕ is the latitude (42°), γ is the surface azimuth angle (which is zero for the south facing solar panel in the current study), ω is the hour angle, and δ is the declination, derived from:

$$\delta = 23.45 \sin\left(360 \frac{284+n}{365}\right) \quad (2.10)$$

where n is the day of year.

Table 1. 1 Parameters of ClearPower CS6P-230P solar panel.

η_{ref}	T_{ref}	$G_{T,ref}$	B	$NOCT$
14.3%	25 °C	1000 W/m ²	0.43%	45 °C

Figure 2.2 shows the calculated cell temperature and efficiency with an interval of one hour as well as the month averaged value. The deviation between estimation and real data is reported to be less than 1.6 % for this method [17]. The data which has a zero GHI solar irradiance (in the nights or during cloudy days) is removed since there is no solar energy input and the solar panel is not in operation. As expected, the cell temperature peaked in the summer, along with a trough in efficiency.

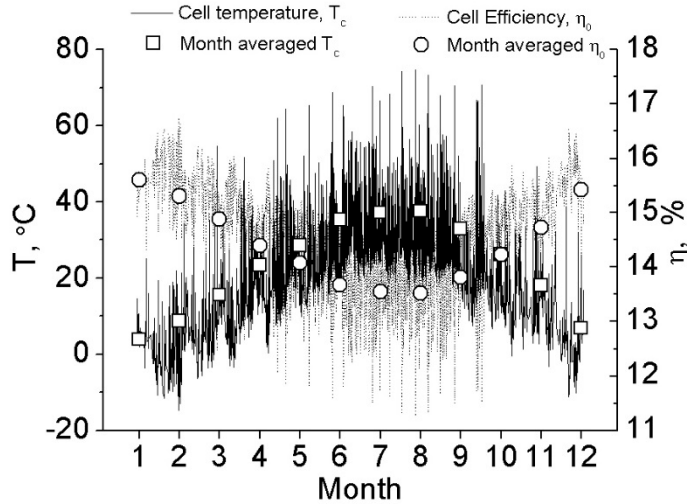


Figure 2. 2 Cell temperature and efficiency estimation based on the weather data in Detroit, Michigan for TMY (typical meteorological year).

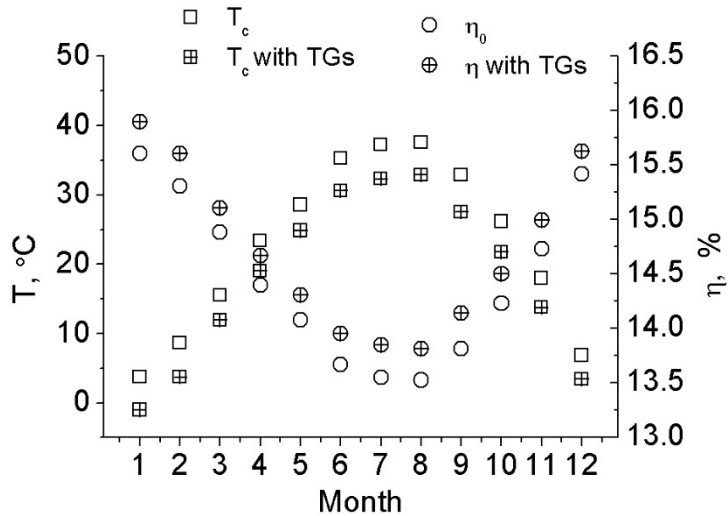


Figure 2. 3 Cell temperature and efficiency with and without TGs.

Assuming the heat transfer can be doubled when employing some effective turbulence generators, the cell temperature and efficiency are shown in Figure 2.3. As we can see, in the presence of TGs the cell temperature would be lowered, and the cell efficiency would be improved. Considering the better solar irradiance condition in the summer time, the actual gain in solar energy should be greater. Figure 2.4 illustrates the solar power output for unit area per month. We can see that most of the solar energy is produced during the summer time. With the TGs, the energy output increased, particularly in the summer where there is an abundant amount of solar energy to harness.

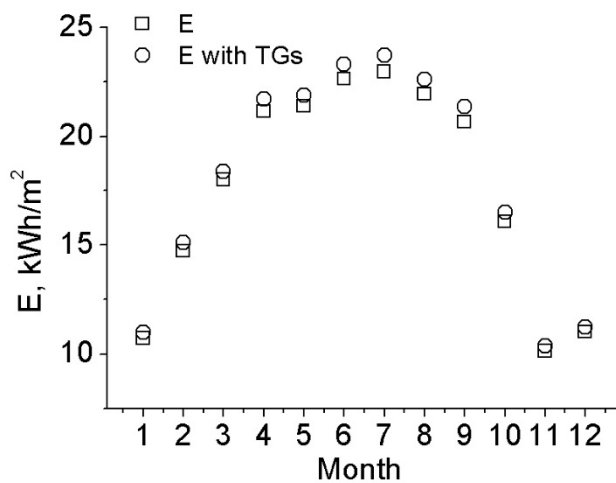


Figure 2. 4 Solar energy output with and without TGs.

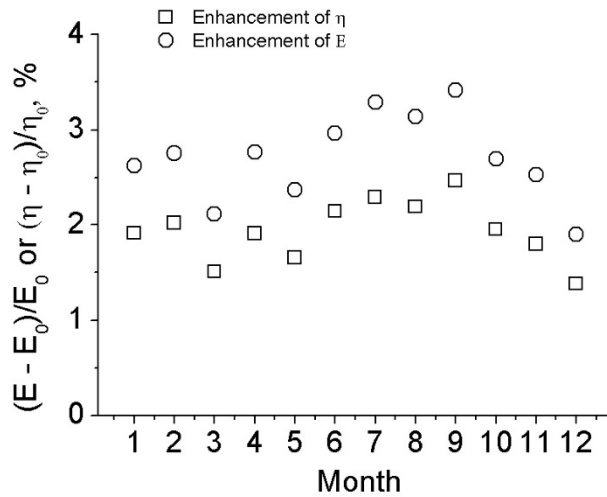


Figure 2. 5 Efficiency enhancement and energy enhancement.

Figure 2.5 compares the enhancement of energy conversion efficiency and solar energy output. They both have the trend of increasing from the beginning of the year, peaking in July-September, and decreasing back to the lowest point in December. However, the enhancement of energy output for each month is significantly larger than that of the conversion efficiency. This can be attributed to the higher efficiency enhancement associated with more intense solar irradiance hours, as shown in Figure 2.6 (only the first 300 hours were shown for clarity purpose). When there is more intense solar irradiance, the heating of the solar panel is more significant and the temperature difference between the solar panel and ambient is larger. With the same heat transfer enhancement, larger temperature differences would lead to larger cooling and consequently, a higher efficiency increase. The sum of products for the synchronous solar irradiance and efficiency would result in a larger percentage energy output enhancement than efficiency enhancement.

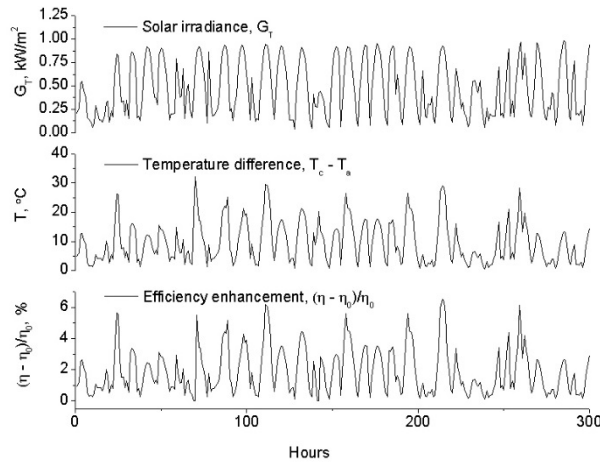


Figure 2. 6 Solar irradiance and efficiency enhancement signal in January.

The total power output of a unit area solar panel in TMY is 200.8 kWh, and with the cooling effect of TGs this value becomes 205.7 kWh, increased by 2.4 %. If we combine this with the current global solar panels installation level, the total power output would increase by 5.45 GW, equivalent to 4.86×10^7 tonnes of CO₂ reduction per year.

2.3 Impact of Climate Change on Solar Energy.

Climate change has the potential to affect the harnessing of solar energy. Climate change could lead to an increase of earth surface temperature of up to 5 degrees by 2100 [27]. With increased ambient temperature, the cell temperature of solar panels will be higher and the efficiency will decrease accordingly. Also, higher temperature leads to a stronger hydrologic cycle and thus increased cloudiness. This would reflect more solar radiation and result in lower irradiant levels.

Climate change can also affect wind conditions. In Breslow and Sailor [28], the simulation results suggest a 1.4 ~ 4.5 % decrease of wind speeds in USA in the next 100 years. The decreasing wind speed would lead to a lower cooling efficiency of solar panels. Assuming the solar irradiance decreases by 5%, wind speed decreases by 4.5% and temperature increases 5 degrees, the cell temperature, energy conversion efficiency and energy output are estimated using the same method in Section 2. Figure 2.7 illustrates the cell temperature and efficiency with the impact of climate change. As expected the cell

temperature increases and efficiency decreases. These changes are almost the same in absolute value throughout the year. Figure 2.8 shows the independent impact of rising air temperature, decreasing solar irradiance and lower wind speed on energy conversion efficiency. The overall change in efficiency is dominated by the declining effect of rising air temperature. The decrease of solar irradiance lead to a slight boost in efficiency, which can be attributed to the lower ambient temperature and lower cell temperature associated with weaker solar irradiance. The impact of wind speed is very small. The average relative efficiency decrease is approximately 2%.

The influence of climate change on solar power output is shown in Figure 2.9. As we can see, with climate change, the power output drops dramatically, particularly in the summer months. The total energy of TMY drops from 200.8 to 186.9 kWh, a decrease of 7%. Figure 2.10 illustrates the effects of each factor. As can be seen, the energy output is mostly influenced by the changes in solar irradiance condition, followed by the ambient air temperature. The effect of decreasing wind speed is negligible. Similar results were reported by Jerez et al. [29]. Their climate change model suggests the solar PV power supply in Europe would decrease in northern Europe and slightly increase in southern Europe by the end of this century. They attribute the changes in solar power mostly to the solar irradiance distribution, i.e., the shortwave radiation is projected to increase in southern Europe and decrease in the north. The negative effect of rising air temperature universally decreases the solar PV power output in all areas. The wind velocity is expected to decrease in most areas; however its impact on solar PV is postulated to be negligible. With the continuing progress in science and technology, the efficiency of solar panels is expected to increase and offset this negative effect of climate change. As illustrated in Figures 2.9 and 2.10, if the efficiency increases by 7% the power output decline caused by climate change would be offset.

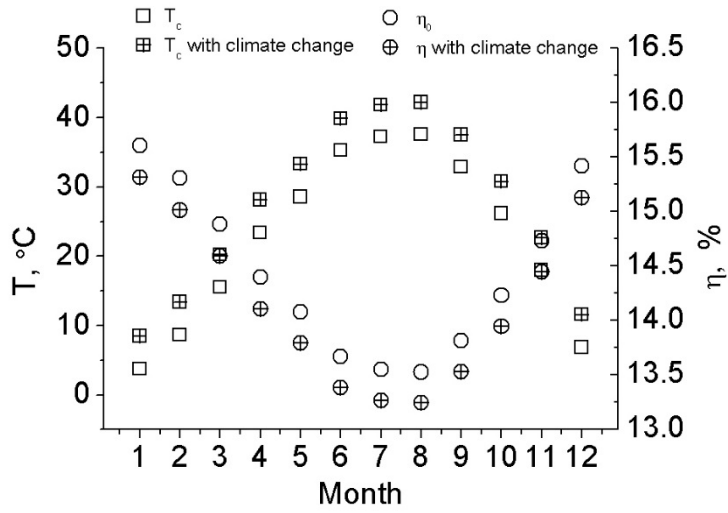


Figure 2. 7 Cell temperature and efficiency with climate change.

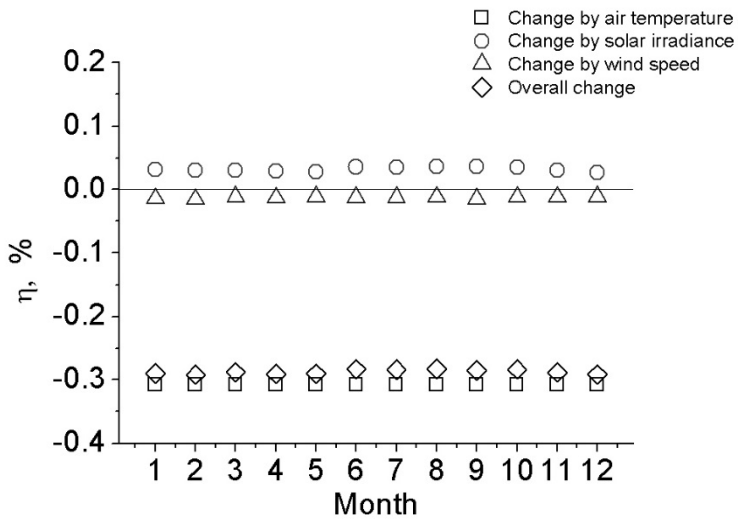


Figure 2. 8 Change in energy conversion efficiency caused by different factors.

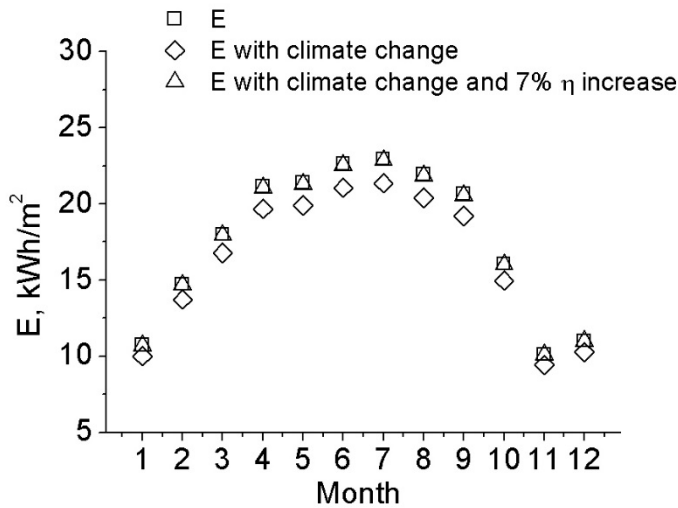


Figure 2.9 Energy output for unit area solar panel.

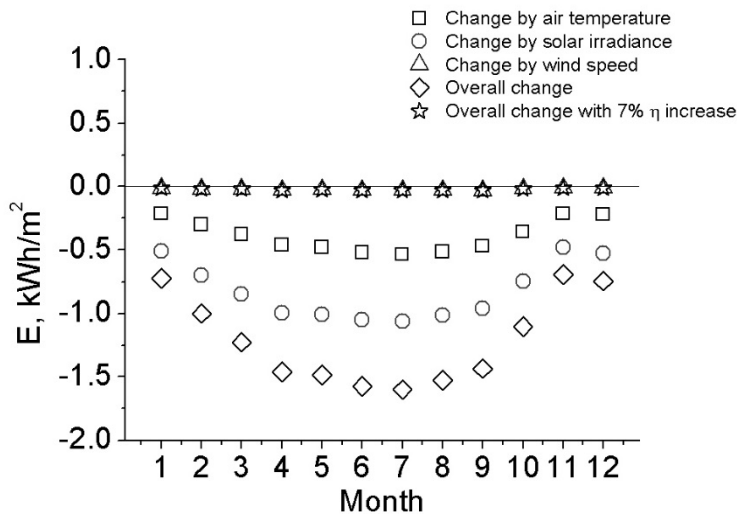


Figure 2.10 Change in energy output caused by different factors.

The climate change impact on another way of harnessing solar power, wind principles, is analyzed by Pryor and Barthelmie [30]. They studied the influence of the wind resource magnitude, extreme wind speeds and gusts, icing, sea ice and permafrost, and other factors such as air density and extreme temperatures. Their simulation results suggest small magnitude changes in the wind resource, extreme wind speeds increases and sea ice and icing frequencies decrease in Europe. They conclude there is no detectable change in the wind conditions that could jeopardize the exploitation of wind energy.

2.4 Conclusion

The mitigation effects of solar energy on climate change are analysed and the equivalent greenhouse emission reduction is estimated. The cell temperature, energy conversion efficiency and power output of typical solar panels are estimated based on the weather condition in Detroit, Michigan, USA. The possible cooling of cell temperature and enhancing of energy conversion efficiency by promoting cell convective heat transfer via turbulence generators is estimated. Larger enhancement in energy output is projected to occur during the summer months. Greater efficiency enhancement is associated with larger temperature difference between solar panels and atmosphere, which is linked to stronger solar irradiance. This synchronous solar irradiance and cell efficiency leads to a greater total power output enhancement compared to the energy conversion efficiency enhancement. The impact of climate change on solar energy harnessing is analysed. The rising atmosphere air temperature is the culprit for the cell efficiency decrease. The cell output power is more sensitive to solar irradiance condition than the ambient temperature.

Acknowledgments

This work was made possible by Natural Sciences and Engineering Research Council of Canada and Ontario Centres of Excellence.

References

- [1] Intergovernmental panel on climate change. (2014). *Climate Change 2014–Impacts, Adaptation and vulnerability: Regional aspects*. Cambridge University Press.
- [2] T. Stocker, (Ed.), *Climate change 2013: The physical science basis: working group I contribution to the fifth assessment report of the intergovernmental panel on climate change*. Cambridge University Press, New York, 2014.
- [3] *International Energy Outlook 2013* DOE/EIA-0484 US Energy Information Administration, US Department of Energy, 2013.
- [4] P. V. Kamat, Meeting the clean energy demand: nanostructure architectures for solar energy conversion. *J. Phys. Chem.* 111 (2007) 2834–2860.
- [5] *Key World Energy Statistics*, International Energy Agency, 2013.
- [6] Ren 21. *Renewables 2016 Global Status Report*.

- [7] J.M. Ogden, M.M. Steinbugler, T.G. Kreutz, A comparison of hydrogen, methanol and gasoline as fuels for fuel cell vehicles: implications for vehicle design and infrastructure development. *J. Power Sources*, 79 (1999) 143-168.
- [8] J.H. Williams, A. DeBenedictis, R. Ghanadan, A. Mahone, J. Moore, W.R. Morrow, S. Price, M.S. Torn, The technology path to deep greenhouse gas emissions cuts by 2050: the pivotal role of electricity. *Science*, 335 (2012) 53-59
- [9] P. Balachandra, B.S. Reddy, Hydrogen energy for the transport sector: a well-to-wheel techno-economic and environmental feasibility analysis. IGIDR, Mumbai, p. 35 (2007).
- [10] M.P. de Wit, A.P.C. Faaij, Impact of hydrogen onboard storage technologies on the performance of hydrogen fuelled vehicles: A techno-economic well-to-wheel assessment. *Int J Hydrogen Energ*, 32 (2007) 4859-4870
- [11] GM Well-to-wheel analysis of energy use and greenhouse gas emissions of advanced fuel / vehicle systems - a European study. L-B systemtechnik, Ottobrun, Germany, (2002) 130
- [12] Well-to-Wheels Analysis of future automotive fuels and powertrains in the European context, Joint Research Centre. (2007).
- [13] A. Hu, S. Levis, G.A. Meehl, W. Han, W.M. Washington, K.W. Oleson, B.J. van Ruijven, M. He, W.G. Strand, Impact of solar panels on global climate. *Nat. Clim. Chang*. 6.3 (2016) 290-294.
- [14] B. K. Sovacool, Valuing the greenhouse gas emissions from nuclear power: a critical survey. *Energy Policy*, 36(8) (2008) 2950-2963.
- [15] D.J. Friedman, Progress and challenges for next-generation high-efficiency multijunction solar cells. *Curr Opin Solid St M*, 14(6) (2010) 131–138.
- [16] M.E. Meral, F. Diner, A review of the factors affecting operation and efficiency of photovoltaic based electricity generation systems. *Renew. Sustainable Energy Rev.*, 15(5) (2013) 2176–2184.
- [17] F. Fouladi, P. Henshaw, D. S-K. Ting. Enhancing smart grid realisation with accurate prediction of photovoltaic performance based on weather forecast. *Int J Environ Stud* 70.5 (2013) 754-764.

- [18] A. M. Jacobi, R. K. Shah. Heat transfer surface enhancement through the use of longitudinal vortices: a review of recent progress. *Exp. Therm. Fluid Sci* 11.3 (1995) 295-309.
- [19] M. Sheikholeslami, M. Gorji-Bandpy, D. D. Ganji, Review of heat transfer enhancement methods: focus on passive methods using swirl flow devices. *Renew. Sustainable Energy Rev.*, 49 (2015) 444-469.
- [20] S. Chamoli, N. S. Thakur, J. S. Saini, A review of turbulence promoters used in solar thermal systems. *Renew. Sustainable Energy Rev.*, 16(5) (2012) 3154-3175.
- [21] C.A. Sylmar, Photovoltaic systems concept study: final report (ALO-2748-12) Springfield, VA: US Department of Energy, Division of Solar Energy, Spectrolab, Inc., 1977
- [22] D.L. Evans, Simplified method for predicting photovoltaic array output. *Sol Energy*, 27(6) 1981 555–560.
- [23] J.A. Duffie, W.A. Beckman, *Solar engineering of thermal processes*, 2nd ed. John Wiley and Sons, New York, 1980.
- [24] International Electrotechnical Commission, 1993, Crystalline silicon terrestrial photovoltaic modules – design qualification and type approval, 2nd ed. (Geneva: IEC) (International Standard EN-61215, 1993–04).
- [25] S. Sharples and P.S. Charlesworth, Full scale measurement of wind induced convective heat transfer from a roof mounted flat plate solar collector. *Solar Energy*, 62(2) (1998) 69–77.
- [26] National Solar Radiation Database, <https://nsrdb.nrel.gov/> (accessed on 20 April, 2017)
- [27] R. E. H. Sims, Renewable energy: a response to climate change. *Sol energy*, 76(1) (2004) 9-17.
- [28] P. B. Breslow, D. J. Sailor, Vulnerability of wind power resources to climate change in the continental United States, *Renew. Energy*, 27(4) (2002) 585-598.
- [29] S. Jerez, I. Tobin, R. Vautard, J. P. Montávez, J. M. López-Romero, F. Thais, G. Nikulin, The impact of climate change on photovoltaic power generation in Europe, *Nat. Commun.*, (2015) 6.

[30]S. C. Pryor, R. J. Barthelmie, Climate change impacts on wind energy: a review, *Renew. Sustainable Energy Rev.*, 14(1) (2010) 430-437.

CHAPTER 3

AN EXPERIMENTAL STUDY OF TURBULENT FLOW BEHIND A DELTA WINGLET

Hao Wu¹, David S-K. Ting^{1†} & Steve Ray²

¹*Turbulence and Energy Laboratory, Centre for Engineering Innovation, University of Windsor,*

401 Sunset Ave, Windsor, Ontario, N9B 3P4, Canada

[†]*Corresponding Author, dting@uwindsor.ca*

²*Essex Energy Corporation, 2199 Blackacre Dr, Suite #2, Oldcastle, Ontario, NOR 1L0, Canada*

H. Wu, D. S-K. Ting, S. Ray., An experimental study of turbulent flow behind a delta winglet, *Exp. Therm. Fluid Sci.*, 88 (2017) pp. 46-54

3.1 Introduction

Convective heat transfer by air commonly exists in many engineering applications such as heat exchangers and the cooling of solar photovoltaic panels. In most cases, it is desirable to enhance the heat transfer, either passively or actively [1]. The passive enhancement of convective heat transfer that does not require any external power can be accomplished by extending the heat transfer surface, perturbing the flow, or adding additives to the fluid flowing across the surface. Active techniques such as vibration, electro field, and acoustic excitation require external power to accomplish enhancement [2]. Due to cost/benefit considerations, passive techniques such as fins (extended surface) and turbulators (perturbed flow) are more widely used. However, the heat transfer enhancement by these techniques typically comes with significant pressure drop, leading to some heat transfer loss associated with flow speed reduction. A specific type of

turbulator called the longitudinal vortex generator has been gaining attention since the 1990s. It can generate vortices with an axis parallel to the main flow direction. These vortices are produced via flow separation and viscous friction. This type of strong swirling secondary flow can reduce the boundary layer thickness, increase the temperature gradient near the surface, and directly increase convective heat transfer via cross-stream velocity. This longitudinal vortex generator has the added feature of an extended heat transfer surface. Furthermore, the pressure drop associated with longitudinal vortices is significantly less than that caused by streamwise vortices [2] and hence, less reduction in streamwise velocity results.

The heat transfer enhancement by longitudinal vortex generators has been extensively studied [3-15]. The rectangular and delta wings and winglets are typical objects of studies, as sketched in Figure 3.1. These wing-type vortex generators can be either attached on the wall or punched out of the surface. Previous studies [3-15] have found that these longitudinal vortex generators could achieve a significant enhancement of heat transfer with a moderate pressure drop. The influence of longitudinal vortices on energy and momentum transport is long lasting; as far as 60 wing chords downstream behind Eibeck and Eaton's delta winglet [5]. Fiebig compared wings and winglets of different shapes, and found that the rectangular and triangular shapes give similar pressure penalty and heat transfer enhancement, while winglets have better performance than wings [14]. Torii and Yanagihara [15] conducted systematical study on the heat transfer enhancement by a single vortex generated by a winglet. They investigated the influence of the angle of attack, free stream velocity and the winglet height. However, their study is not accompanied with the flow structure measurement.

To better understand the underlying physics of the longitudinal vortex and its interaction with the boundary layer, detailed turbulent flow parameters must be systematically scrutinized. Godard and Stanislas [16] investigated the vortices generated by a pair of counter-rotating winglets using particle image velocimetry (PIV). The winglets were

mounted on a bump, which was used to generate an adverse pressure gradient. The winglets height was less than half of the boundary layer thickness. They studied at three locations, from 22 to 57 winglet heights downstream of the winglets. The vortices decreased in intensity and increased in size with distance, and when reaching 57 winglet heights downstream, the vortices were hardly detectable, although the downwash was still visible. Velte et al. [17] furthered this study by performing stereoscopic PIV measurement at four locations close to the winglets, from 1 to 8 winglet heights downstream of the winglets on a bump. In this study the winglets height was the same as the boundary layer thickness. Henze et al. [18] studied the vortices generated by a full-body tetrahedral element, mounted on the bottom wall of a wind tunnel test section. They used a three-component PIV system to capture flow velocities in all directions. The PIV measurements were conducted in cross-stream plane and streamwise plane.

The PIV technique is suitable for obtaining the velocity profile and velocity vector of vortices. On the other hand, the hot wire, with its ability to measure at much higher frequencies, can give a deeper view of the underlying turbulent parameters. Cutler and Bradshaw [19, 20] conducted detailed measurements of the common wake of delta wings using hot-wire and pressure probes. In their studies, the vortices were generated at two different heights, one over the boundary layer and the other merged into the boundary layer. For the first case, the boundary layer beneath the vortices is thinned by lateral divergence, and at the outboard of the vortices, it is thickened by lateral convergence. As the vortices merge into the boundary, the boundary layer between the vortices is kept thin by lateral divergence.

Shabaka et al. [21] studied a single vortex generated by a half-delta wing penetrating into the turbulent boundary layer using hot wire anemometers. The circulation around the vortex penetrating into the boundary layer was almost conserved, that is, it decayed very slowly. Mehta and Bradshaw [22] furthered this study by using two half-delta wings to generate vortices that rotate in opposite directions and the common flow between them was away from the surface. The mean velocity and turbulence downstream were

quantified. The cancellation of circulation by fluid mixing from the two vortices was found to be slow.

Lau [23] investigated the channel flow with pairs of rectangular winglets arranged periodically in both spanwise and streamwise directions. The three components of the flow velocity were measured using an X-wire and a quadruple hot-wire probe. The mean velocity vector, long-time averaged Reynolds stresses and the turbulent kinetic energy are presented. Biswas et al. [13] investigated the flow structure of a vortex generated by a delta winglet in a channel flow by a rotation probe, and compared their measurements with simulation results. They found that the vortices undergo elliptical deformation due to the channel walls. Also observed was a corner vortex with two induced vortices.

Since a winglet can enhance heat transfer with little pressure penalty, and the generated vortices are more maneuverable than those from wings, the study on the flow structure of the wake of winglets is imperative. Most of the above-mentioned studies on winglets were conducted in a confined channel where the influence of the walls is significant. A more elementary condition, an unconfined flow, may give a clearer and more fundamental view of the vortex flow generated without the interference of confining walls. Though the turbulent flow behind wings on a flat plate has been relatively well studied, the research on winglets is scarce. The objective of this study is to investigate the turbulent structures and parameters of the vortex generated by a winglet on a flat plate in the unconfined condition using a triple sensor hot-wire anemometer. The detailed flow characteristics are related to heat transfer based on existing knowledge in the literature and physical reasoning.

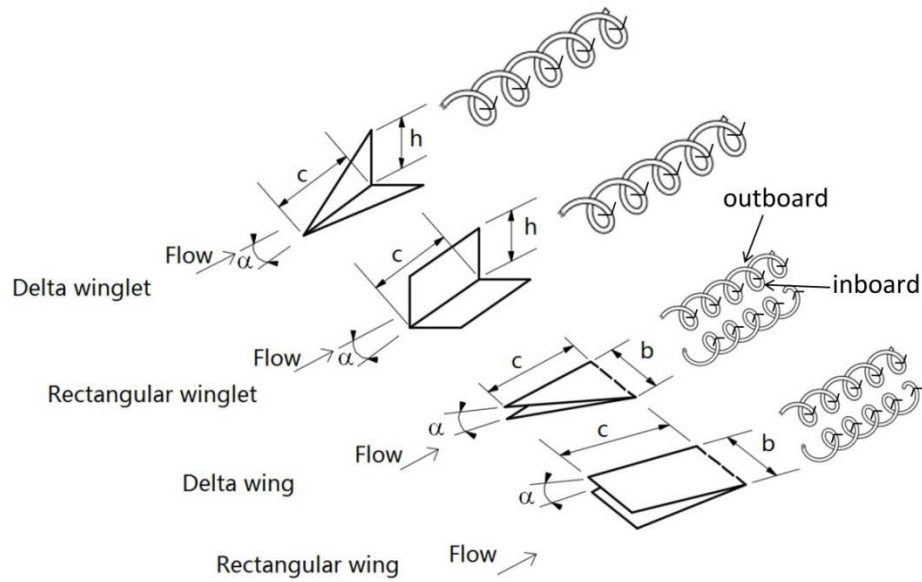


Figure 3. 1 Typical vortex generators. α is the angle of attack, c is the chord length, h is the winglet height, and b is the span or width.

3.2 Experimentation

Figure 3.2 shows the experimental setup. The studied delta winglet was made from a 0.1 mm thick aluminum sheet. The height of the delta winglet, h , was 10 mm and the length, c , was 20 mm, giving an aspect ratio of $4h/c = 2$. The size of the winglet was chosen to be of the same magnitude as the boundary layer thickness to ensure the generated vortex interacted well with the boundary layer. The experiment was conducted in a wind tunnel with a 76 cm high and 76 cm wide cross section. The delta winglet was attached to a flat plate via one of its folds with an angle of attack, α , of 30 degrees. The winglet was placed one chord length away from the leading edge to avoid the possible influence by the flow separation from the plate's leading edge. The flat aluminum plate was 33.5 cm wide, 52.5 cm long and 2.35 mm thick, with a chamfered leading edge of 35 degrees. The velocity profile of the base flat plate case in the absence of the winglet confirmed minimal leading edge disturbance. This flat plate was placed at mid-height in the middle of the test section. The streamwise area of the flat plate and the stand were no more than 3% of the wind tunnel cross-sectional area. The background turbulence intensity was around 0.4%. The free stream velocity was kept at 7.7 m/s, with Reynolds number of 5000 based on the

winglet height. A triple sensor hotwire probe (type 55P91) with a constant-temperature anemometer was applied to measure the velocity at 100 mm (10h) downstream of the winglet. The measured plane was 40 mm × 26 mm, with a spatial resolution of 2 mm. The signals were obtained at a sampling frequency of 80 kHz and a sampling number of 10^6 . The signal was low passed at 30 kHz. All three velocity components, u, v, w, were measured simultaneously.

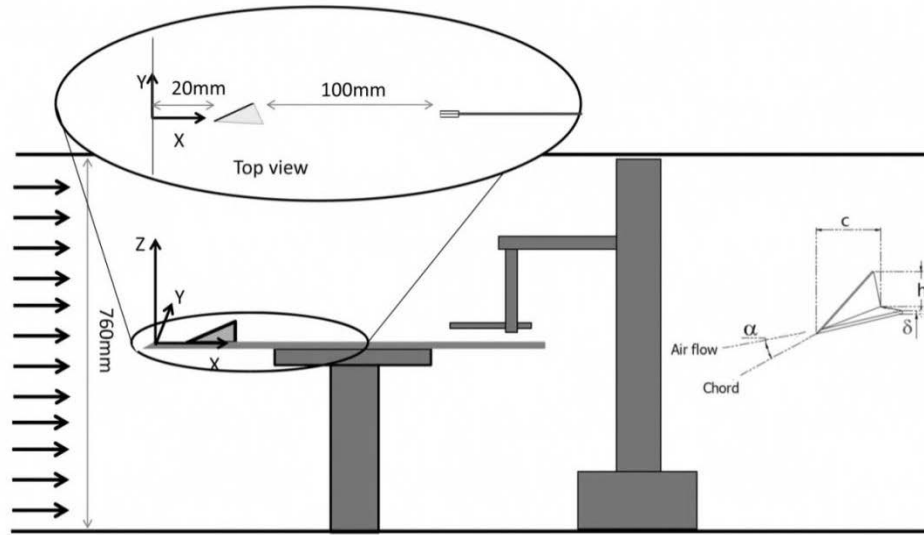


Figure 3. 2 The experimental setup inside a wind tunnel. The $\delta = 1$ mm winglet is fixed at $1c$ from leading edge, $\alpha = 30^\circ$, $h = 10$ mm, $c = 20$ mm, hot wire at $10h$ downstream of the winglet.

3.3 Data Processing and Uncertainty analysis

From the hot-wire anemometer the instantaneous voltage values at each location of interest were recorded. Based on the calibration coefficient and the temperature, the instantaneous velocities (U, V, and W) were deduced. Subsequently, the time-averaged velocity (\bar{U}) was calculated from:

$$\bar{U} = \frac{1}{N} \sum_{i=1}^N U_i \quad (3.1)$$

where the sample size N is 10^6 . The instantaneous fluctuating velocity (u) was obtained from:

$$u_i = U_i - \bar{U} \quad (3.2)$$

The root mean square velocity (u_{rms}), usually used to express the intensity of the turbulence, was calculated from:

$$u_{\text{rms}} = \sqrt{\frac{\sum_{i=1}^N u_i^2}{N-1}} \quad (3.3)$$

Both time-averaged velocity and root mean square velocity (turbulence intensity) were normalized using the free stream velocity to get the corresponding dimensionless quantities.

The cross-stream velocity vector was generated from the velocity components in the Y and Z directions, \bar{V} and \bar{W} . The corresponding magnitude was deduced from:

$$L = \sqrt{(\bar{V}^2 + \bar{W}^2)} \quad (3.4)$$

and the angle was determined from:

$$\theta = \arctan\left(\frac{\bar{W}}{\bar{V}}\right) \quad (3.5)$$

Non-dimensional vorticity was defined as:

$$\Omega = \frac{\omega \times h}{U_\infty} \quad (3.6)$$

where h is the height of the delta winglet, and vorticity,

$$\omega = \frac{\partial w}{\partial y} - \frac{\partial v}{\partial z} \quad (3.7)$$

Taylor scale represents the small eddies in the turbulent flow and is considered as the dissipative length. Taylor time scale (τ_λ) can be expressed as:

$$\tau_\lambda = \sqrt{\frac{2u^2}{\left(\frac{du}{dt}\right)^2}} \quad (3.8)$$

In the case of discrete data, it is:

$$\tau_\lambda = \frac{\sqrt{\frac{1}{N} \sum_{i=1}^N 2u_i^2}}{\sqrt{\frac{1}{N-1} \sum_{i=1}^{N-1} \left(\frac{u_{i+1}-u_i}{\Delta t}\right)^2}} \quad (3.9)$$

Based on the Taylor frozen hypothesis [24], which states that the eddies can be considered merely passing the probe without evolution if the velocity fluctuation is small compared to the convective current that carries the eddies, the Taylor microscale (λ) can be obtained from:

$$\lambda = \bar{U} \cdot \tau_\lambda \quad (3.10)$$

Integral length scale represents the large, energy containing eddies. Its time scale can be estimated using the autocorrelation factor (ρ):

$$\rho(\tau) = \frac{\overline{u(t)u(t+\tau)}}{u^2(t)} \quad (3.11)$$

For discrete samples, it is:

$$\rho(m\Delta t) = \frac{\frac{1}{N-m} \sum_{i=1}^{N-m} (u_i u_{i+m})}{\frac{1}{N} \sum_{i=1}^N u_i^2} \quad (3.12)$$

where m is varied from 0 to $N - 1$. The integral time scale is defined as:

$$\tau_\Lambda = \int_0^\infty \rho(\tau) d\tau \quad (3.13)$$

For discrete samples, it is:

$$\tau_\Lambda = \sum_{i=1}^{N_k-1} \rho(i\Delta t) \Delta t \quad (3.14)$$

where N_k is the point where the autocorrelation factor first crosses over the zero value. Similar to the Taylor length scale, the integral length scale can be obtained from:

$$\Lambda = \bar{U} \cdot \tau_\Lambda \quad (3.15)$$

The total uncertainty associated with each parameter consists of bias and precision uncertainties. Bias uncertainty (B) was estimated according to Jorgensen [25], including

the uncertainty from calibration, data acquisition, data reduction, etc. Precision uncertainty (P) represents the repeatability of the measurement, and it can be deduced from the Student's t distribution method with a 95% confidence interval [26]. The total uncertainty is:

$$E = \sqrt{B^2 + P^2} \quad (3.16)$$

The total uncertainties of \bar{U} and u_{rms} were deduced directly from the above method. For the other parameters, the uncertainty was derived according to error propagation [26], and the following equations were used:

$$\frac{E_{\frac{\bar{U}}{U_\infty}}}{\frac{\bar{U}}{U_\infty}} = \sqrt{2 \left(\frac{E_{\bar{U}}}{\bar{U}} \right)^2} \quad (3.17)$$

$$\frac{E_{\frac{u_{rms}}{U_\infty}}}{\frac{u_{rms}}{U_\infty}} = \sqrt{\left(\frac{E_{\bar{U}}}{\bar{U}} \right)^2 + \left(\frac{E_{u_{rms}}}{u_{rms}} \right)^2} \quad (3.18)$$

$$\frac{E_{\frac{\lambda}{\lambda}}}{\frac{\lambda}{\lambda}} = \sqrt{\left(\frac{E_{\bar{U}}}{\bar{U}} \right)^2 + 2 \left(\frac{E_{u_{rms}}}{u_{rms}} \right)^2} \quad (3.19)$$

$$\frac{E_{\frac{\Lambda}{\Lambda}}}{\frac{\Lambda}{\Lambda}} = \sqrt{\left(\frac{E_{\bar{U}}}{\bar{U}} \right)^2 + 2 \left(\frac{2E_{u_{rms}}}{u_{rms}} \right)^2} \quad (3.20)$$

3.4 Results and Discussion

3.4.1 Velocity Profile

In Figure 3.3, the cross-stream velocity vector at 100 mm (10h) downstream of the delta winglet at $U_\infty = 7.7$ m/s is presented to show the magnitude and direction of the secondary flow. The leading vortex of the delta winglet was located at $Y/h = 0$, as presented by the dashed line in the figure. It is clear that there is a large vortex structure in the wake. Biswas et al. [13] coined this vortex as the main vortex, and explained that its formation was due to the flow separation at the leading edge of the winglet. The region where the flow moves toward the plate has been called the inflow or downwash

region, and the area where the flow moves upward, away from the plate is called the outflow or upwash region.

The possible influences of this vortex on the heat transportation from the plate surface include two parts. First, it can scoop up the heated air from the hot surface; this is particularly the case in the outflow region. In the inflow region, cold air is brought toward the plate into the boundary layer, after receiving thermal energy in boundary layer, it is convected away via the outflow. The other effect of this vortex is the perturbation of the boundary layer by lateral divergence in the inflow region. This, along with the turbulence generated in the wake, is expected to promote effective heat removal. Cutler and Bradshaw [19] regarded the boundary layer as two-dimensional, and they quantified the effect of lateral divergence and convergence in terms of the extra-rate-of-strain parameter $(\frac{\partial V}{\partial y} / \frac{\partial U}{\partial z})$ at $z/\delta_{0.995}=0.5$. Smits et al. [27] found that this strain parameter has a significant effect on the turbulent boundary layer structure when it is in the order of 0.1. In the present study, the extra-rate-of-strain parameter is much greater than 0.1, implying that the flow cannot be regarded as a perturbation on a two-dimensional boundary layer. The large flow angle variations (as large as 19 degrees, shown in Figure 3.4) and large lateral gradients in the mean velocity suggest that the boundary layer is highly three-dimensional. In the current study, the main vortex is marked as Region M, and the induced vortex, which will be discussed later, is marked as Region I. The area at the bottom right corner, where the cross-stream flow is almost stagnant, is marked as Region S.

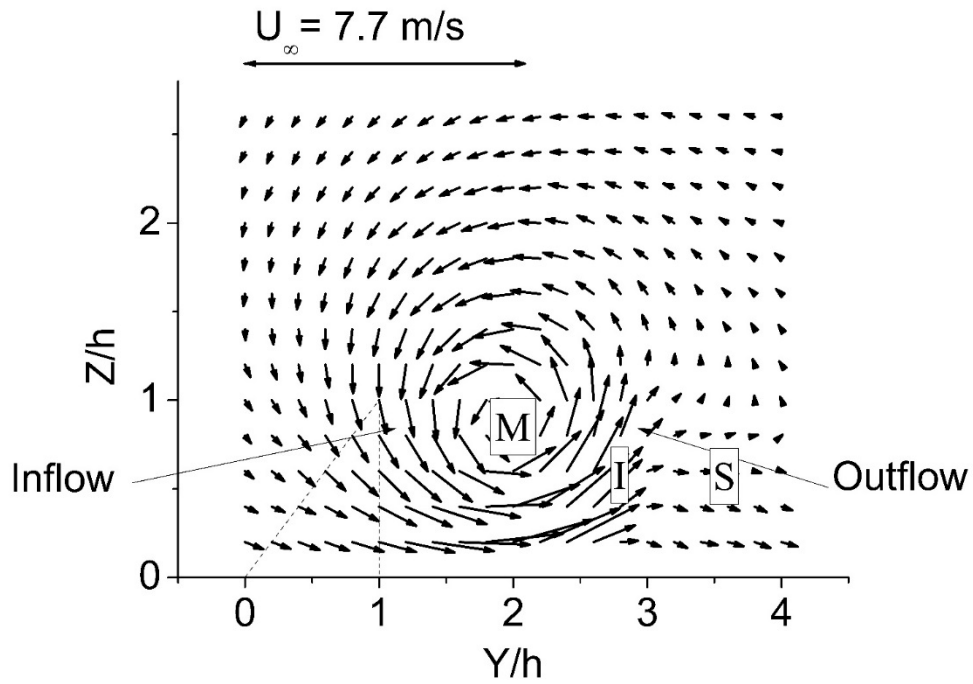


Figure 3. 3 Cross-stream velocity vector at 10 winglet heights downstream of the delta winglet.

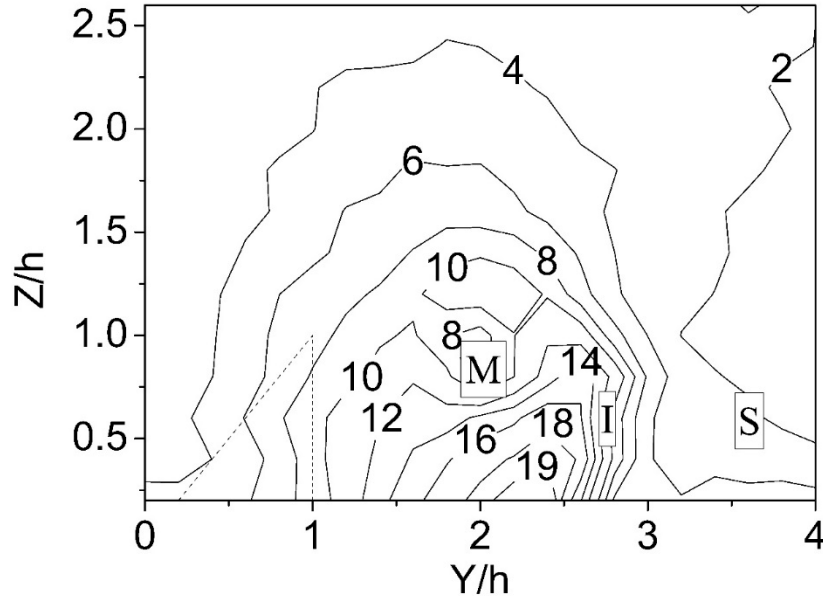


Figure 3. 4 Mean flow angle (degrees) at 10 winglet heights downstream of the delta winglet.

To better identify the vortex, the non-dimensional vorticity is presented in Figure 3.5. Note that these are time-averaged values, that is, they are not the instantaneous results. The center of the vortex is at approximately $Y/h = 2$ and $Z/h = 0.8$, where the largest vorticity is found. Cutler and Bradshaw [20] defined the core of vortex as the position where it has minimum total pressure. In their study, the core was found to move outward (to outflow side) and downward as the flow moves downstream in the beginning, then it moves outward and then gradually upward. The change of the horizontal location is caused by the outward movement of the near-surface vorticity. The lifting of vorticity away from the wall is called vortex rebound, which has also been observed in other studies [28, 29]. For the investigations in confined tunnel flow [13, 23], the vortex generated by delta winglet and rectangular winglet was found at the center right behind the vortex generators due to the restriction of vortex location by the tunnel walls. At the upwash region near the plate in Figure 3.5, another vortex with a rotation opposite to the main vortex can be observed, though the vorticity curve is not complete at the bottom due to the limitation of measurement facility. Biswas et al. [13] named this vortex the “induced vortex.”

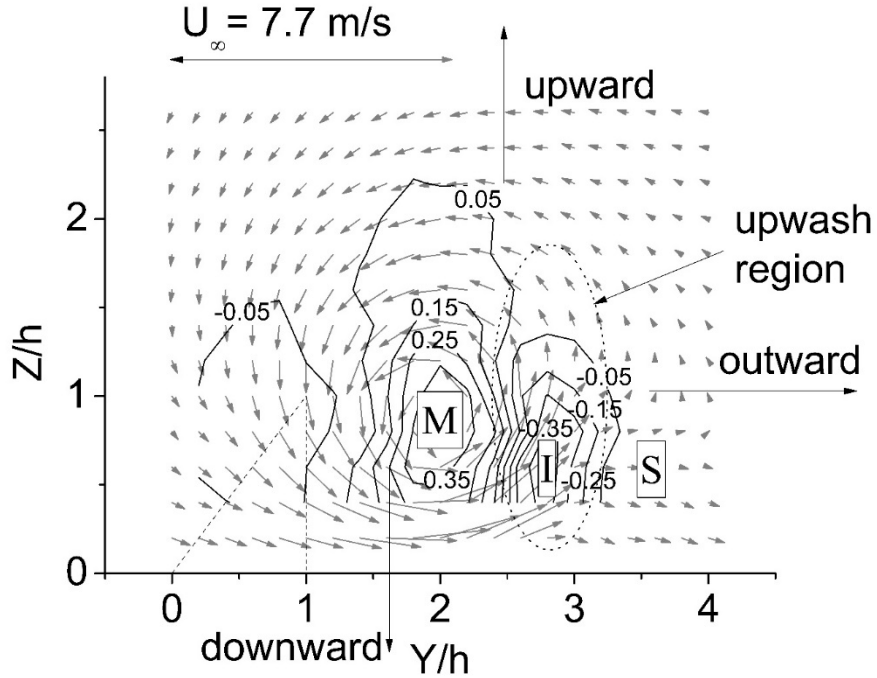


Figure 3.5 Nondimensional vorticity Ω at 10 winglet heights downstream of the delta winglet.

In order to see the influence of the interaction between the vortex and boundary layer on streamwise velocity, the time averaged streamwise velocity at 100 mm (10 winglet heights) downstream of the delta winglet is scrutinized. Figure 3.6 shows the sum of W velocities normalized by free stream velocity (\bar{W}/U_∞). We can see at $Y/h = 1.4$ and 2.4 it has maximum and minimum values, respectively; and thus, these two locations are chosen to represent the typical inflow and outflow regions. Figure 3.7 shows the normalized streamwise velocities (\bar{U}/U_∞) at $Y/h = 1.4$ and 2.4 and are contrasted with the base flat plate case (without winglet). The boundary layer thickness is defined as the height where U has 99% of free stream velocity. For the base flat plate case (without the winglet), this is approximately 6 mm (0.6 h) at 10 winglet heights downstream of the winglet. This thickness is more than twice of the laminar boundary layer thickness, 2.6 mm, calculated from $\frac{\delta}{x} = \frac{5}{\text{Re}_x^{1/2}}$ [30]. The turbulent boundary layer thickness derived from $\frac{\delta}{x} = \frac{0.37}{\text{Re}_x^{1/5}}$ is 5.5 mm, roughly the current measured boundary layer thickness.

Furthermore, the velocity profile of the present flat plate case, in the absence of the

winglet, follows the turbulent boundary layer curve $\frac{\bar{U}}{U_\infty} = \left(\frac{z}{\delta}\right)^{\frac{1}{7}}$. Compared to this reference condition, the inflow region has a thicker boundary layer. Near the plate (at $Z/h = 0.2$) the normalized velocity for inflow is approximately 0.92, significantly larger than that for the base flat plate condition of 0.8. Torii and Yanagihara [15] heat transfer measurements confirmed that Stanton number peaked in the inflow region. The outflow region has a similar boundary layer thickness as the inflow region, but its velocity is lower than that of base flat plate case. Near the plate surface, the normalized velocity for the outflow region is approximately 0.73, and thus, the heat transfer rate is expected to be less. This anticipated decrease in heat transfer rate in the outflow region has been reported by Eibeck and Eaton [5]. The maximum uncertainty in the normalized time-averaged velocity is estimated to be 0.02.

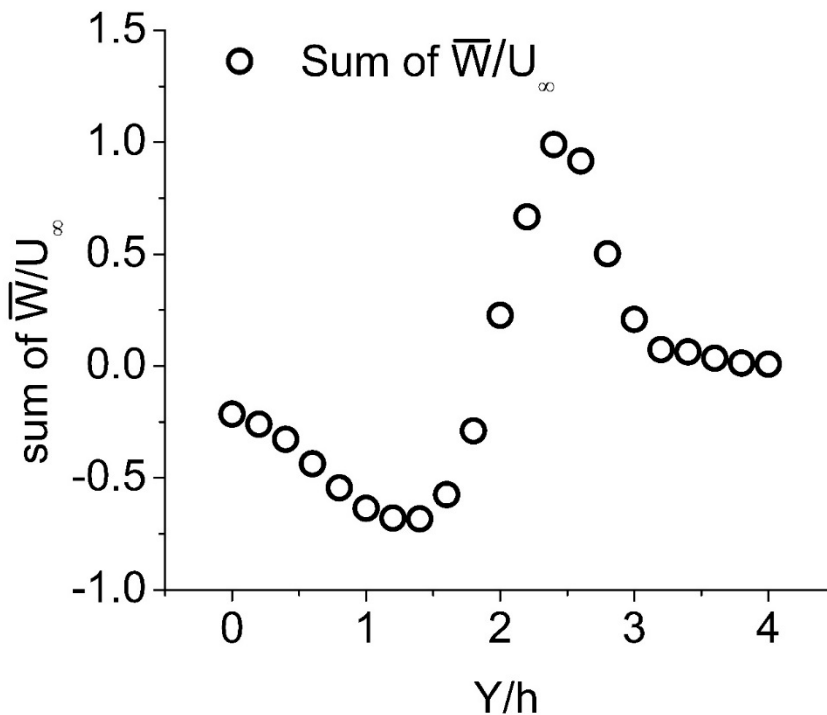


Figure 3. 6 The sum of normalized W velocity for each y position at 10 winglet heights downstream of the delta winglet.

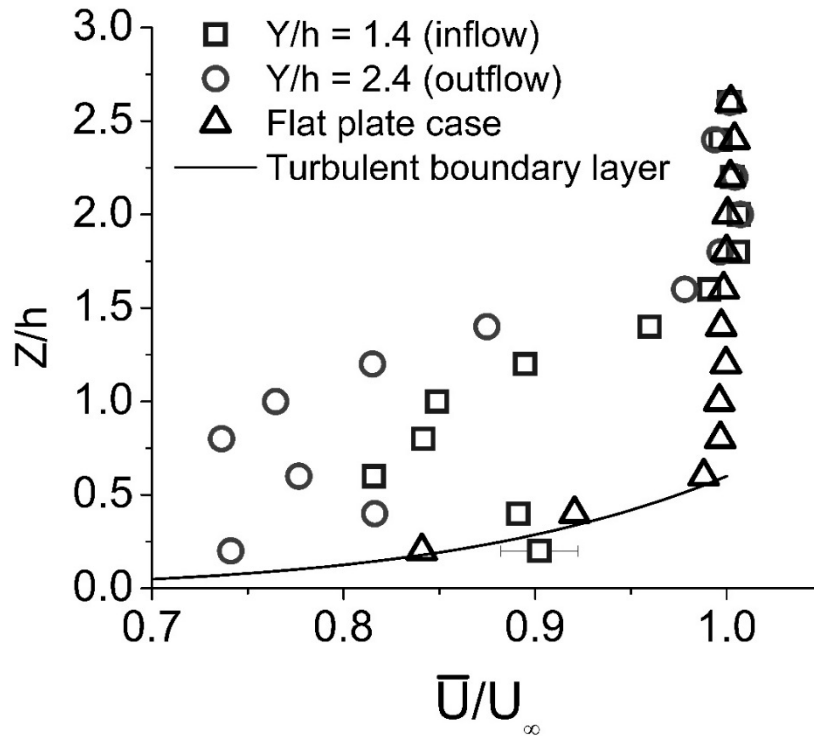


Figure 3.7 Streamwise velocity \bar{U}/U_∞ of inflow, outflow, and the base flat plate case without the winglet, at 10 winglet heights downstream of the delta winglet.

Figure 3.8 shows the profile of the normalized streamwise velocity on the measured plane. As discussed earlier, in the presence of the vortex, the boundary layer thickness becomes thicker than that of the underlying flat plate case. We can see the vortex is embedded into the boundary layer. The distribution of streamwise velocity deficit coincides with the vortex structure in Figure 3.3, and only 65% of the free stream velocity is detected at the vortex core. This maximum streamwise velocity deficit at the core of the vortex has also been observed in confined flow for winglet [13], but not on vortices generated by wings [19, 20]. In the wing studies, the mean velocity has some deficit near the core of the vortex, but at the center, the velocity recovers to 100% of the free stream value. This difference may imply that the vortex generated by wings and winglets have different streamwise velocity properties. Further studies are needed to confirm this. The deficit of mean U velocity may decrease the heat transfer rate to some extent, but the effect has to be considered in conjunction with the accompanying turbulence intensity increase. At the

upwash region, there is another velocity deficit caused by the induced vortex. The heat transfer rate could be decreased at this region due to this velocity deficit, noting that when the cross-flow reaches the outflow region it has already been heated.

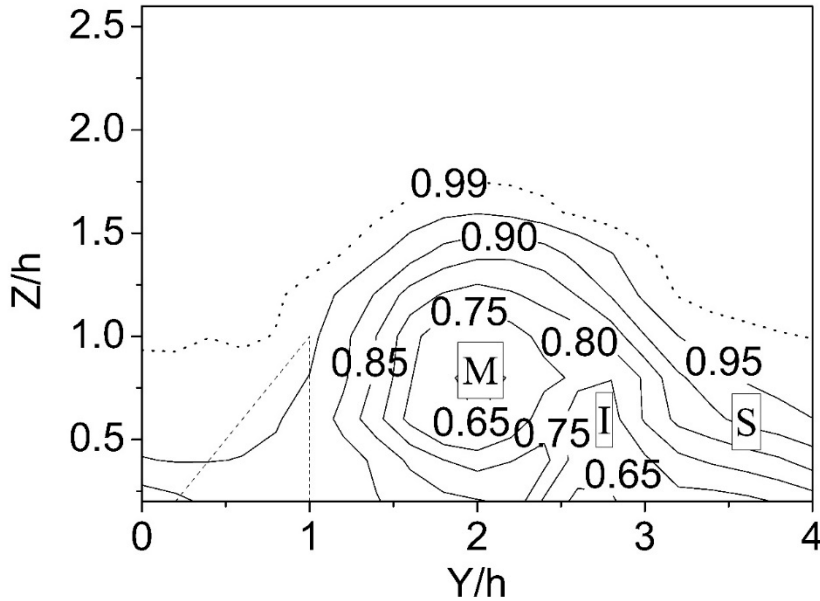
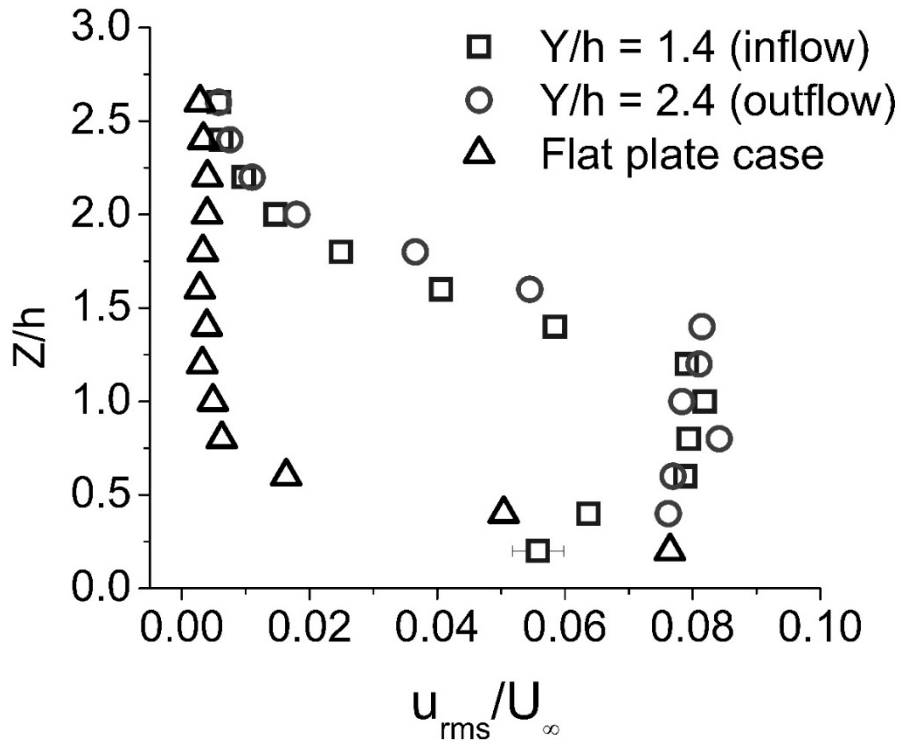


Figure 3. 8 Streamwise velocity \bar{U}/U_∞ profile at 10 winglet heights downstream of the delta winglet.

3.4.2 Turbulence Intensity

Besides the big vortex structure, the turbulence in the wake is another important parameter dictating the convection heat transfer rate. In Torii and Yanagihara [15], the heat transfer enhancement caused by a longitudinal vortex embedded in the laminar boundary layer is mostly attributed to the transition to a turbulent boundary layer, instead of the vertical motion itself. In Figure 3.9, turbulence intensity, Tu (u_{rms}/U_∞), of the inflow, the outflow, and the base flat plate cases are compared, along with the comparison of Tu , Tv (v_{rms}/U_∞) and Tw (w_{rms}/U_∞). As can be seen, for the reference flat plate case, the turbulence intensity has its highest value of 8% adjacent to the plate surface, and it decreases to the free stream turbulence value (0.4%) with increasing

normal distance from the plate. Note that the turbulence intensities for all three components are similar. The largest difference among T_u , T_v , and T_w is 3%, at the same location. Patten et al. [31] have found that in wall-bounded turbulent flows, the rms of the velocity fluctuations peaks close to the wall. This peak value has been reported to be at a Z/δ^* value of approximately 1.3 (which would be $Z/h = 0.3$ in the present study), where δ^* is the boundary layer displacement thickness. In our study, the parabolic shaped curve of T_u as a function of Z is not clearly observed. This is partly due to the restriction of the nearest location of hot wire probe to the plate, and the interval of Z value. For the inflow and outflow regions, the highest values of T_u are similar to that of a flat plate, and with distance away from the plate, the high T_u can last until $Z/h = 1.5$. Note that the large area of high T_u could significantly contribute to the local heat transfer rate. The maximum uncertainty in turbulence intensity is estimated to be 0.4%.



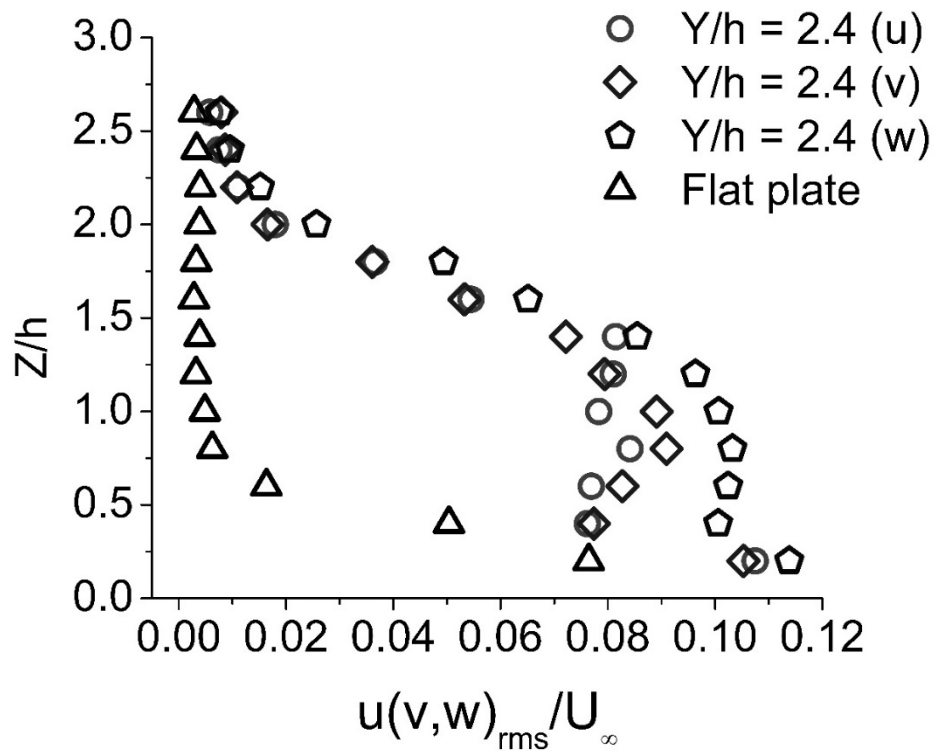
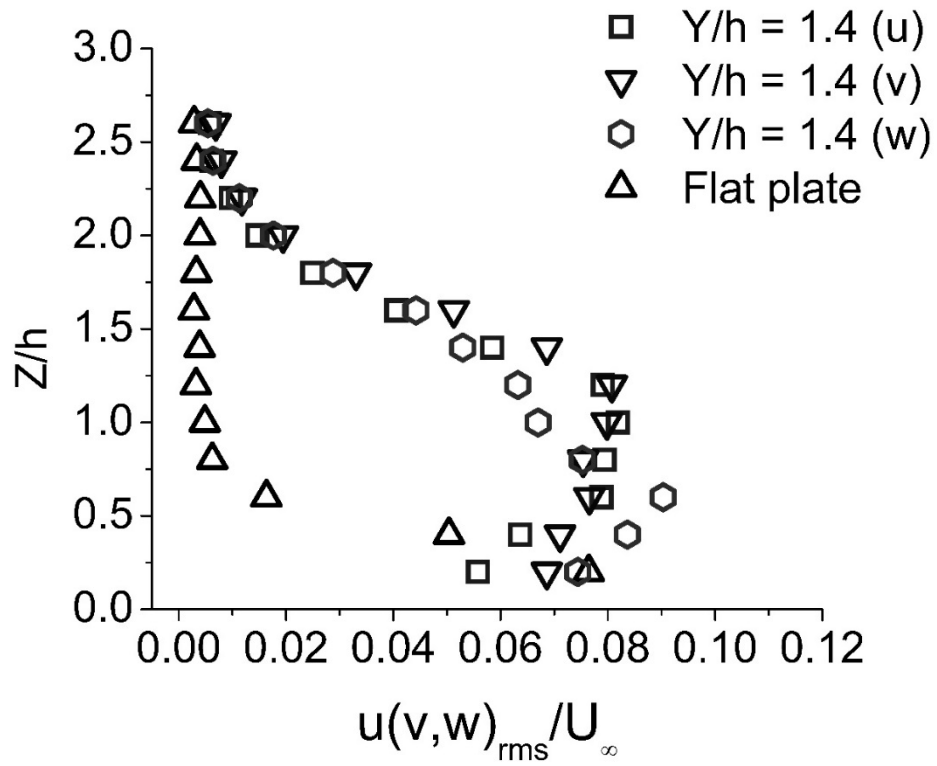


Figure 3. 9 Turbulence intensity $u(v,w)_{rms}/U_{\infty}$ of inflow, outflow, and the base flat plate case without the winglet, at 10 winglet heights downstream of the delta winglet.

The profile of turbulence intensity Tu is presented in Figure 3.10. One peak value is at the core of the longitudinal vortex (Region M). Cutler and Bradshaw [20] surmised that the large velocity fluctuation at the core of a vortex was attributed to two reasons. First, the occasional propagation of genuine turbulence into the vortex core; and second, the perturbations in velocity travel down to the core (as if in a waveguide) due to the lack of mixing in the core. From an energy point of view, this peak value in the core can be ascribed to the large vorticity and shear in the core, which can convert the energy in the main velocity into turbulence. The other peak value is at the upwash region near the plate (Region I). This turbulence intensity peak can be attributed to the scooping effect of upwash and the merge of high vorticity flow and cross-stream stagnation flow, that is, the high shear. A similar phenomenon was observed in the study of embossed-type vortex generator by Dupont et al. [32]. Other than these two peak values, the turbulence intensity has a higher value near the plate, and it decreases to free stream turbulence with the increase of distance from the plate, similar to the base flat plate case without any winglets.

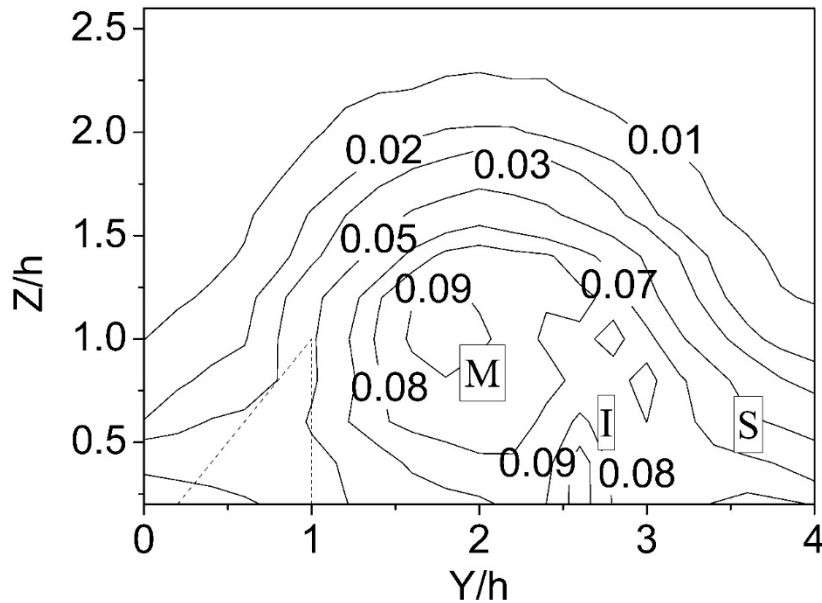


Figure 3. 10 Turbulence intensity (u_{rms}/U_{∞}) profile at 10 winglet heights downstream of the delta winglet.

3.4.3 Turbulence Length Scales.

Turbulence length scales play an important role in the convective heat transfer [33-37] and are key parameters when describing a turbulent flow [38]. However, large vortex structures may have influences on the deduction of length scales. One way to identify the difference caused by the big vortex structure is to check the statistical characteristic of the fluctuating velocity. Figure 3.11 and 3.12 show the FFT (Fast Fourier Transform) results of the instantaneous velocity signals for typical points in the main vortex at $Y/h = 2.4$ and $Z/h = 1.6$, and the induced vortex at $Y/h = 2.8$ and $Z/h = 0.6$, respectively. At both locations, the power spectral densities of u component show no recognizable peak, and therefore we may assume negligible vortex influence on the turbulent length scales deduction in the streamwise direction. For the power spectral densities of v and w components, they have the similar noticeable peak at approximately 400 Hz for the main vortex and 200 Hz for the induced vortex. One possible explanation for this phenomenon is that the probe can only detect the peak frequency of a vortex in the directions that are in the same plane as the vortex. The vortex structures observed in the current study are in

y and z planes; consequently, there is no obvious peak detected in the x direction. In short, the vortex shedding frequencies are probably 400 Hz for the main vortex and 200 Hz for the induced vortex, and the corresponding Strouhal number are 0.5 and 0.25 based on the winglet height, respectively.

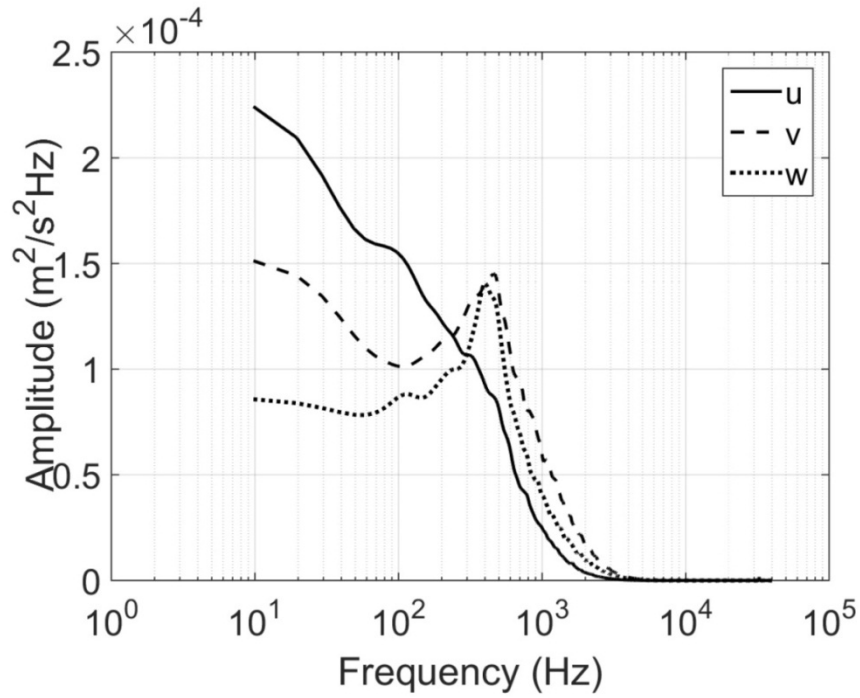


Figure 3. 11 Power spectral densities for point Y/h = 2.4 and Z/h = 1.6 at 10 winglet heights downstream of the delta winglet.

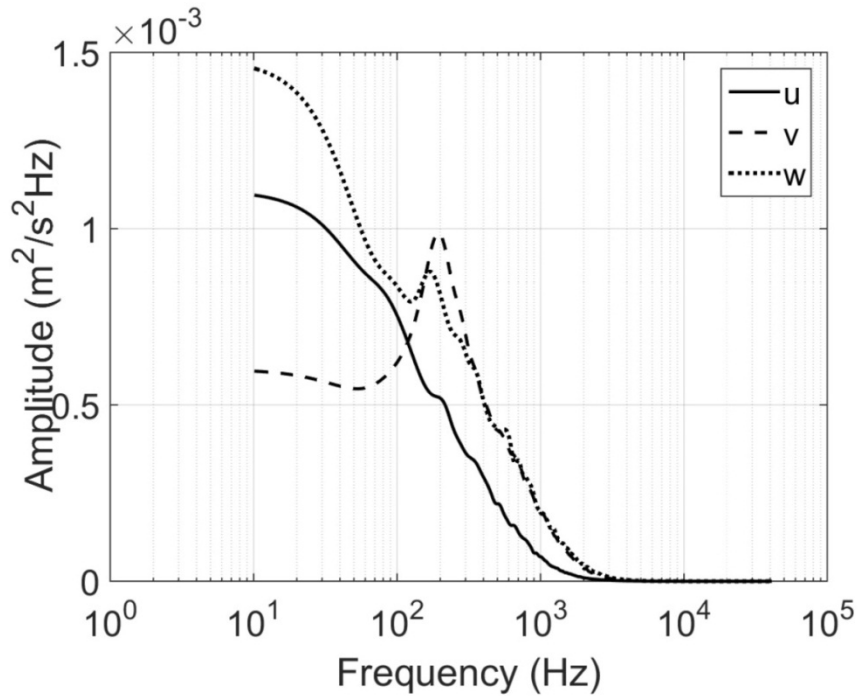


Figure 3. 12 Power spectral densities for point $Y/h = 2.8$ and $Z/h = 0.6$ at 10 winglet heights downstream of the delta winglet.

Figure 3.13 shows the contour of integral length scale (normalized by h) in the streamwise direction. Since the flow above the boundary layer is largely laminar in this study, the integral length scale has no physical meaning in that area, therefore the integral scale is only deduced when the turbulence intensity is larger than 1%. As can be seen, in Region S and upon Region M, the integral scale has its largest values. It is interesting to note that the integral scale around the main vortex has the similar value as the corresponding boundary layer thickness. It has been postulated that the turbulence length scale that is in the same order of magnitude with other characteristic sizes such as boundary layer thickness are most likely coupled [33]. In other words, eddies corresponding to the boundary layer thickness may most effectively enhance the heat transfer. The relative uncertainty in integral length scale is estimated to be 13%.

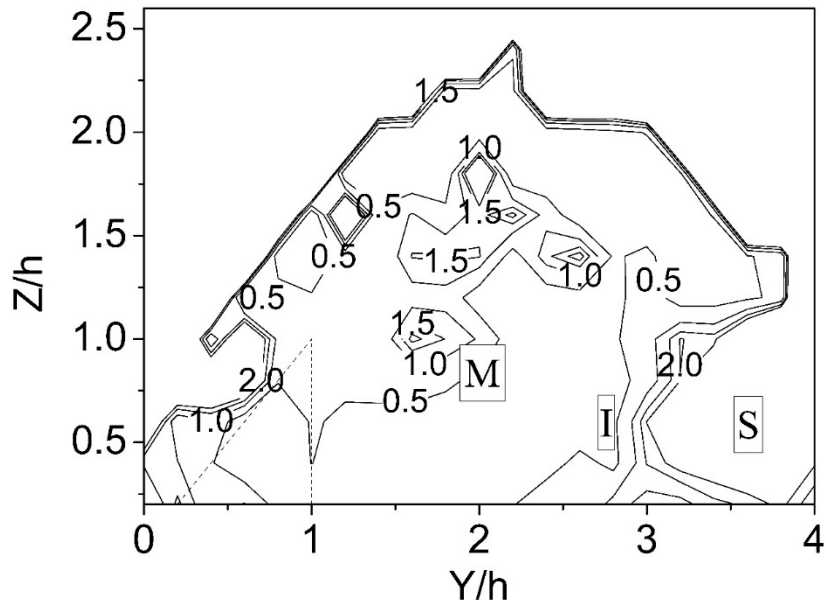


Figure 3. 13 Integral length scale (normalized by h) for u component at 10 winglet heights downstream of the delta winglet.

Figure 3.14 depicts the Taylor microscale (normalized by h) in the streamwise direction at $Y/h = 1.4$ and 2.4 contrasted with the reference flat plate case without any winglets. For the base flat plate case, Taylor microscale has its largest value adjacent to the plate and it decreases quickly with increasing z (height). In Fouladi et al. [33], the Taylor microscale was also observed to be larger near the surface. Their study also observed that at the same distance away from the flat plate, this length scale increases with the decay of turbulence. The large Taylor microscale near the surface may correspond to the shear in the boundary layer. In the current study, the inflow and outflow regions have a smaller Taylor microscale near the plate. Taylor microscale increases slightly with the increase of height, and then it decreases to the free stream value. The relative uncertainty in Taylor microscale is estimated to be 7%.

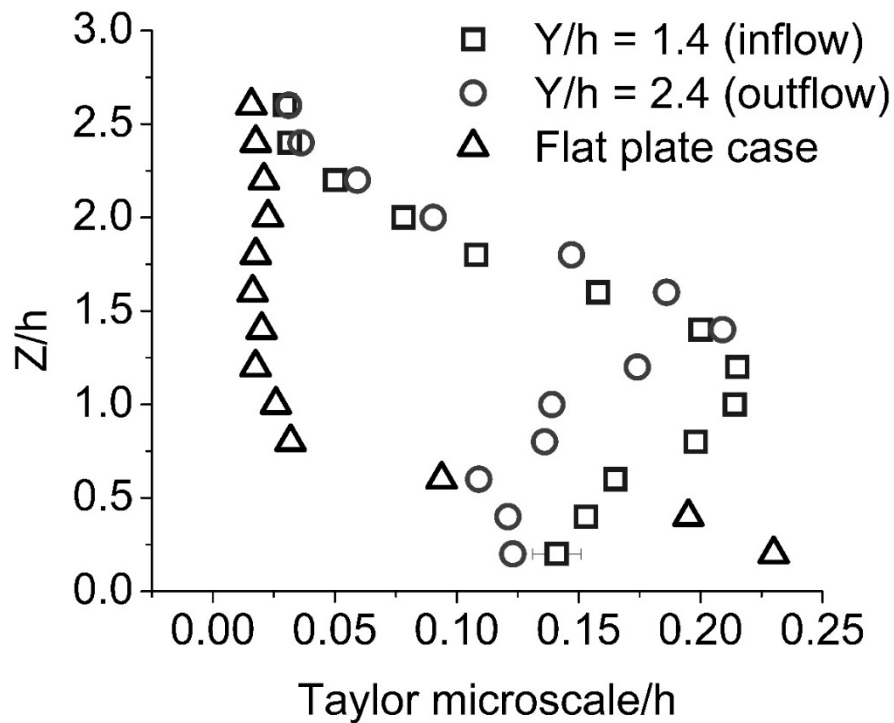


Figure 3. 14 Taylor microscale (normalized by h) for u component of inflow, outflow, and the base flat plate case without the winglet, at 10 winglet heights downstream of the delta winglet.

An overall contour view of Taylor microscale (normalized by h) is presented in Figure 3.15. At the bottom right corner, where the cross-stream flow is almost stagnant (Region S), Taylor microscale reaches its maximum size. This peak value is very similar to that of the flat plate case. In the presence of the main vortex, the Taylor microscale decreases, especially in the vicinity of the upwash region (Region I). This Taylor microscale shrinkage can be attributed to the augmentation of turbulence intensity. A stronger turbulence level can sustain a higher dissipation rate, and thus, a smaller Taylor microscale. Upon the main vortex core, another peak Taylor microscale can be seen. This peak Taylor microscale has the same value as that in Region S and hence, it appears that the main vortex has lifted part of the smallest Taylor eddies from the bottom left of Region S into the upper left of Region M. Also interesting is the concurrence occurrence of the largest Taylor microscale and integral length scale. This indicates that the size of

Taylor microscale varies in accord with the largest eddies in the energy cascade, for a given turbulence level and thus, dissipation rate.

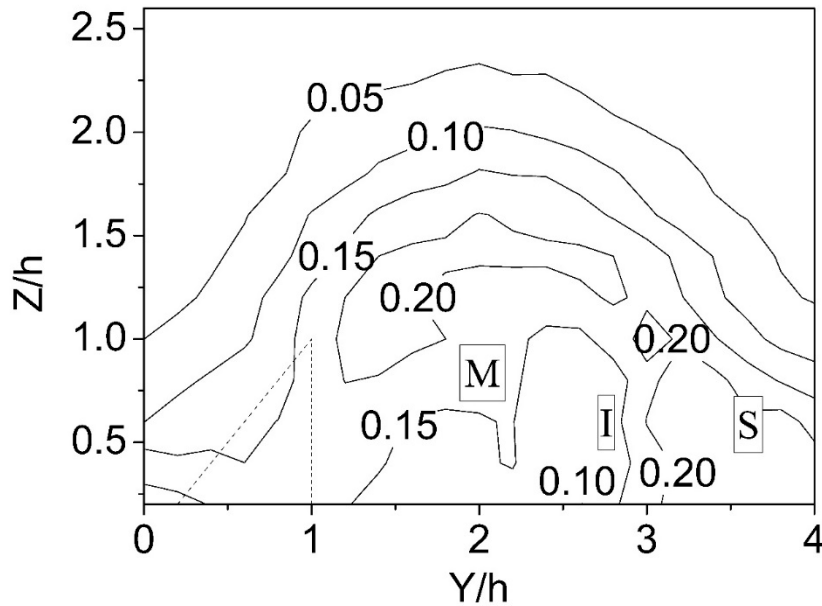


Figure 3. 15 Taylor microscale (normalized by h) for u component at 10 winglet heights downstream of the delta winglet.

3.5 Conclusion

The wake structure of a delta winglet was experimentally investigated by hot-wire measurement. The longitudinal main vortex and induced vortex were observed downstream of the winglet. The flow can be divided into two regions, inflow and outflow. The boundary layer is three-dimensional and turbulent. For both the inflow and outflow regions, the boundary layer thickness is larger than that of a flat plate, while relatively higher turbulence intensity is maintained. Compared to the reference flat plate case, the inflow region has a higher streamwise velocity near the plate surface, while the streamwise velocity in the outflow region is lower throughout. The streamwise velocity deficit and turbulence intensity have their peak values at the cores of both the main vortex and the induced vortex, presumably due to the large shear in these two locations.

The Taylor microscale has a peak at the core of the main vortex and at the cross-stream stagnant region (Region S), while a trough occurs at the core of the induced vortex. The integral length scale is of the same order of magnitude as the boundary layer thickness. The vortex shedding frequencies are detected for both vortices in y and z directions. Considering all the parameters investigated and the scooping effect of the main vortex, the inflow region is expected to have a higher heat transfer rate than the base flat plate case, and the outflow region tends to have a lower one.

Acknowledgments

This work was made possible by Natural Sciences and Engineering Research Council of Canada and Ontario Centres of Excellence.

References

- [1] R. L. Webb, N. H. Kim, Principle of enhanced heat transfer, Taylor Francis, New York, 1994.
- [2] A. M. Jacobi, R. K. Shah, Heat transfer surface enhancement through the use of longitudinal vortices: a review of recent progress, *Exp. Therm. Fluid Sci.* 11 (1995) 295-309.
- [3] A. Joardar, A. M. Jacobi, Impact of leading edge delta-wing vortex generators on the thermal performance of a flat tube, louvered-fin compact heat exchanger, *Int. J. Heat Mass Transfer* 48 (2005) 1480-1493.
- [4] M. C. Gentry, A. M. Jacobi, Heat transfer enhancement by delta-wing vortex generators on a flat plate: vortex interactions with the boundary layer, *Exp. Therm. Fluid Sci.* 14 (1997) 231-242.
- [5] P. A. Eibeck, J. K. Eaton, Heat transfer effects of a longitudinal vortex embedded in a turbulent boundary layer, *ASME J. Heat Transf.* 109 (1987) 16-24.

- [6] M. Fiebig, P. Kallweit, N. K. Mitra, Wing type vortex generators for heat transfer enhancement, Proc. 8th International Heat Transfer Conference USA 5 (1986) 2909-2913.
- [7] M. Fiebig, P. Kallweit, N. K. Mitra, S. Tiggelbeck, Heat transfer enhancement and drag by longitudinal vortex generators in channel flow, Exp. Therm. Fluid Sci. 4 (1991) 103-113.
- [8] U. Brockmeier, M. Fiebig, T. Guntermann, N. K. Mitra, Heat transfer enhancement in fin-plate heat exchangers by wing-type vortex generators, Chem. Eng. Technol. 12 (1989) 288-294.
- [9] A. Y. Turk, G. H. Junkhan, Heat transfer enhancement downstream of vortex generators on a flat plate, Proc. 8th International Heat Transfer Conference USA 6 (1986) 2903–2908.
- [10] S. R. Hiravennavar, E. G. Tulapurkara, G. Biswas, A note on the flow and heat transfer enhancement in a channel with built-in winglet pair, Int. J. Heat Fluid Flow 28 (2007) 299-305.
- [11] J. I. Yanagihara, K. Torii, Heat transfer augmentation by longitudinal vortices rows, Proc. Third World Conference on Experimental Heat Transfer 1 (1993) 560-567.
- [12] G. Biswas, P. Deb, S. Biswas, Generation of longitudinal streamwise vortices—a device for improving heat exchanger design. ASME J. Heat Transf. 116 (1994) 588-597.
- [13] G. Biswas, K. Torii, D. Fujii, K. Nishino, Numerical and experimental determination of flow structure and heat transfer effects of longitudinal vortices in a channel flow, Int. J. Heat Mass Transf. 39 (1996) 3441-3451.
- [14] M. Fiebig, Embedded vortices in internal flow: heat transfer and pressure loss enhancement, Int. J. Heat Fluid Flow 16 (1995) 376-388.
- [15] K. Torii, J. I. Yanagihara, The effects of longitudinal vortices on heat transfer of laminar boundary layers, JSME Int. J. Ser. II 32 (1989), 395-402.

- [16]G. Godard, M. Stanislas, Control of a decelerating boundary layer. Part 1: Optimization of passive vortex generators, *Aerosp. Sci. Technol.* 10 (2006) 181-191.
- [17]C. M. Velte, M. O. L. Hansen, D. Cavar, Flow analysis of vortex generators on wing sections by stereoscopic particle image velocimetry measurements, *Environ. Res. Lett.* 3 (2008) 015006.
- [18]M. Henze, J. Von Wolfersdorf, B. Weigand, C. F. Dietz, S. O. Neumann, Flow and heat transfer characteristics behind vortex generators—A benchmark dataset, *Int. J. Heat Fluid Flow* 32 (2011) 318-328.
- [19]A. D. Cutler, P. Bradshaw, Strong vortex/boundary layer interactions. Part 1, Vortices high, *Exp. Fluids* 14 (1993) 331-332.
- [20]A. D. Cutler, P. Bradshaw, Strong vortex/boundary layer interactions. Part 2, Vortices low, *Exp. Fluids* 14 (1993) 339-401.
- [21]I. M. M. A. Shabaka, R. D. Mehta, P. Bradshaw, Longitudinal vortices imbedded in turbulent boundary layers. Part 1, Single vortex, *J. Fluid Mech.* 155 (1988) 37-57.
- [22]R. D. Mehta, P. Bradshaw, Longitudinal vortices imbedded in turbulent boundary layers. Part 2. Vortex flow with “common flow” upwards, *J. Fluid Mech.* 188 (1988) 529-546.
- [23]S. Lau, Experimental study of the turbulent flow in a channel with periodically arranged longitudinal vortex generators, *Exp. Therm. Fluid Sci.* 11 (1995) 255-261.
- [24]G. I. Taylor, The spectrum of turbulence, *Proc. R. Soc. Lond. A* 164 (1938) 476–490.
- [25]F. E. Jørgensen, *How to Measure Turbulence with Hot-Wire Anemometers: a practical guide*, Dantec Dynamics, Skovlunde, Denmark, 2002.
- [26]R. S. Figliola, D. E. Beasley, *Theory and Design for Mechanical Measurements*, fifth ed., Wiley, New York, 2011.
- [27]A. J. Smits, J. A. Eaton, P. Bradshaw, The response of a turbulent boundary layer to lateral divergence, *J. Fluid Mech.* 94 (1979) 243-268.

- [28] J. K. Harvey, F. J. Perry, Flowfield produced by trailing vortices in the vicinity of the ground, *AIAA J.* 9 (1971) 1659-1660.
- [29] P. Orlandi, Vortex dipole rebound from a wall, *Phys. Fluid A* 2 (1990) 1429-1436.
- [30] P. M. Gerhart, A. L. Gerhart, J. I. Hochstein, Munson, Young and Okiishi's *Fundamentals of Fluid Mechanics*, eighth ed., Wiley, New York, 2016.
- [31] N. Patten, P. Griffin, T. M. Young, Effects of freestream turbulence on the characteristics in the boundary layer near the transition onset location, *ASME J. Fluids Eng.* 135 (2013) 071203.
- [32] F. Dupont, C. Gabillet, P. Bot, Experimental study of the flow in a compact heat exchanger channel with embossed-type vortex generators, *ASME J. Fluids Eng.* 125 (2003) 701-709.
- [33] F. Fouladi, P. Henshaw, D. S.-K. Ting, Effect of a triangular rib on a flat plate boundary layer, *ASME J. Fluids Eng.* 138 (2016) 011101.
- [34] M. J. Barrett, D. K. Hollingsworth, On the calculation of length scales for turbulent heat transfer correlation, *ASME J. Heat Transfer* 123 (2001) 878-883.
- [35] J. S. Carullo, S. Nasir, R. D. Cress, W. F. Ng, K. A. Thole, L. J. Zhang, H. K. Moon, The effects of freestream turbulence, turbulence length scale, and exit Reynolds number on turbine blade heat transfer in a transonic cascade, *ASME J. Turbomach.* 133 (2011) 011030.
- [36] C. Sak, R. Liu, D. S.-K. Ting, G. W. Rankin, The role of turbulence length scale and turbulence intensity on forced convection from a heated horizontal circular cylinder, *Exp. Therm. Fluid Sci.* 31 (2007) 279-289.
- [37] F. Fouladi, P. Henshaw, D. S.-K. Ting, S. Ray, Flat plate convection heat transfer enhancement via a square rib, *Int. J. Heat Mass Transfer*, 104 (2017) 1202-1216.
- [38] D. S.-K. Ting, *Basics of Engineering Turbulence*, Academic Press, New York, 2016.

CHAPTER 4

**FLOW OVER A FLAT SURFACE BEHIND DELTA WINGLETS OF VARYING
ASPECT RATIOS**

Hao Wu¹, David S-K. Ting^{1†} & Steve Ray²

¹Turbulence and Energy Laboratory, Centre for Engineering Innovation, University of Windsor,

401 Sunset Ave, Windsor, Ontario, N9B 3P4, Canada

†Corresponding Author, dting@uwindsor.ca

²Essex Energy Corporation, 2199 Blackacre Dr, Suite #200, Oldcastle, Ontario, N0R 1L0, Canada

H. Wu, D. S-K. Ting, S. Ray., Flow over a flat surface behind delta winglets of varying aspect ratios, to be submitted.

4.1 Introduction

There are many applications where the effectiveness of convective heat transfer by air is important. One special issue is the convective cooling of solar photovoltaic (PV) panels, where the convective heat transfer is predominantly restricted by the boundary layer. Due to the function of the PV panel, its surface condition cannot be easily altered by means of curving [1] or dimpling [2] to disturb the boundary layer. Moreover, it cannot be covered with fins for that would block the solar radiation. Therefore, turbulence generators (TGs) mounted on the frame is a practical measure to disturb the boundary layer and enhance the heat transfer. For this purpose, the flow mechanism behind desirable TGs must be scrutinized for better understanding and designing. One of the potential TGs that can fit into the PV narrow frame is rib [3–5]. Ribs can perturb the boundary layer by causing flow separation, recirculation and reattachment. The separated and reattached flow would

lead to some strong unsteady behaviors, such as flapping separation bubbles, rolled-up vortices and shedding of large scale vortices. Grooves [6,7] are another promising turbulence generating technology. Turbulence intensity can be enlarged in the near-wall region immediately downstream of the groove.

A more promising type of TGs is probably the longitudinal vortex generators (LVGs) [8]. LVGs can manipulate the boundary layer in a rather unique way, i.e., swirling the flow by rotating with an axis more-or-less parallel to the main flow direction. The boundary is thus highly three-dimensional and more importantly, the resulting turbulent flow can last longer because of the prevailing, slowly decaying large vortical flow. There are two typical LVGs: wings and winglets, as sketched in Figure 4.1. A detailed literature review can be found in Wu et al. [9]. An isolated winglet can spawn one vortex and the rotating direction is controlled by the orientation of the winglet. One wing, on the other hand, can produce two counter rotating vortices with the inboard flow downward into the horizontal plane. The performance of these LVGs weighs heavily on the geometries like attack angle and aspect ratio. This study is an extension from our previous work [9], the current paper scrutinizes the impact of the aspect ratio on the vortex structures and underlying turbulence parameters of the flow downstream of a delta winglet over a flat plate.

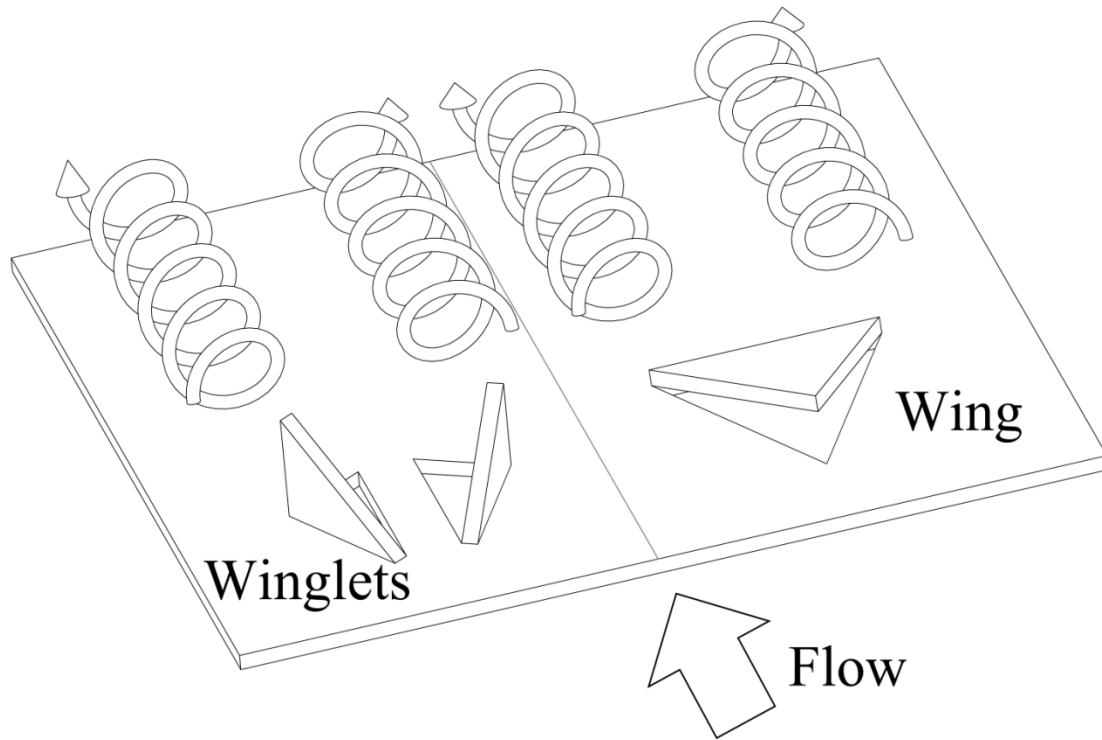


Figure 4. 1 Typical vortex generators.

4.2 Experimentation

Figure 4.2 shows the experimental setup, including the tested winglets and the associated parameters; note the winglet Vertex and Rear Corner. The experiments were conducted inside a closed loop wind tunnel. The test section of the wind tunnel has a 76 cm by 76 cm cross section. The delta winglets were made from a 0.1 mm thick aluminum sheet. The height, h , was kept at 10 mm, and the chord length, c , varies from 40 to 10 mm, giving an aspect ratio (AR), $4h/c$, of 1 to 4. The winglets were attached on the base surface of the wind tunnel by one of the folds, 1000 mm away from the inlet of the test section. The angle of attack, α , was maintained at 30 degrees in the present study. The stream velocity was fixed at 10 m/s, resulting in a Reynolds number based on the winglet height of 6000. The background turbulence intensity was around 0.4%. A triple sensor hotwire probe (type 55P91) with a constant-temperature anemometer was employed to obtain the velocity at 100 mm ($10h$) downstream of the winglet. The measured planes were 50 mm \times 30 mm for aspect ratio of 1 and 40 mm \times 30 mm for aspect ratio of 2

and 4, with a spatial resolution of 2 mm. The velocity signals were sampled at 80 kHz for 12.5 seconds, resulting in a sampling number of 10^6 . The signal was low passed at 30 kHz. All three velocity components, u , v , w , were measured simultaneously.

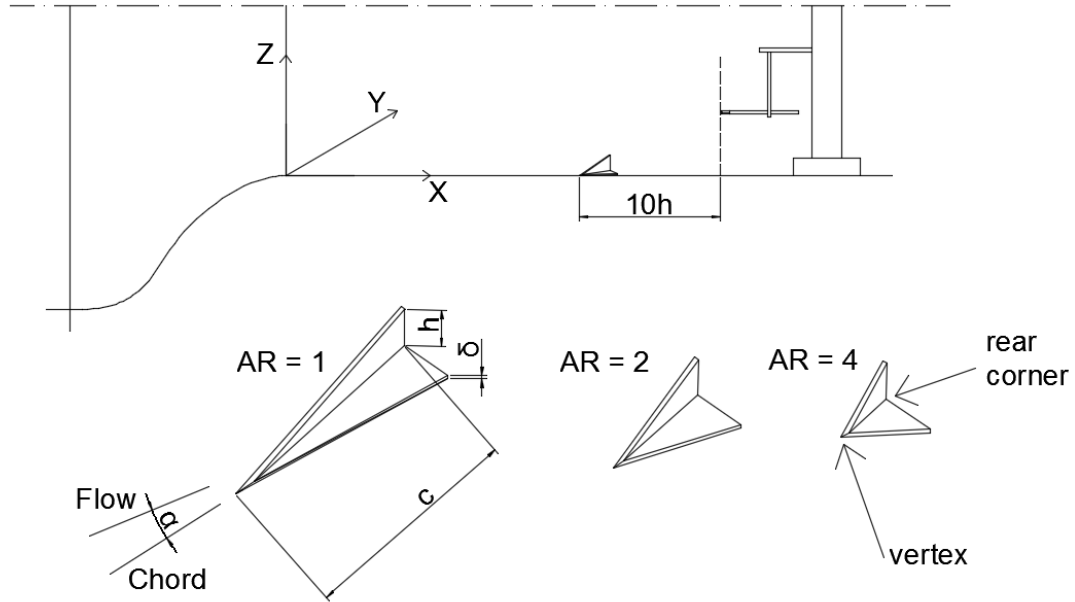


Figure 4. 2 The experimental setup inside a wind tunnel and the sketch of the winglet. $\delta = 0.1$ mm, $\alpha = 30^\circ$, $h = 10$ mm, $c = 10, 20, 40$ mm.

4.3 Data Processes

The instantaneous velocities (U , V , and W) are obtained from hot-wire output voltage signals via calibration coefficient and ambient temperature. The time-averaged velocity (\bar{U}) is deduced from:

$$\bar{U} = \frac{1}{N} \sum_{i=1}^N U_i \quad (4.1)$$

where N is the sample size. The instantaneous fluctuating velocity (u) is calculated from:

$$u_i = U_i - \bar{U} \quad (4.2)$$

The root mean square velocity (u_{rms}) is computed from:

$$u_{\text{rms}} = \sqrt{\frac{\sum_{i=1}^N u_i^2}{N-1}} \quad (4.3)$$

Vorticity is calculated from:

$$\omega = \frac{\partial w}{\partial y} - \frac{\partial v}{\partial z} \quad (4.4)$$

Dimensionless time-averaged velocity and turbulence intensity are deduced via dividing them by the free stream velocity, and dimensionless vorticity is obtained from:

$$\Omega = \frac{\omega \times h}{U_\infty} \quad (4.5)$$

The magnitude of the cross-stream velocity vector is deduced from:

$$L = \sqrt{(\bar{V}^2 + \bar{W}^2)} \quad (4.6)$$

and the angle is calculated from:

$$\theta = \arctan\left(\frac{\bar{W}}{\bar{V}}\right) \quad (4.7)$$

According to the Taylor frozen hypothesis [10], if the velocity fluctuation is small compared to the main flow, the carried eddies can be regarded as merely passing the probe without evolution. The Taylor microscale (λ) can be calculated from:

$$\lambda = \bar{U} \cdot \tau_\lambda \quad (4.8)$$

where Taylor time scale (τ_λ) can be determined from:

$$\tau_\lambda = \sqrt{\frac{2\bar{u}^2}{\left(\frac{du}{dt}\right)^2}} \quad (4.9)$$

In the present study, the data is discrete, so this equation is rewritten as:

$$\tau_\lambda = \sqrt{\frac{\frac{1}{N} \sum_{i=1}^N 2u_i^2}{\frac{1}{N-1} \sum_{i=1}^{N-1} \left(\frac{u_{i+1} - u_i}{\Delta t}\right)^2}} \quad (4.10)$$

Integral length scale can be estimated from:

$$\Lambda = \bar{U} \cdot \tau_{\Lambda} \quad (4.11)$$

where integral time scale (τ_{Λ}) can be obtained from:

$$\tau_{\Lambda} = \int_0^{\infty} \rho(\tau) d\tau \quad (4.12)$$

ρ is the autocorrelation factor, which is defined as:

$$\rho(\tau) = \frac{\overline{u(t)u(t+\tau)}}{u^2(t)} \quad (4.13)$$

For discrete data, the equations are rewritten as:

$$\tau_{\Lambda} = \sum_{i=1}^{N_k-1} \rho(i\Delta t) \Delta t \quad (4.14)$$

where N_k is the point where the autocorrelation factor crosses over the zero value for the first time, and:

$$\rho(m\Delta t) = \frac{\frac{1}{N-m} \sum_{i=1}^{N-m} (u_i u_{i+m})}{\frac{1}{N} \sum_{i=1}^N u_i^2} \quad (4.15)$$

where m varies from 0 to $N - 1$. The displacement thickness can be obtained from:

$$\delta^* = \int_0^{\infty} \left(1 - \frac{\bar{U}(z)}{U_{\infty}}\right) dz \quad (4.16)$$

In the present study, 15 points are measured and the highest points are in the free stream with $\frac{\bar{U}(z)}{U_{\infty}} = 1$. Therefore this equation is rewritten as:

$$\delta^* = \sum_{i=1}^{15} \left(1 - \frac{\bar{U}(i\Delta z)}{U_{\infty}}\right) \Delta z \quad (4.17)$$

where Δz is 2 mm. The momentum thickness can be deduced from:

$$\theta = \int_0^{\infty} \frac{\bar{U}(z)}{U_{\infty}} \left(1 - \frac{\bar{U}(z)}{U_{\infty}}\right) dz \quad (4.18)$$

and it is rewritten as:

$$\theta = \sum_{i=1}^{15} \frac{\bar{U}(i\Delta z)}{U_{\infty}} \left(1 - \frac{\bar{U}(i\Delta z)}{U_{\infty}}\right) \Delta z \quad (4.19)$$

Shape factor is calculated from:

$$H = \frac{\delta^*}{\theta} \quad (4.20)$$

The total uncertainties of \bar{U} and u_{rms} were deduced from:

$$E = \sqrt{B^2 + P^2} \quad (4.21)$$

where B is the bias uncertainty and P is the precision uncertainty. Bias uncertainty included the uncertainty from calibration, data acquisition, data reduction, etc., and was estimated according to Jorgensen [11]. Precision uncertainty shows the repeatability of the measurement, and was estimated following the Student's t distribution method with a 95% confidence interval [12]. The uncertainties for rest of the parameters were obtained via error propagation [12]:

$$\frac{E_{\bar{U}}}{\bar{U}} = \sqrt{2 \left(\frac{E_{\bar{U}}}{\bar{U}} \right)^2} \quad (4.22)$$

$$\frac{E_{u_{\text{rms}}}}{u_{\text{rms}}} = \sqrt{\left(\frac{E_{\bar{U}}}{\bar{U}} \right)^2 + \left(\frac{E_{u_{\text{rms}}}}{u_{\text{rms}}} \right)^2} \quad (4.23)$$

$$\frac{E_{\lambda}}{\lambda} = \sqrt{\left(\frac{E_{\bar{U}}}{\bar{U}} \right)^2 + 2 \left(\frac{E_{u_{\text{rms}}}}{u_{\text{rms}}} \right)^2} \quad (4.24)$$

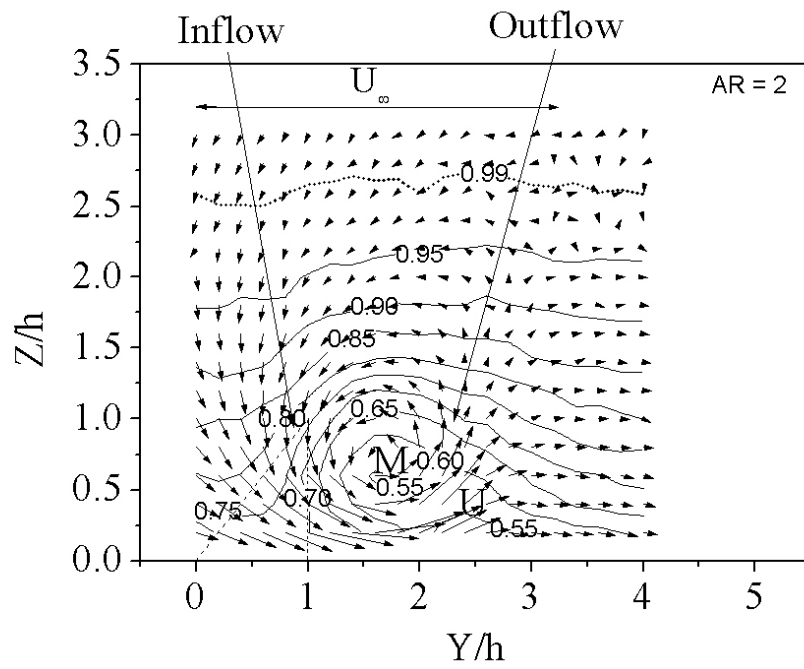
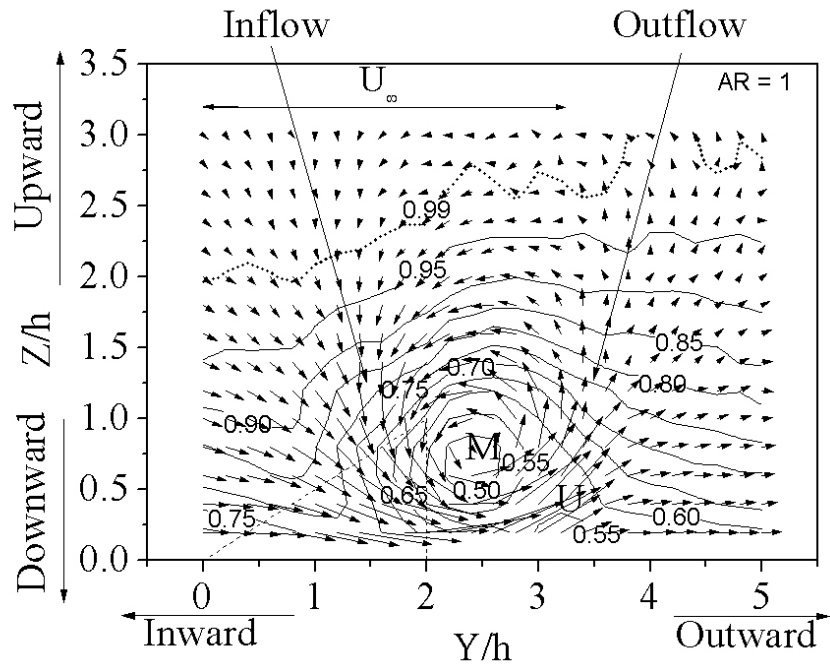
$$\frac{E_{\Lambda}}{\Lambda} = \sqrt{\left(\frac{E_{\bar{U}}}{\bar{U}} \right)^2 + 2 \left(\frac{2E_{u_{\text{rms}}}}{u_{\text{rms}}} \right)^2} \quad (4.25)$$

4.4 Results and Discussion

4.4.1 Time-Averaged Velocity

The normalized time-averaged streamwise velocity is scrutinized to appreciate the interaction between the longitudinal vortex and the boundary layer. Figure 4.3 illustrates the normalized streamwise time-averaged velocity contours and cross-stream velocity vectors at 10 h downstream of the winglet at $U_{\infty} = 10$ m/s and $AR = 1, 2$ and 4. The lowest height of measurement points is 2 mm due to the inherent diameter of the triple sensor

probe. The axes are normalized by the winglet height h . The locations of the winglets are shown in dashed line, its leading vertex located at the origin of the coordinates ($Y/h = 0$, $Z/h = 0$). The large longitudinal vortices can be clearly seen at the outward side of the winglet in the cross-stream velocity vector plots. The boundary layer (99% free stream velocity) is shown as a dotted line. The boundary layer thicknesses for all three aspect ratios are around 25 mm. As we can see, large vortices are deeply embedded inside the boundary layer. At the top right corner some chaotic vector can be seen, especially for $AR = 2$ and 4. This is because it is far away from the vortex and there is no secondary flow. The area where the flow moves downward, towards the surface is called the Inflow Region, and the area where the flow moves upward, away from the surface is called the Outflow Region. At $AR = 1$, the reduction of boundary layer thickness around the Inflow Region due to the downwash effect can be observed. Correspondingly, at the Outflow Region the boundary layer thickness is increased by the upwash effect. As the aspect ratio increases (at $AR = 2$ and 4), these effects are less significant. Two peak velocity deficits are observed, one is at the core of the main vortex (marked as M), and the other is at the Upwash Region (marked as U). As shown in Figures 4.3 and 4.4, with the increase of the aspect ratio, the normalized velocity at the main vortex core has less deficit, 0.47 for $AR = 1$ instead 0.61 for $AR = 4$, while the velocity deficit at Upwash Region remains at 0.52.



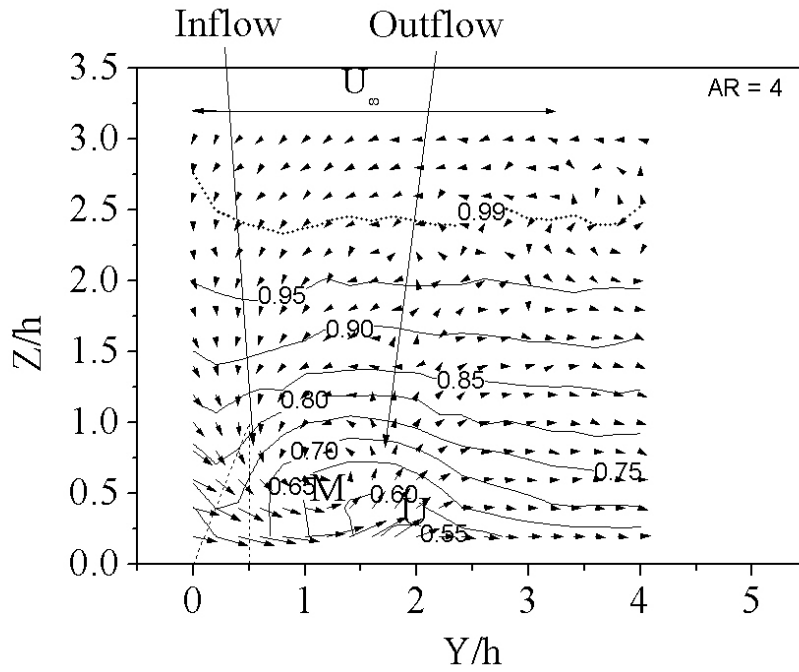


Figure 4. 3 Normalized streamwise time-averaged velocity contours and cross-stream velocity vectors at AR = 1, 2 and 4.

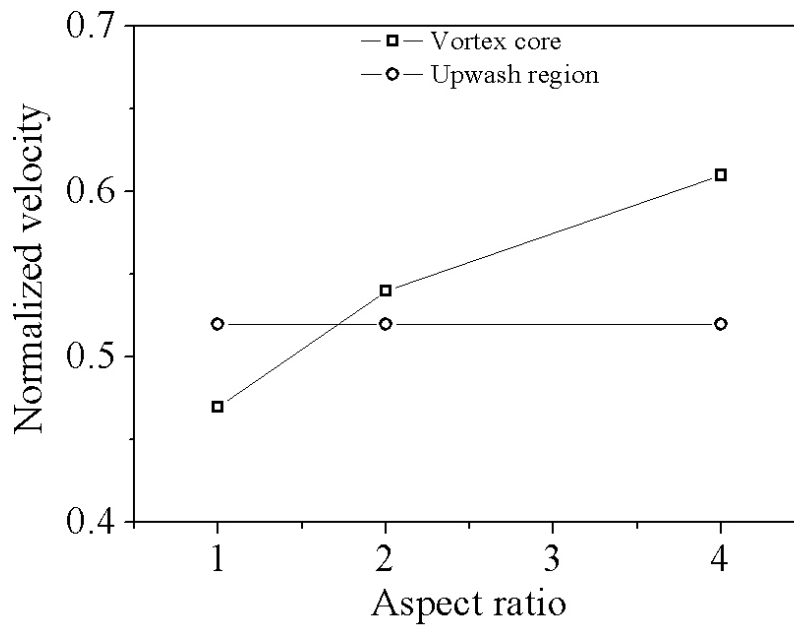


Figure 4. 4 Normalized streamwise velocity at peak deficit locations with respect to aspect ratio.

The comparison of Inflow and Outflow for each vortex at different aspect ratios may give a clearer view of the effect of aspect ratio. The sum of normalized W velocities (\bar{W}/U_∞) are deduced, as shown in Figure 4.5, to pinpoint the locations of Inflow and Outflow. The locations correspond to the lowest sum of \bar{W}/U_∞ is $Y/h = 1.6$ for $AR = 1$, 0.6 for $AR = 2$, and 0.2 for $AR = 4$, therefore these locations are chosen to represent Inflow. Outflow is described by the largest sum of \bar{W}/U_∞ ($Y/h = 3$ for $AR = 1$, 2.2 for $AR = 2$ and 1.8 for $AR = 4$). The normalized velocities at Inflow and Outflow for all three aspect ratios are depicted in Figure 4.6, and are contrasted with the base reference case without winglet (smooth surface case).

For the smooth surface reference case, the displacement thickness and momentum thickness are approximately 3.8 mm and 2.9 mm, respectively, resulting a shape factor H of 1.3 . Conventionally, $H = 2.59$ is typical of laminar flows, and $H = 1.3 \sim 1.4$ is typical of turbulent flows [13]. Thus the reference flow has a turbulent boundary layer. The boundary layer thickness, defined as the height where the flow reaches 99% of the free stream velocity, is around 26 mm. This is very close to the calculated value from
$$\frac{\delta}{x} = \frac{0.37}{Re^{1/5}} \quad (25.5 \text{ mm}).$$

For the Inflow (Figure 4.6a) in the present of the winglet, the normalized velocities are larger than that of the reference smooth surface case, except at $AR = 1$ between $Z/h = 0.6$ to 1.4 , where it is smaller. The smaller velocity may be attributed to the velocity deficit at the main vortex core. At the lowest measured point ($Z/h = 0.2$), the normalized velocities for all three aspect ratios converge to around 0.7 . For the Outflow (Figure 4.6b), winglet influenced flows have smaller normalized velocities, and this is more so as the aspect ratio is reduced. Similar to the Inflow, the normalized velocities converge to around 0.5 near the surface. The comparison between Inflow and Outflow in Figure 4.6c clearly illustrates a lower streamwise velocity in the Outflow Region. The velocity difference between Inflow and Outflow decreases with the increase of height, Z/h . The maximum uncertainty in normalized time-averaged velocity is estimated to be 0.02 .

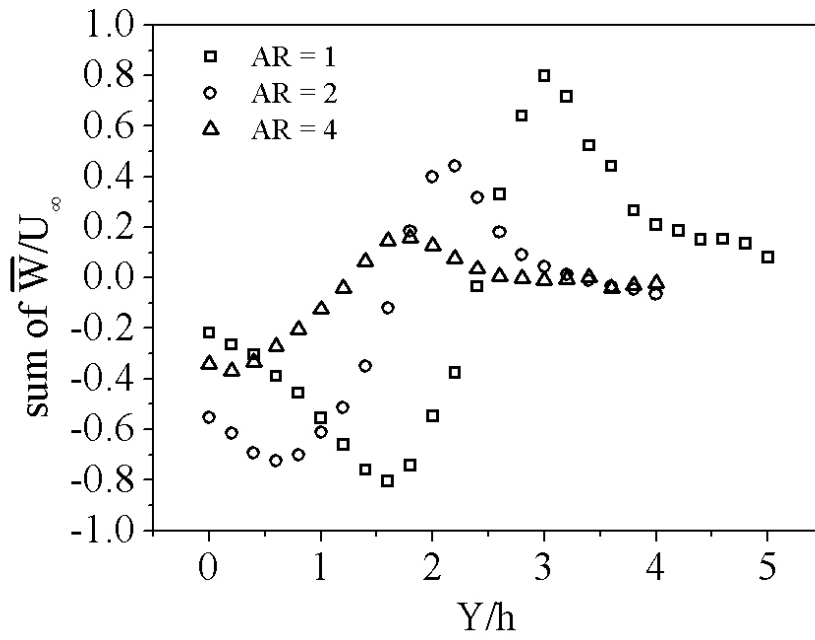
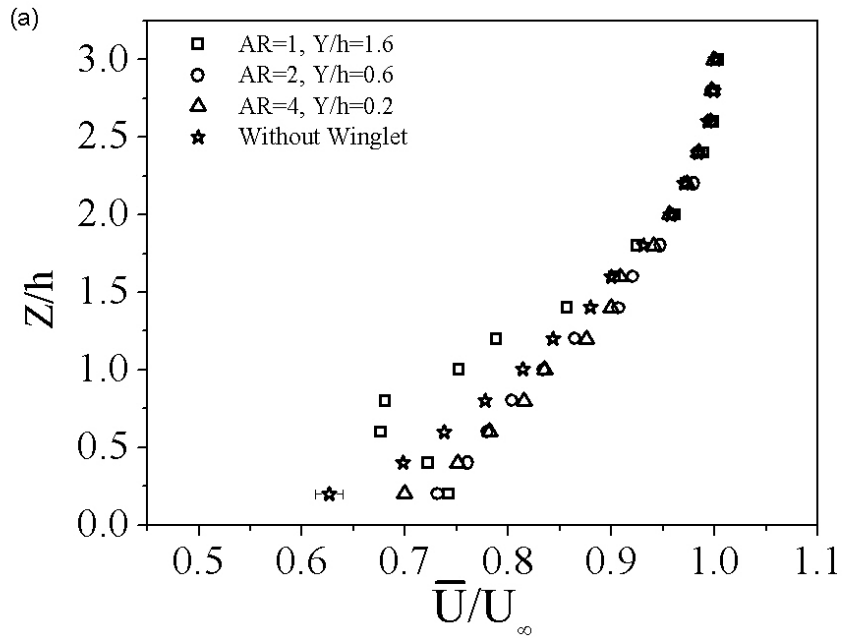


Figure 4.5 Sum of normalized W velocities at AR = 1, 2 and 4.



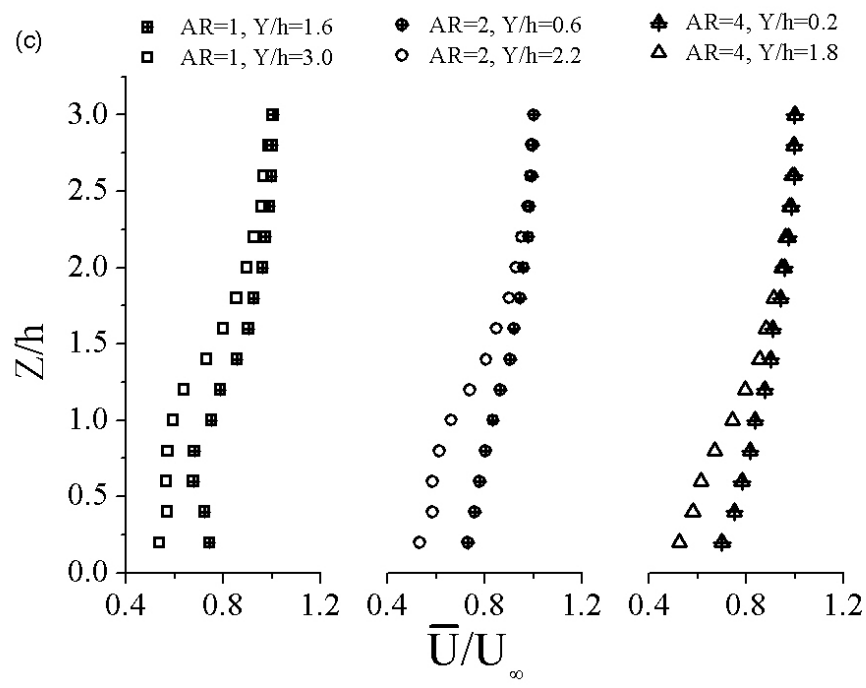
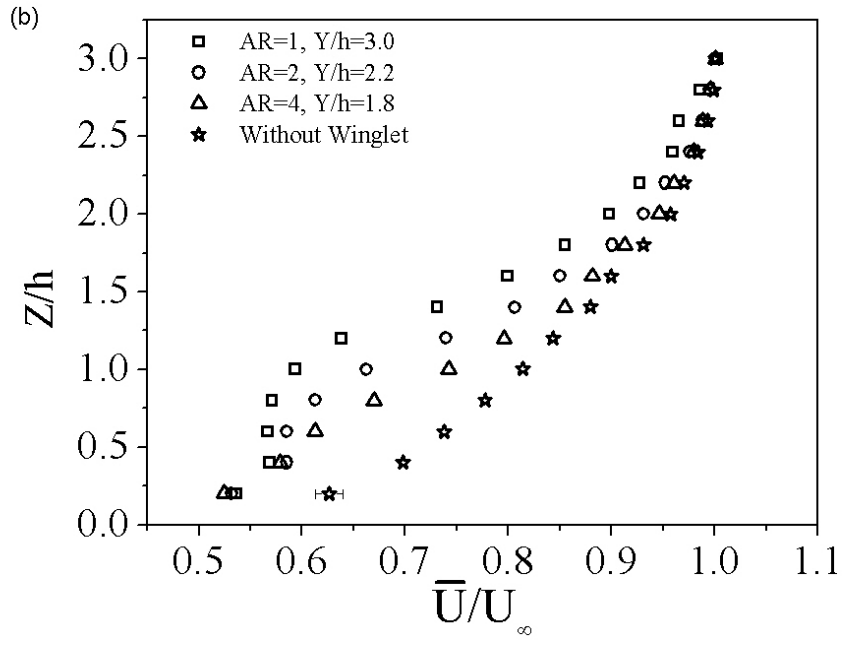


Figure 4. 6 Normalized streamwise velocities for Inflow and Outflow at AR = 1, 2 and 4. (a) Inflow, (b) Outflow, (c) Inflow and Outflow.

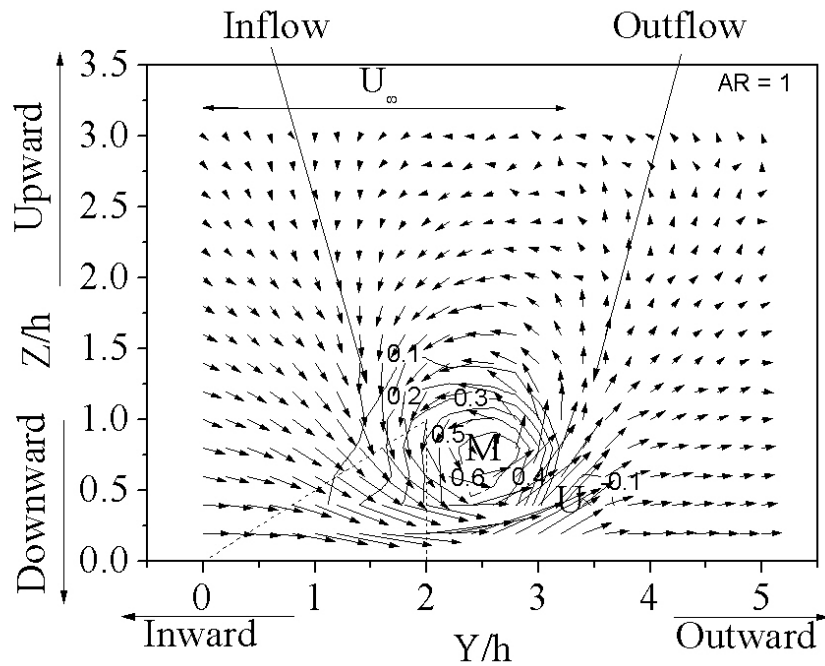
4.4.2 Vortex Structure.

To gain better insight of the secondary flow, the cross-stream dimensionless vorticity plots at $AR = 1, 2$ and 4 are plotted in Figure 4.7. For $AR = 1$, the vortex can be observed by the closed vorticity curve. The location where vorticity peaks is considered as the core of the vortex. For $AR = 2$ and 4 , the vorticity curve is not complete at the bottom due to the limitation of the measurement facility. Nevertheless, the peak vorticity location concurs with the center of cross-stream velocity vector and the mean (time-averaged) flow angle trough (Figure 4.8). Figure 4.8 shows the mean flow angle (between mean flow and streamwise) for $AR = 1, 2$ and 4 . As can be seen, besides the trough at the main vortex core, the mean flow angle is smaller upon the main vortex core and larger below the main vortex core. This indicates that the secondary flow is stronger at the bottom of the vortex, which is supported by the larger cross-stream velocity vector magnitude there.

With the increase of aspect ratio, the vorticity contour (Figure 4.7) shows a decrease of main vortex area, which implies the shrinking of the main vortex. Moreover, an overall trend of decreasing cross-stream velocity vector magnitude can be observed. This evinces that over the studied range of conditions, the vortex weakens with the increase in aspect ratio. Figure 4.9 shows the peak mean flow angle and vorticity with the varying of aspect ratio. We can see both of these two parameters decrease with the increasing aspect ratio, which conforms to the decreasing vortex intensity. This trend coincides with the decrease in streamwise velocity deficit, that is, less energy is converted from streamwise main flow to cross-stream secondary flow.

Figure 4.10 illustrates the positioning of the main vortex core with respect to aspect ratio. The location of the vortex core with respect to the winglet vertex (the origin in Figure 4.7) is represented by square. As the aspect ratio increases from 1 to 4 , the main vortex core moves downward, from around $Z/h = 0.8$ to 0.4 , and inward, from around $Y/h = 2.4$ to 1.2 with respect to the winglet vertex. The inward movement can be partly attributed to the shortening of winglet chord length. Therefore if we set the coordinates origin to the

winglet rear corner ($X = 0, Y = 0, Z = 0$), the location of the main vortex core moves from $Y/h = 0.4$ to 0.7 (as illustrated by circle in Figure 4.10), thus indicating the outward movement of the main vortex core relative to the winglet rear corner with the increase in aspect ratio. This downward movement of the vortex with the increase of aspect ratio, together with the decreased vortex intensity, may explain the less significant effects of thinning the boundary layer in Inflow and thickening the boundary layer in Outflow (see Section 4.1).



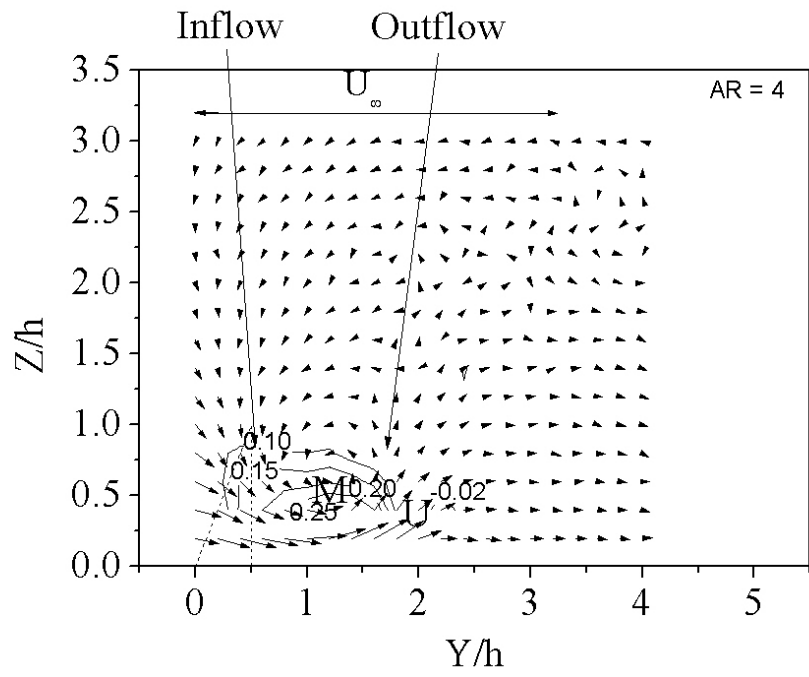
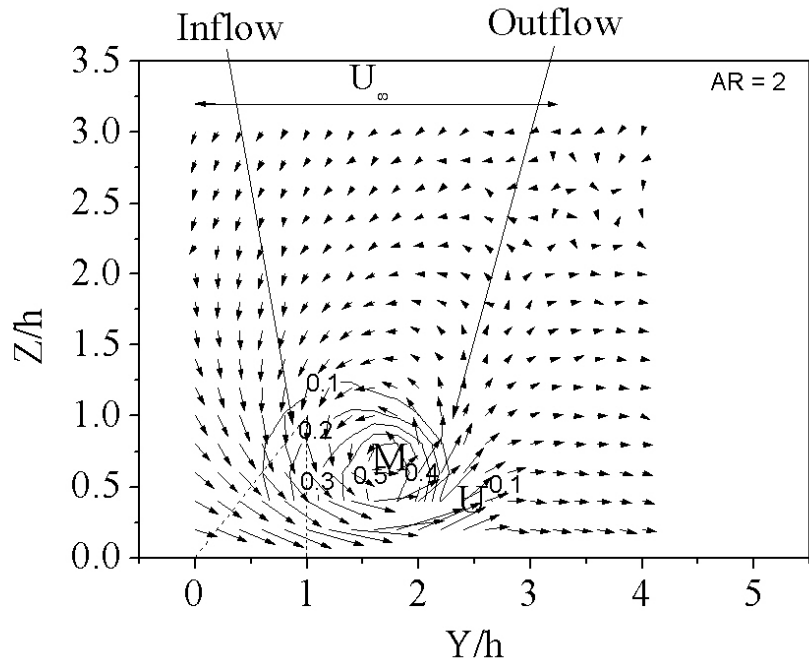
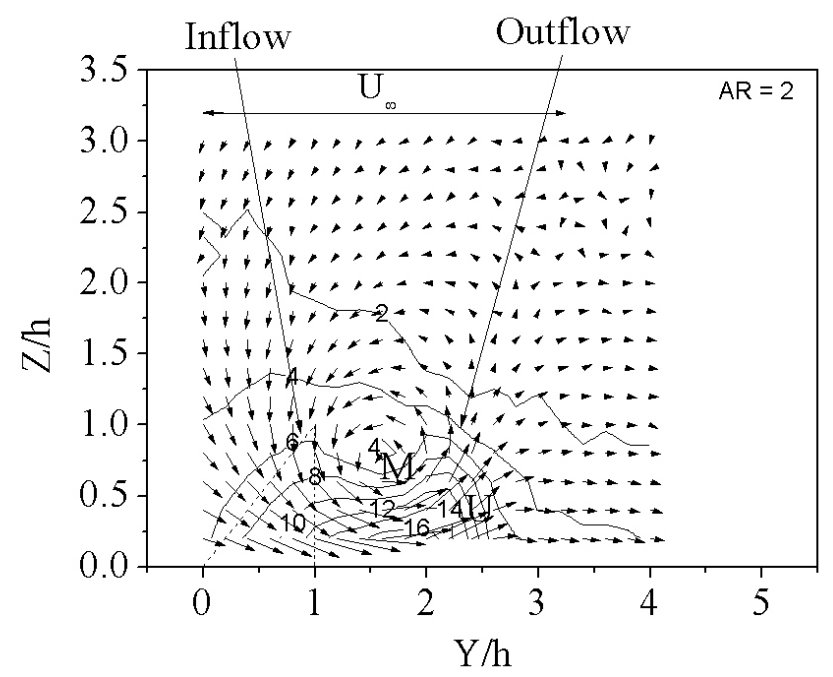
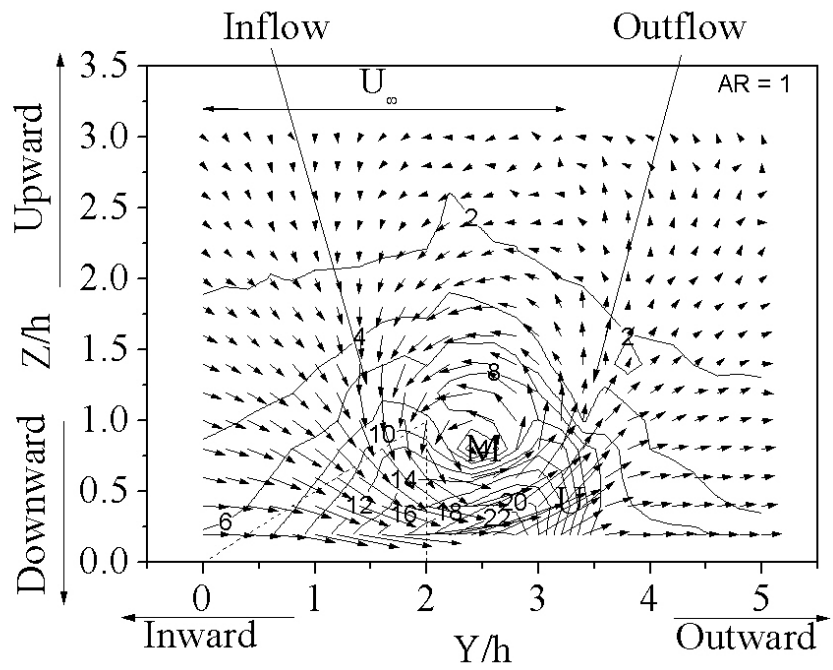


Figure 4. 7 Cross-stream velocity vector and dimensionless vorticity contour at AR = 1, 2 and 4.



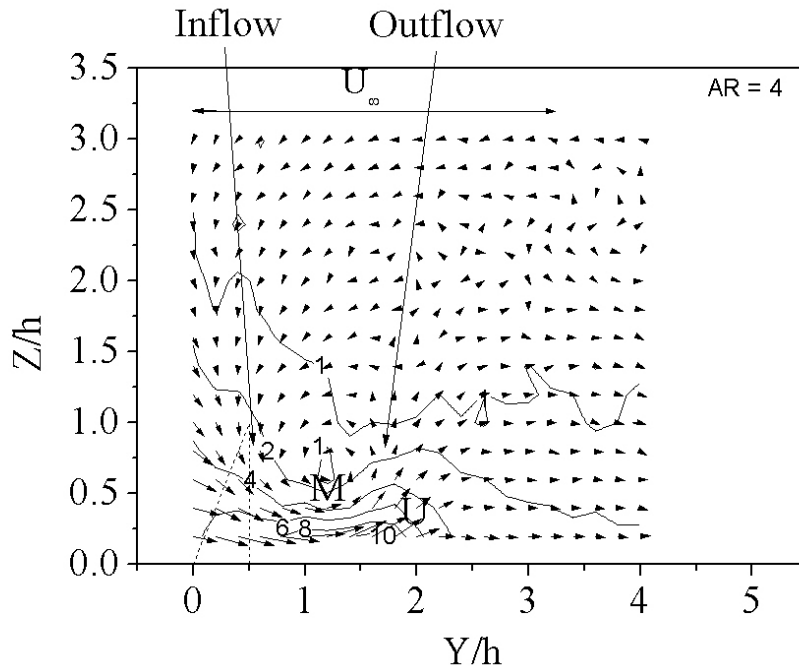


Figure 4. 8 Mean flow angle (between mean flow and streamwise, in degree) contour and cross-stream velocity vector at AR = 1, 2 and 4.

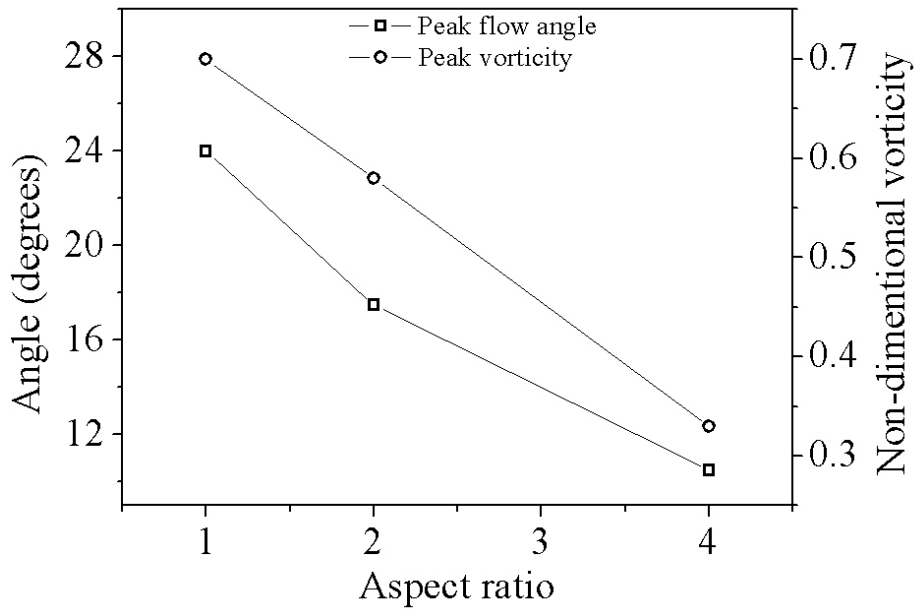


Figure 4. 9 Peak mean flow angle (between mean flow and streamwise) and peak vorticity with respect to aspect ratio.

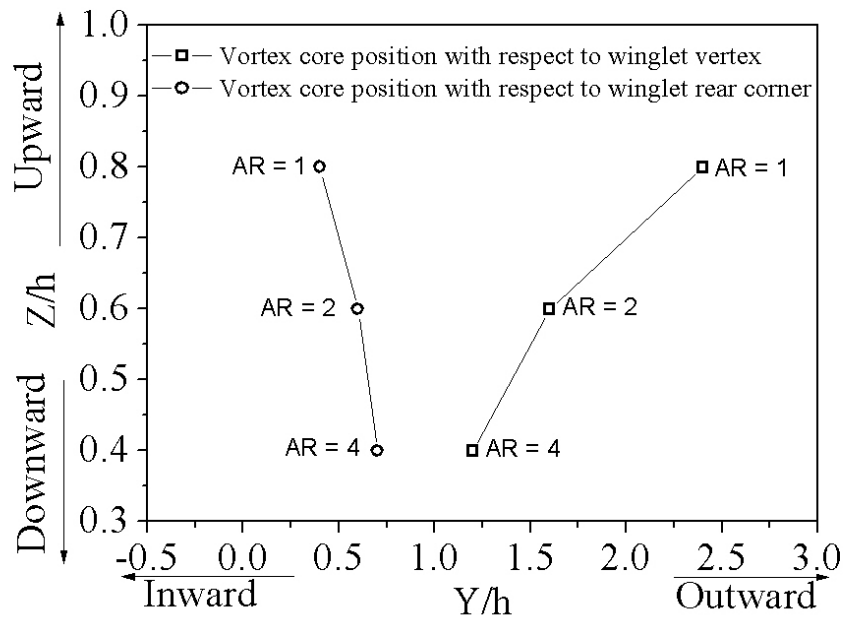
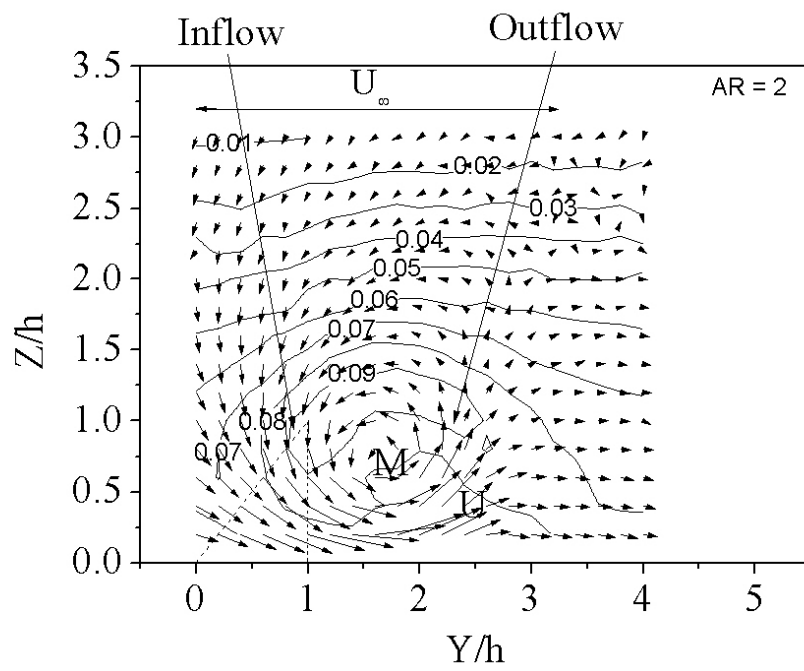
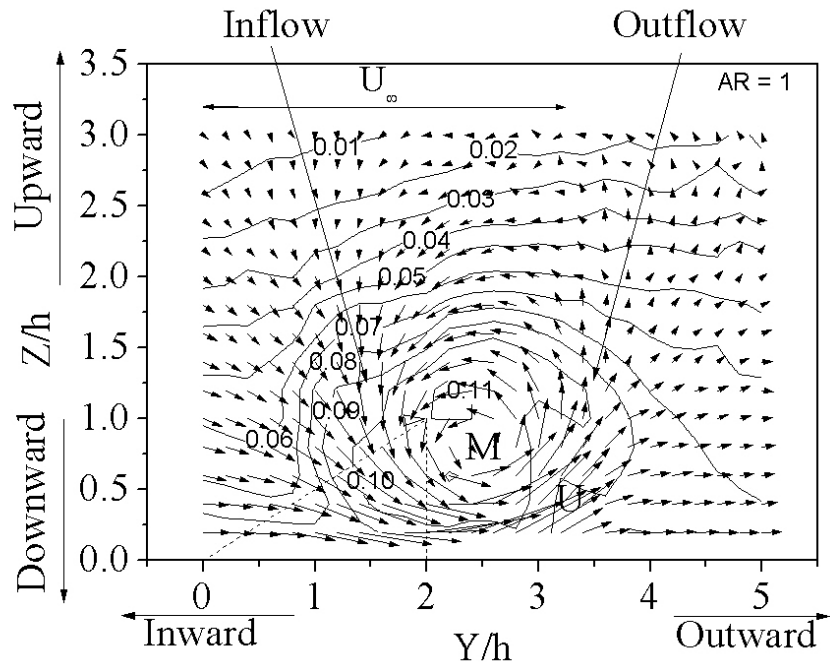


Figure 4. 10 The main vortex core locations with respect to aspect ratio.

4.4.3 Turbulent Parameters

Besides the large vortex structure, the turbulence level in the flow is another important parameter for vortex generators. The turbulence intensity contours (u_{rms}/U_{∞}) at AR = 1, 2 and 4 are shown in Figure 4.11. Peak turbulence intensity can be observed near the main vortex core. The peak turbulence intensity value decreases slightly with the increase of aspect ratio. Considering the decreasing vortex intensity and streamwise velocity deficit, it can be inferred that this peak turbulence intensity is gathering energy from the mean flow via the large vorticity and shear near the main vortex core. In other words, with the increase of aspect ratio less energy is converted into turbulence due to the smaller vortex intensity and shear, and thus it has a smaller turbulence intensity and velocity deficit.



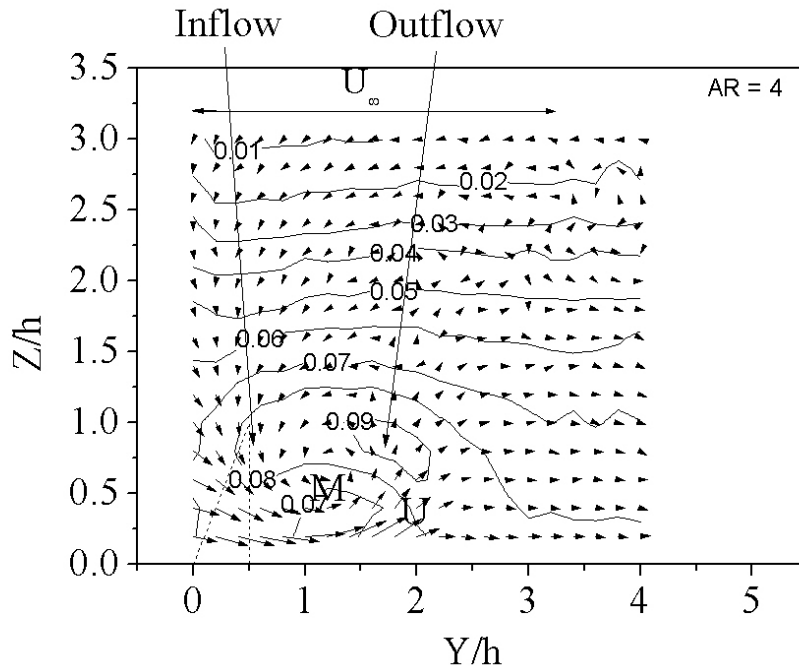
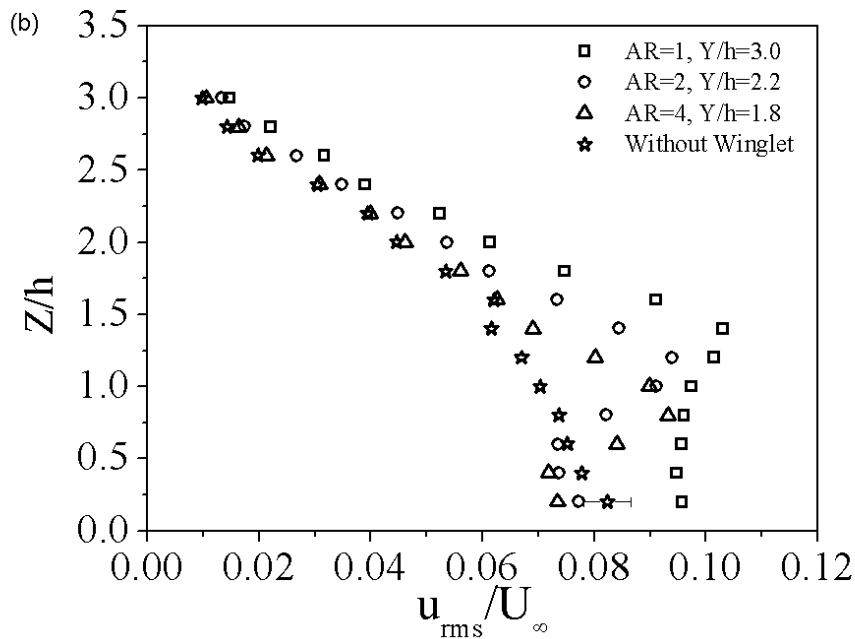
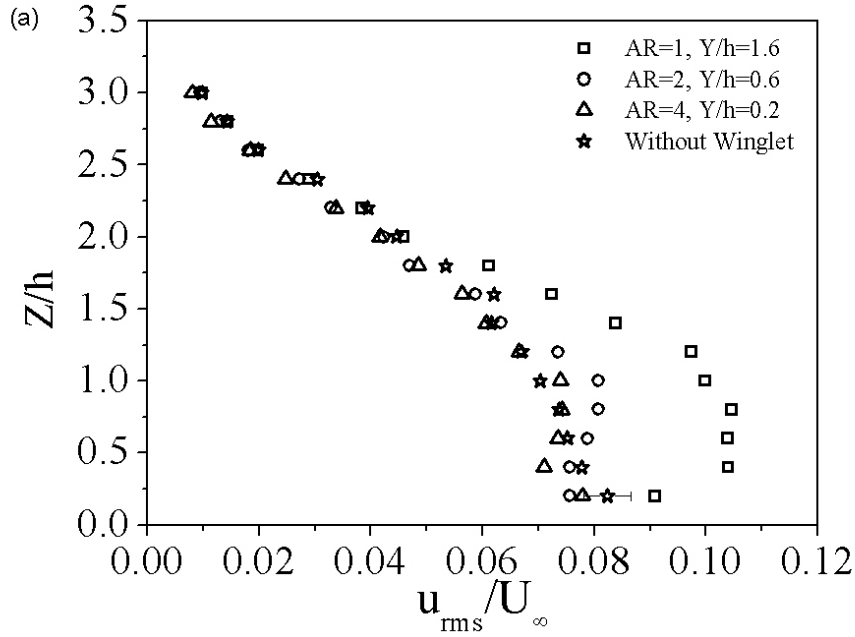


Figure 4. 11 Stream-wise turbulence intensity (u_{rms}/U_{∞}) contour and cross-stream velocity vector at AR = 1, 2 and 4.

Figure 4.12 illustrates turbulence intensity Tu (u_{rms}/U_{∞}) for Inflow and Outflow at AR = 1, 2 and 4, and compares with the reference case without winglet. As can be seen, the turbulence intensity has its highest value of 8% adjacent to the wall in the absence of the vortex generator, and then it decreases to the free stream value farther away. For Inflow (Figure 4.12a), at AR = 1 the turbulence intensity is larger than that of the smooth surface base. At AR = 2 and 4 the turbulence intensity is similar to the reference case flow, and for AR = 2 it is slightly larger than that for AR = 4. The increase-decrease trend for AR = 1 implies the higher turbulence intensity is associated with the main vortex core. For Outflow (Figure 4.12b), all three aspect ratios have larger turbulence intensities than the reference smooth surface, and also the increase-decrease trend. The turbulence intensity decreases with the increase of aspect ratio. The height (distance from the wall) where Tu peaks also decreases with increasing AR, which agrees with the decreasing vortex height and size. The comparison between Inflow and Outflow in Figure 4.12c illustrates that for all the aspect ratios the turbulence intensity curves for Inflow and Outflow have a crossover, above that crossover Outflow has higher turbulence intensity, while below that

crossover Inflow Tu is larger or at least the same as Outflow. This crossover height also decreases with the increase of AR. The maximum uncertainty for turbulence intensity is estimated to be 0.4%.



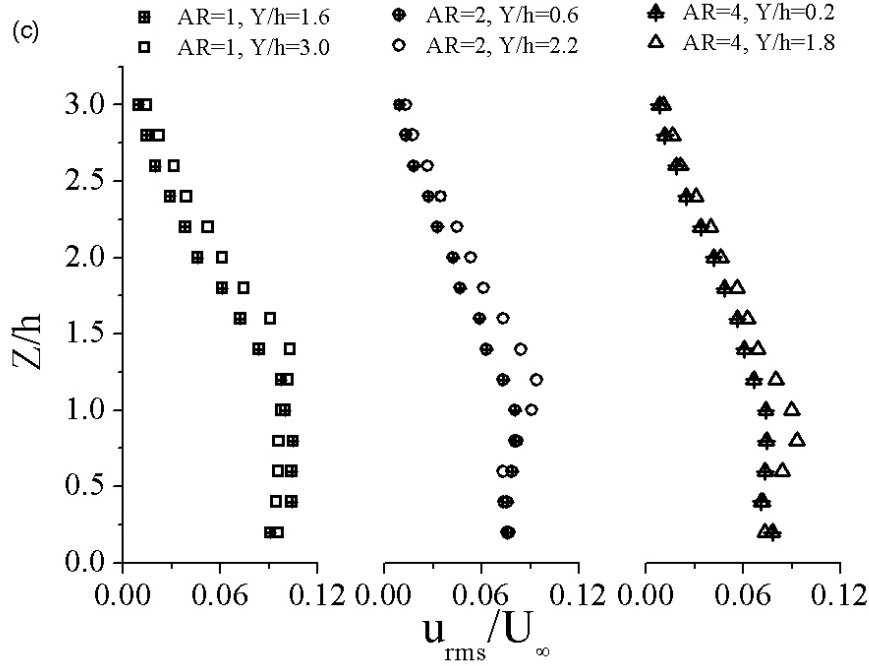
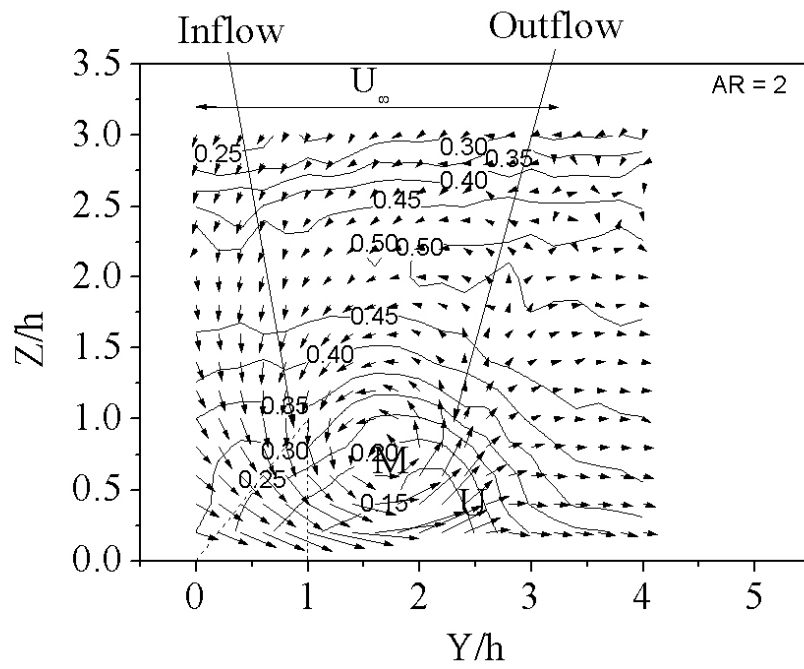
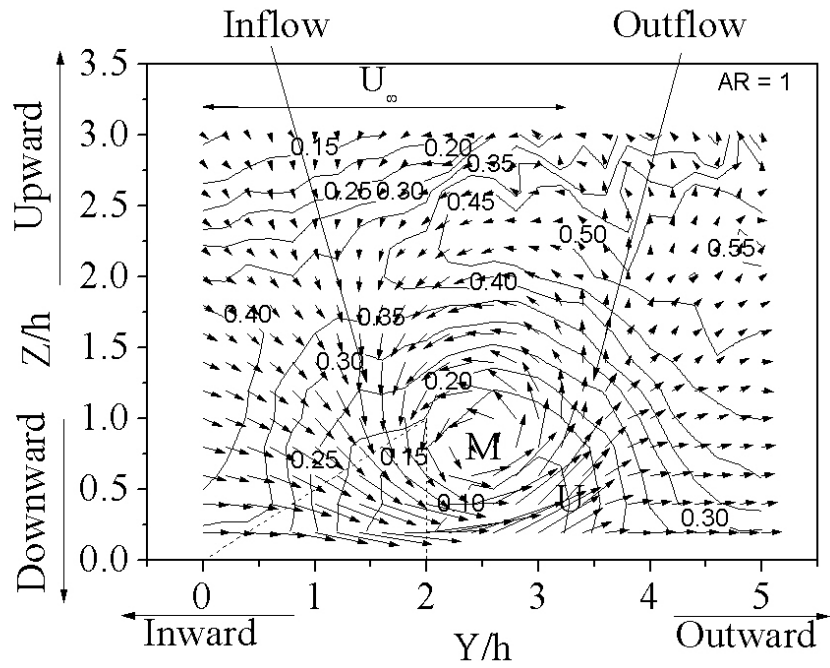


Figure 4. 12 Stream-wise turbulence intensity for Inflow and Outflow at AR = 1, 2 and 4. (a) Inflow, (b) Outflow, (c) Inflow and Outflow.

Turbulence length scales are also very important for characterizing a turbulent flow [14]. Taylor microscale represents the small and dissipative eddies in turbulent flow. Increasing (decreasing) Taylor microscale suggests decreasing (increasing) amount of fluctuating kinetic energy, in context with the upper bound of the turbulence energy cascade, which scale with the integral length. Convection of kinetic energy from (to) a neighboring high (low) turbulence region and local production or depletion can muddle this quasi-equilibrium turbulence manifestation. The contour view of Taylor microscales (normalized by h) at AR = 1, 2 and 4 are presented in Figure 4.13. The peak Taylor microscale zone can be seen at $Z/h \approx 2$. A trough value of Taylor microscale is observed at the main vortex core. This trough in Taylor microscale can be explained by the local high turbulence intensity, that is, greater turbulence intensity can sustain a higher dissipation rate and thus a smaller Taylor microscale. As shown in Figures 4.13 and 4.14, at the main vortex core the Taylor microscale increases with the decrease of turbulence intensity as the aspect ratio increases.



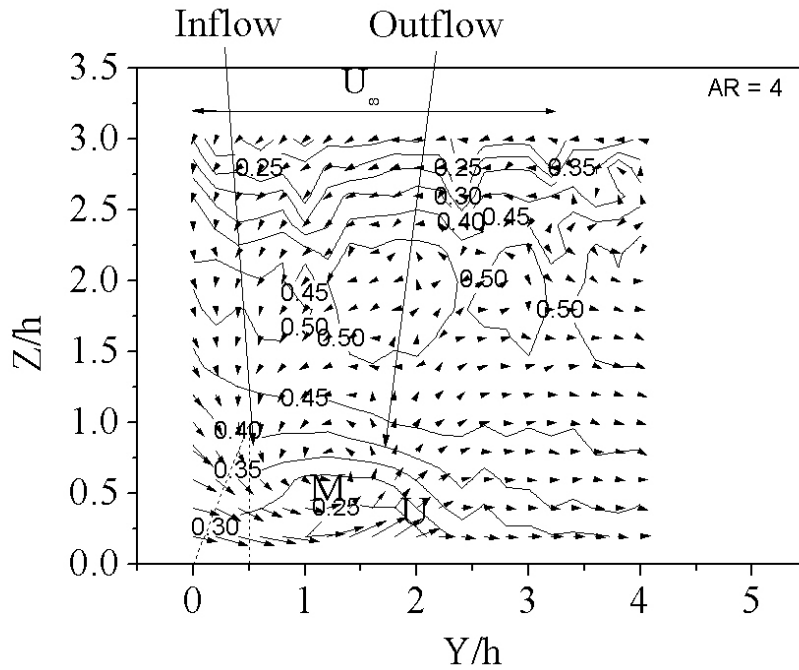


Figure 4. 13 Stream-wise Taylor microscale (normalized by h) contour and cross-stream velocity vector at AR = 1, 2 and 4.

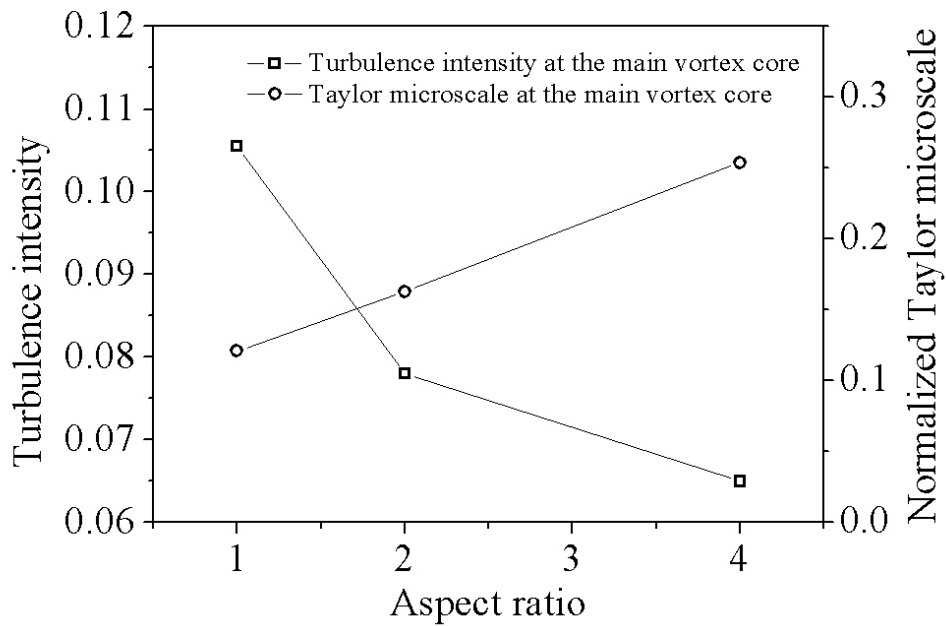
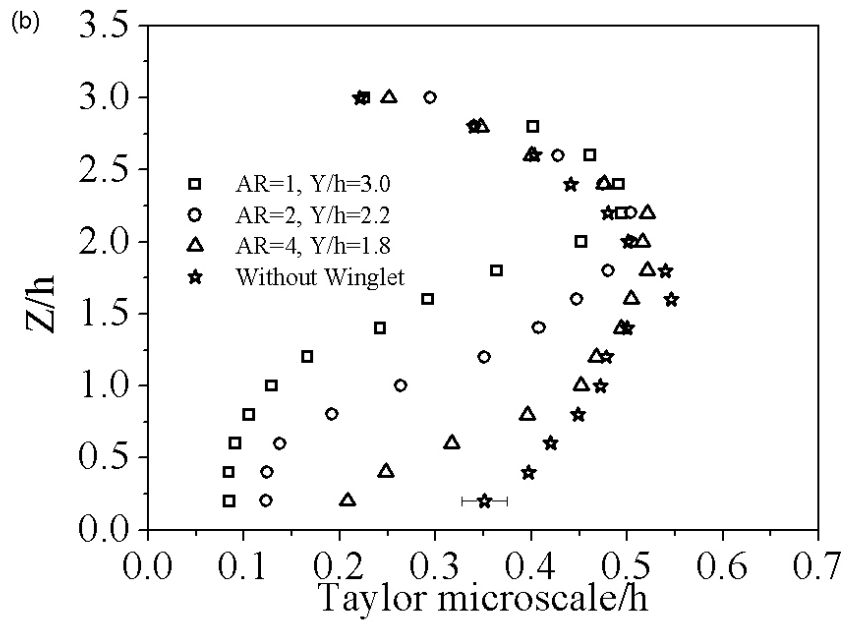
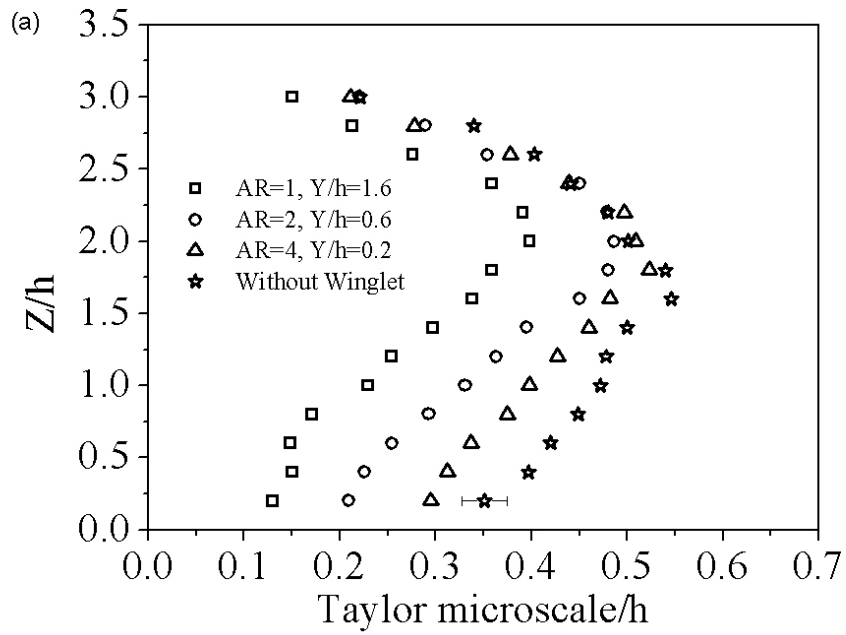


Figure 4. 14 Stream-wise turbulence intensity and Taylor microscale at the main vortex core with respect to aspect ratio.

Figure 4.15 shows the Taylor microscale normalized by the winglet height at Inflow and Outflow contrasted with the reference smooth surface case without winglet. From next to the solid surface, Taylor microscale increases with the distance away from the wall and peaked at around $Z/h = 2$, then it decreases until the free stream value. The increase trend (when $Z/h < 2$) may be attributed to the turbulence intensity distribution. Near the wall the turbulence intensity is the highest, thus the condition can sustain a higher dissipation rate, thereupon a smaller Taylor microscale. Away from the wall, the turbulence intensity decreases and, to this extent, the Taylor microscale increases. However, if the distance from the solid wall continues increasing, getting nearer to the boundary layer edge, the velocity gradient becomes less (see Figure 4.6). This would lead to a smaller shear in the boundary layer flow, and thus a smaller Taylor microscale. This explains the decrease trend when $Z/h > 2$.

With the presence of a winglet for both Inflow and Outflow (Figures 4.15a and b) the Taylor microscale is smaller than the smooth surface case when the height is lower than $Z/h = 2$, and its value increases with the increase of aspect ratio. This agrees with the negative correlation between Taylor microscale and turbulence intensity. Above $Z/h = 2$, when the Taylor scale is dominated by the decreasing shear with height, all curves gathered together and the influence of aspect ratio is less significant. Figure 4.15c shows the comparison between inflow and outflow. An overall trend of larger Taylor microscale at outflow when $Z/h > 2$ and at inflow when $Z/h < 2$ can be observed. With the increase of aspect ratio the difference between inflow and outflow in Taylor microscale becomes smaller. The relative uncertainty in Taylor microscale is estimated to be 7 %.



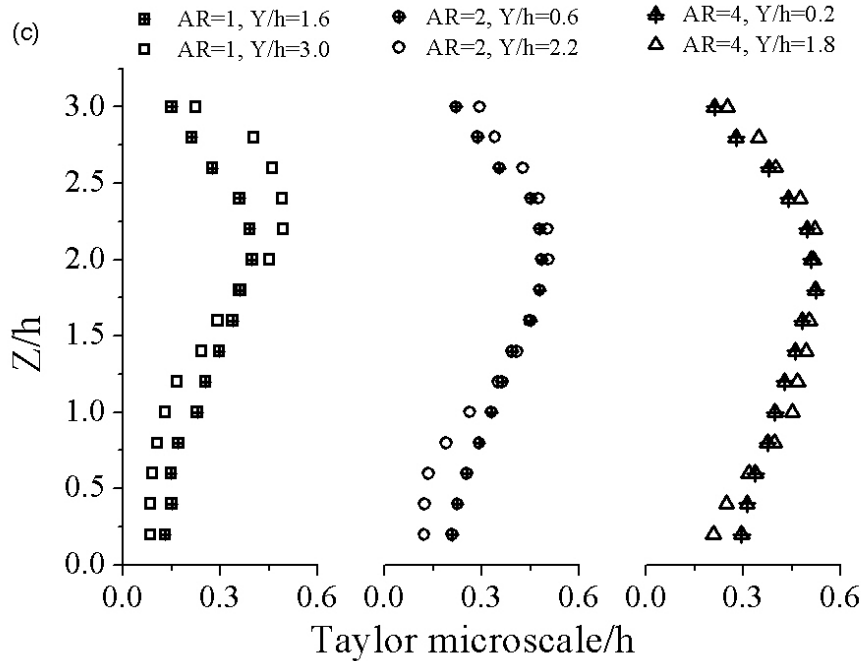
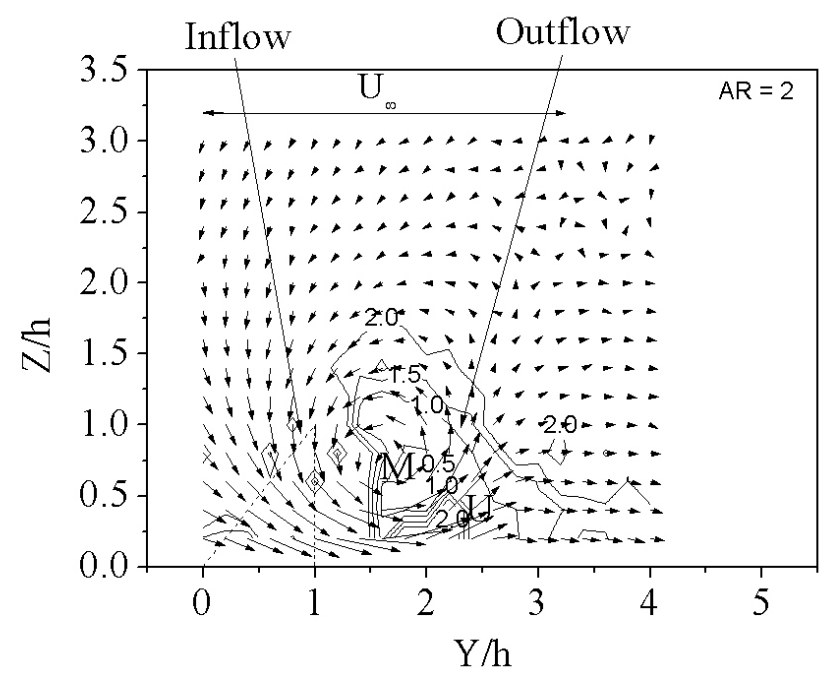
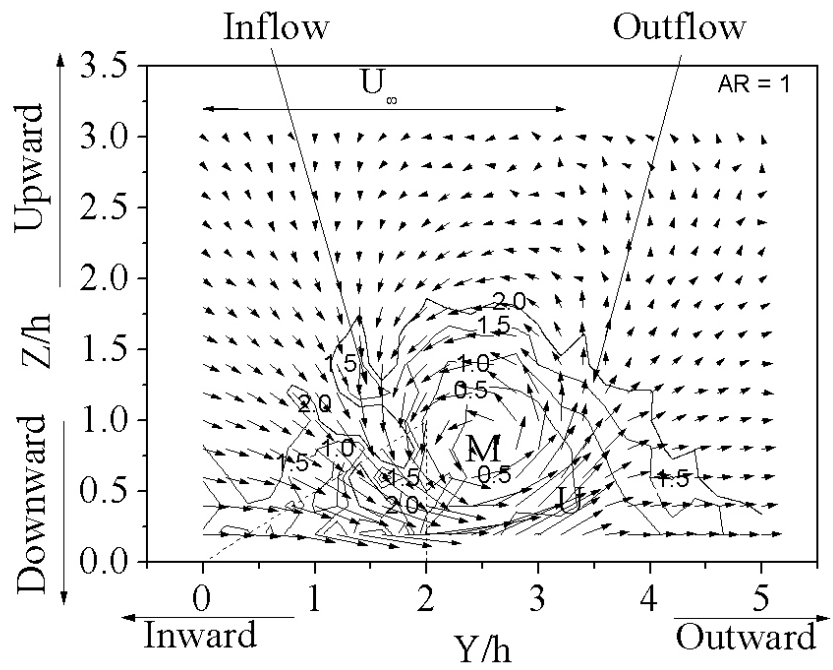


Figure 4. 15 Stream-wise Taylor microscale (normalized by h) for Inflow and Outflow at AR = 1, 2 and 4.

Integral length scale represents the large and energy containing eddies. The contour of integral length scale normalized by winglet height is shown in Figure 4.16. For all three aspect ratios, the integral length scale is approximately unity near the main vortex core, attesting that integral length scales with the dimension of the obstruction; in this case the height of the winglet. Thus the integral length scale is independent of the aspect ratio at the studied conditions, with the relatively small angle of attack $\alpha = 30^\circ$ considered. Note that this integral length scale is not related to the longitudinal vortex in Y-Z plane. The integral length scale is obtained from u velocity component, which contains the information of eddies in the plane parallel to X axis, like X-Y plane and X-Z plane.



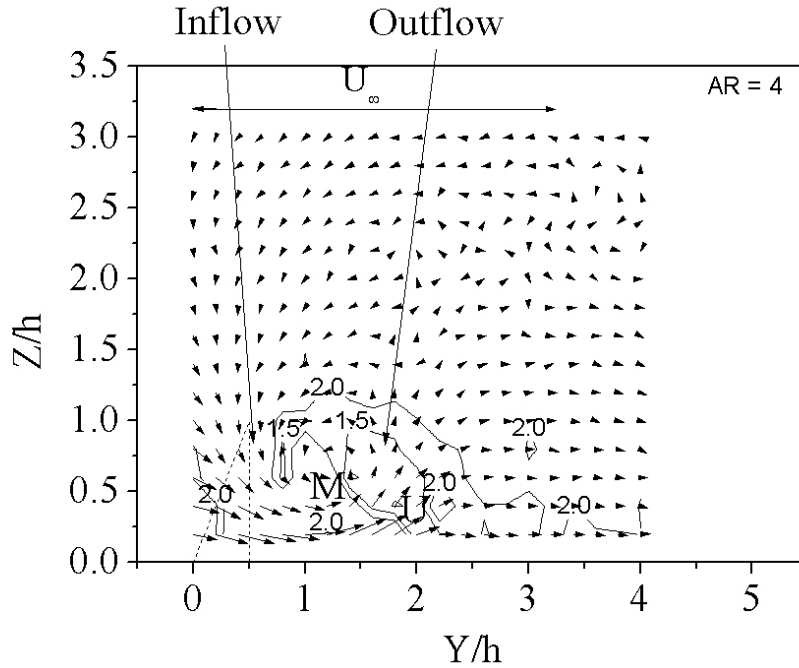


Figure 4. 16 Stream-wise integral length scale contour and cross-stream velocity vector.

4.5 Conclusion

The wake structure of a delta winglet with an aspect ratio of 1, 2 and 4 positioned at an angle of attack of 30 degrees on a flat surface were experimentally scrutinized at a Reynolds number based on the winglet height of 6000 via triple sensor hot-wire measurements. The boundary layer on the flat surface was otherwise turbulent and had a thickness of 26 mm (2.6 times the tested winglet height). Big vortex structures deeply embedded into the boundary layer were observed in the cross-stream plane. At the Inflow, the boundary layer was thinned and at the Outflow, it was thickened. This thinning and thickening effect became less significant with increasing aspect ratio. Peak streamwise velocity deficits were observed at the main vortex core and the Upwash Region. With the increase of aspect ratio, the peak velocity deficit at the main vortex core decreased while the one at the Upwash Region remained approximately unchanged. The main vortex moved downward and inward with respect to the winglet vertex, and outward with respect to the winglet rear corner. The vortex intensity and turbulence intensity decreased,

while the corresponding Taylor microscale increased. The integral length scale was found to be insensitive to the aspect ratio over the studied conditions.

Acknowledgments

This work was made possible by Natural Sciences and Engineering Research Council of Canada and Ontario Centres of Excellence.

Reference

- [1] J. Serpa, R. Lessmann, W. Hagist, Turbulent separated and reattached flow over a curved surface, *ASME J. Fluids Eng.* 109 (1987) 403–409.
- [2] W. Zhou, Y. Rao, H. Hu, An experimental investigation on the characteristics of turbulent boundary layer flows over a dimpled surface, *ASME J. Fluids Eng.* 138 (2016) 21204.
- [3] P. Panigrahi, S. Acharya, Multi-modal forcing of the turbulent separated shear flow past a rib, *ASME J. Fluids Eng.* 126 (2004) 22–31.
- [4] G. Bergeles, N. Athanassiadis, The flow past a surface-mounted obstacle, *ASME J. Fluids Eng.* 105 (1983) 461–463.
- [5] S. Acharya, S. Dutta, T. Myrum, Turbulent flow past a surface-mounted two-dimensional rib, *ASME J. Fluids Eng.* 116 (1994) 238–246.
- [6] B.R. Pearon, R. Elavarasan, R.A. Antonia, The response of a turbulent boundary layer to a square groove, *ASME J. Fluids Eng.* 119 (1997) 466–469.
- [7] Sutardi, C. Ching, Effect of different sized transverse square grooves on a turbulent boundary layer, *Exp. Fluids.* 34 (2003) 261–274.
- [8] F. Dupont, C. Gabillet, P. Bot, Experimental Study of the Flow in a Compact Heat Exchanger Channel With Embossed-Type Vortex Generators, *ASME J. Fluids Eng.* 125 (2003) 701.

- [9] H. Wu, D. S-K. Ting, S. Ray, An Experimental Study of Turbulent Flow Behind a Delta Winglet, *Exp. Therm. Fluid Sci.* 88 (2017) 46–54.
- [10] G. Taylor, The spectrum of turbulence, *Proc. R. Soc. London A.* 164 (1938) 476–490.
- [11] F.E. Jørgensen, *How to Measure Turbulence with Hot-Wire Anemometers: A Practical Guide*, Dantec Dynamics, Skovlunde, Denmark, 2002.
- [12] R.S. Figliola, D.E. Beasley, *Theory and Design for Mechanical Measurements*, 5th ed., Wiley, New York, 2011.
- [13] H. Schlichting, *Boundary-Layer Theory*, 7th ed., McGraw-Hill, New York, 1979.
- [14] D.S.-K. Ting, *Basics of Engineering Turbulence*, Academic Press, New York, 2016.

CHAPTER 5

THE EFFECT OF DELTA WINGLET ATTACK ANGLE ON THE HEAT TRANSFER PERFORMANCE OF A FLAT SURFACE

Hao Wu¹, David S-K. Ting^{1†} & Steve Ray²

¹Turbulence and Energy Laboratory, Centre for Engineering Innovation, University of Windsor,

401 Sunset Ave, Windsor, Ontario, N9B 3P4, Canada

[†]Corresponding Author, dting@uwindsor.ca

²Essex Energy Corporation, 2199 Blackacre Dr, Suite #200, Oldcastle, Ontario, N0R 1L0, Canada

H. Wu, D. S-K. Ting, S. Ray., The effect of delta winglet attack angle on the heat transfer from a flat surface, *Int. J. Heat Mass Transf.*, under review

5.1 Introduction

In typical engineering applications, liquid-to-air and two-phase-to-air heat exchangers have their heat transfer ‘bottleneck’ on the air side [1]. Extending heat transfer surface and perturbing the flow are familiar means for boosting heat transfer efficiency. To perturb the flow, either main-flow disturbing or secondary flow inducing can be applied [2]. Louvers and strip fins are examples of main-flow enhancement methods, while the secondary-flow augmentation is to intentionally generate vortices via vortex generators (VGs). The investigations on the application of VGs in plate-fin heat exchangers [3–5], fin-tube heat exchangers [6–11], louvered fin heat exchanger [12–14], circular tubes [15,16], triangular ducts [17] and rectangular channels [18–20] have revealed that VGs are effective heat transfer enhancers. Vortex generators are typically incorporated into a surface by means of punching, embossing, stamping, or attachment process, with an

attack angle [21]. As described by Fiebig [22], when the attack angle is 90 degrees, generated vortices are mainly transverse. As the attack angle decreases, the longitudinal vortices dominate over the transverse ones. Noting that it is impossible to generate pure longitudinal vortices, since transverse vortices spawn naturally unless the attack angle is zero, in which case no vortices, longitudinal or transverse, are created [21]. Transverse vortices have their rotating axes normal to the main flow direction and the flow is primarily two-dimensional, whereas the rotation direction of longitudinal vortices is parallel to the main flow direction which makes the flow three-dimensional. Some studies [22,23] found longitudinal vortices showing less flow loss and better heat transfer characteristics than transverse vortices. Extensive reviews of the longitudinal vortex generators are available from a number of sources [2,24–26]; nevertheless, a brief highlight of pertaining literature is due.

A delta winglet, as shown in Figure 5.1, is an effective vortex generator. In several comparison studies, this type of vortex generator posted itself as potentially the best longitudinal vortex generator with simple geometry. In Edwards and Alker [27], the heat transfer enhancement by cubes (typical transverse vortex generators) and delta winglets (typical longitudinal vortex generators) were compared. The winglets vortices could achieve a higher overall enhancement by persisting over a greater distance, though cubes furnished greater local enhancements. Zhou and Ye [28] studied the heat transfer improvement by rectangular winglet, trapezoidal winglet, delta winglet and curved trapezoidal winglet. The curved trapezoidal winglet gave the best performance in fully turbulent flow, while the delta winglet showed the best performance in the laminar and transitional flow. In Fiebig [22], systematical comparison of rectangular and delta wings and winglets were conducted. The results showed that winglets were better than wings in terms of heat transfer enhancement and pressure penalty. Tian et al. [21] numerically compared the heat transfer augmentation by rectangular and delta winglet pairs in a flat-plate channel. They concluded that the delta winglet pair was better than the rectangular winglet pair on overall performance.

Since the attack angle of the delta winglet essentially dictates the transverse/longitudinal vortices ratio, its effect on heat transfer performance has attracted heightened interest. Lei et al. [29] conducted CFD simulation on the hydrodynamics and heat transfer of a delta winglet in a fin-and-tube heat exchanger. Winglets with a thickness of 0.2 mm, aspect ratio from 1 to 4 and attack angle from 10 to 50 degrees were studied. The heat transfer coefficient increased with the increase of attack angle and aspect ratio. Chen et al. [30] numerically studied the heat transfer enhancement of delta winglets in a finned oval tube heat exchanger. Three attack angles (20, 30 and 45 degrees) and two aspect ratios (1.5 and 2) were investigated. The normalized Nusselt number had higher value for larger attack angle and smaller aspect ratio cases.

Most of the aforementioned studies were conducted inside fin-and-tube heat exchangers, where the heat transfer performance was highly influenced by the interaction between the winglet and the tube, rather than the winglet itself. At the more fundamental level, a winglet placed on an unconfined flat surface can unambiguously elucidate the impact of attack angle on the resulting flow and heat transfer characteristics, without the complication of confinement. A larger attack angle, from 30 to 60 degrees, may enable the differentiation of the relative contribution of transverse versus longitudinal vortices; for the longitudinal vortices are expected to diminish at larger attack angles. In short, the objective of this study is to examine the effect of winglet attack angle on the convective heat transfer from an unconfined flat surface. The heat transfer performance is interpreted in terms of the transverse-longitudinal vortex structures, streamwise velocity, velocity boundary layer thickness, and turbulence fluctuation.

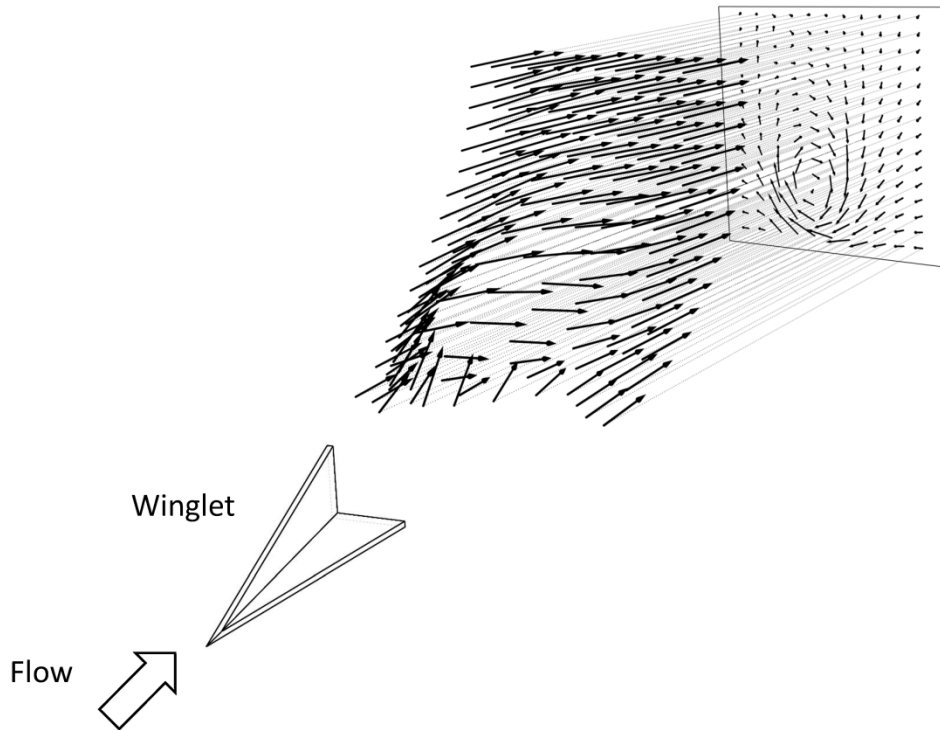


Figure 5. 1 Delta winglet vortex generator.

5.2 Experimentation

Figure 5.2 shows the experimental facilities. The experiments were conducted in a 1.8 m long wind tunnel test section with a 0.76 m by 0.76 m cross-section. A PTFE plate with a thermal conductivity of 0.25 W/(m·K) and emissivity of 0.92 was inlaid in the center of the 10 mm thick test section base. The PTFE was 3 mm thick, 295 mm wide and 380 mm long. The test section base was made of 10 mm thick fiberglass with a very low heat conductivity of 0.04 W/(m·K) to minimize the conduction heat loss. A water tank underneath the PTFE plate was heated to produce steam to evenly heat up the bottom surface of the PTFE plate at a temperature of 100 °C. An infrared thermal camera (Fluke TiX520) mounted on the top of the test section was employed to capture the temperature distribution of the top surface. The thermal photograph had 240 × 320 pixels, resulting in approximately 1 mm resolution. The temperatures on both sides of the PTFE plate were verified by type-T thermocouples with an accuracy of 0.5°C.

The delta winglet (Figure 5.2) was made from a 0.1 mm thick aluminum sheet with an emissivity of 0.09. It had a height h of 10 mm and a chord length c of 20 mm, resulting in an aspect ratio of 2. The winglet was attached 800 mm from the inlet of the test section on the PTFE plate by one of the folds. The attack angle α was set at 30, 45 and 60 degrees. The flow behind the winglet was measured by a triple sensor hotwire probe (type 55P95) and a constant-temperature anemometer at $20h$. The measured plane was $80 \text{ mm} \times 40 \text{ mm}$ with a spatial resolution of 4 mm. The velocity boundary layer for the smooth surface without the winglet was identified to be turbulent, with a shape factor of 1.3 and thickness of $2.4h$. The background turbulence intensity was approximately 0.4%. The free stream velocity was set at 10 m/s, resulting in a Reynolds number based on the winglet height of around 6000. The velocity signals were sampled at 80 kHz and low passed at 30 kHz. All three velocity components, U , V , W , were measured simultaneously, with a sampling number of 10^6 .

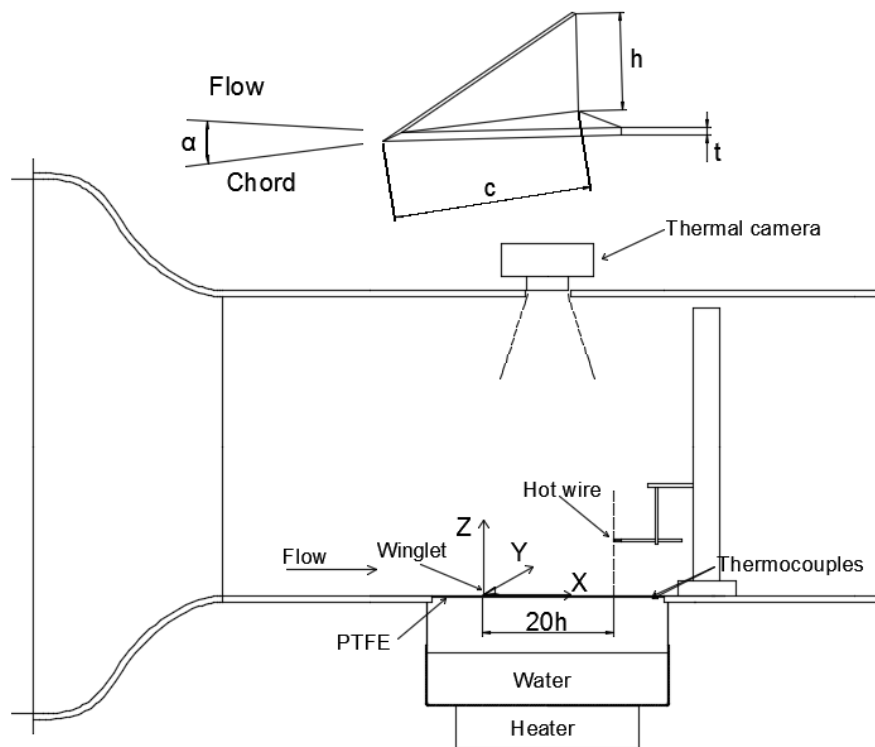


Figure 5. 2 A schematic of the winglet and the experimental setup inside the wind tunnel. $t = 0.1 \text{ mm}$; $\alpha = 30^\circ, 45^\circ, 60^\circ$; $h = 10 \text{ mm}$; $c = 20 \text{ mm}$.

5.3 Data Processes

The portion of heat conducted through the PTFE plate can be deduced from:

$$q = \frac{k_{\text{PTFE}}A(T_{\text{bottom}}-T_{\text{top}})}{t_{\text{PTFE}}} \quad (5.1)$$

where k_{PTFE} is the thermal conductivity of PTFE, A is the heat transfer area, t_{PTFE} is the thickness of the PTFE plate, T_{bottom} and T_{top} are the temperature at the bottom (100°C) and top of the PTFE plate, respectively. Assuming all the heat conducted to the upper surface is convected away by the flow stream, the convective heat transfer coefficient is thus,

$$h = \frac{q}{A(T_{\text{top}}-T_{\text{air}})} \quad (5.2)$$

where T_{air} is the air temperature. The corresponding non-dimensional Nusselt number is

$$\text{Nu} = \frac{hD}{k_{\text{air}}} \quad (5.3)$$

where D is the characteristic length, k_{air} is the thermal conductivity of air. To disclose the enhancement, this Nusselt number is cast with respect to the reference Nusselt number for the smooth surface case without the wingleet, i.e.,

$$\text{Nu}/\text{Nu}_0 = \frac{T_{\text{bottom}}-T_{\text{top}}}{T_{\text{top}}-T_{\text{air}}} / \frac{T_{\text{bottom}}-T_{\text{top},0}}{T_{\text{top},0}-T_{\text{air}}} \quad (5.4)$$

Concerning the flow characteristics, the hot wire measures the instantaneous velocities U , V , and W . The time-averaged velocities \bar{U} (\bar{V} , \bar{W}) is obtained from:

$$\bar{U} = \frac{1}{N} \sum_{i=1}^N U_i \quad (5.5)$$

where N is the sample size. The magnitude of the cross-stream velocity vector is

$$L = \sqrt{(\bar{V}^2 + \bar{W}^2)} \quad (5.6)$$

and the angle of the cross-stream velocity vector,

$$\theta = \arctan\left(\frac{\overline{W}}{\overline{V}}\right) \quad (5.7)$$

The dimensionless vorticity can be calculated from:

$$\Omega = \frac{h}{U_\infty} \left(\frac{\partial \overline{W}}{\partial y} - \frac{\partial \overline{V}}{\partial z} \right) \quad (5.8)$$

The root mean square fluctuating velocity u_{rms} (v_{rms} , w_{rms}) is computed from:

$$u_{\text{rms}} = \sqrt{\frac{\sum_{i=1}^N (U_i - \overline{U})^2}{N-1}} \quad (5.9)$$

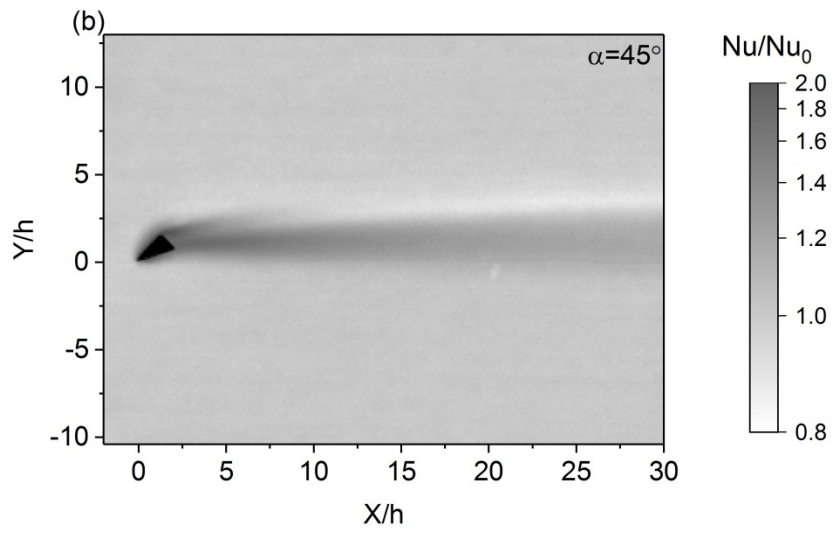
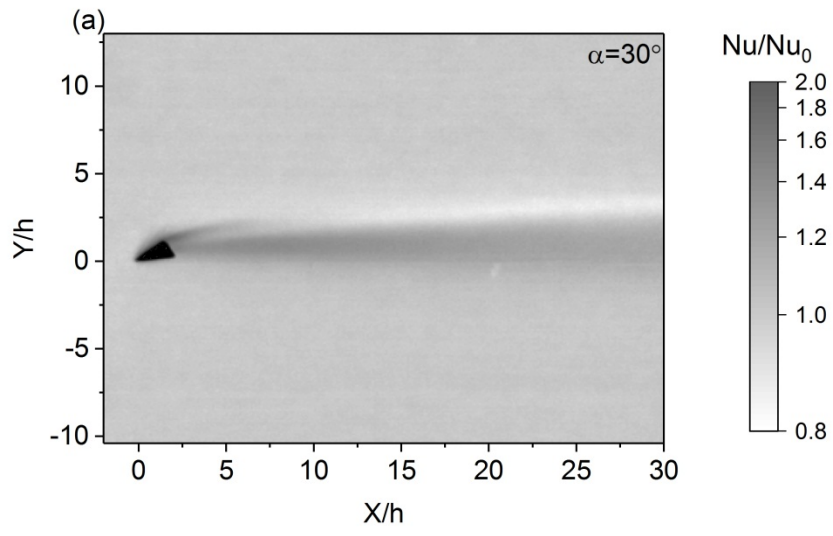
And the total turbulence fluctuation is obtained from [31]:

$$q^2 = u_{\text{rms}}^2 + v_{\text{rms}}^2 + w_{\text{rms}}^2 \quad (5.10)$$

Both time-averaged velocity and turbulence intensity are expressed in the normalized form, that is, by dividing the respective values by the free stream velocity.

5.4 Results

The effect of winglet attack angle on the heat transfer performance of the studied flat surface is portrayed in terms of the normalized Nusselt number in Figure 5.3. As mentioned in Section 2, the winglet had a much lower emissivity than that of the PTFE plate. Thus, when deducing Nu/Nu_0 based on the thermal imaging with a set emissivity of 0.92, the winglet area gave meaningless values. For this reason, the attached fold of the winglet is overlaid with a black triangle in Figure 5.3. At the proximity of the winglet, the thermal energy was effectively conducted to the winglet, a heat fin (sink), and dissipated into the cooler convective stream. For reference purpose, the origin of the X-Y-Z coordinate is set at the leading vertex of the winglet. The heat transfer augmentation ($Nu/Nu_0 > 1$) spanning the entire downstream domain is clearly visible. Also observed is a narrower stripe of heat transfer reduction ($Nu/Nu_0 < 1$), especially after 10h downstream. The heat amplification wake with a narrow diminishment section expands with downstream distance. The transversal spread of the enhanced region with distance was also reported by Torii and Yanagihara [32], who attributed it to longitudinal vortices.



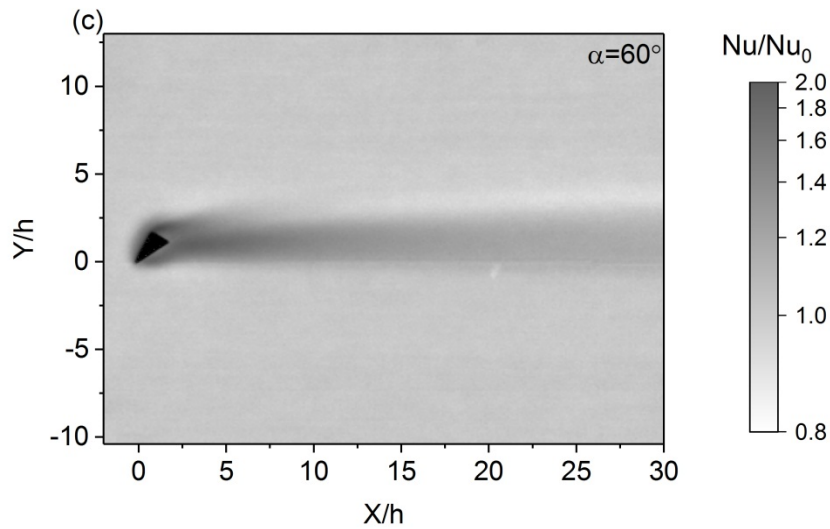


Figure 5. 3 Variation of normalized Nusselt number profile with attack angle. (a) 30 degrees, (b) 45 degrees, (c) 60 degrees.

The peak heat transfer enhancement (maximum Nu/Nu_0) and peak heat transfer decline (minimum Nu/Nu_0) with respect to downstream distance are tracked in Figure 5.4. In the near wake ($X/h < 10$), the peak Nu/Nu_0 increased with the attack angle, most significantly when increasing α from 30 to 45 degrees. This is believed to be due to considerable transition from dominantly longitudinal to largely transverse vortices. For α of 45 to 60 degrees, the maximum normalized Nusselt number dropped nearly exponentially with downstream distance. This initial sharp drop in the peak Nu/Nu_0 with X is presumably due to the rapid fading of the transverse vortex. Farther downstream ($X/h > 10$), the peak Nu/Nu_0 decreased more gradually and became essentially insensitive to the attack angle. This extended heat transfer enhancement which persevered beyond the final measurement location of $30h$ is hypothesized to be the work of the slower decaying longitudinal vortices. These heat transfer augmentations caused by the slowly-decaying longitudinal whirling motions also appeared to be fairly insensitive to changes in the attack angle, over the range of studied α .

Figure 5.4 also shows that the attack angle had only marginal effect on the maximum reduction in the heat transfer rate. It is, nonetheless, discernable that the attack angle which led to the most effective heat transfer enhancement (largest peak Nu/Nu_0), $\alpha = 60$ degrees, also resulted in the least heat transfer diminishment. Similarly, α of 30 degrees which produced the smallest peak Nu/Nu_0 , also collaborated with the most serious heat transfer attenuation. In short, the larger the attack angle, the better the heat transfer performance, at both near and far wake.

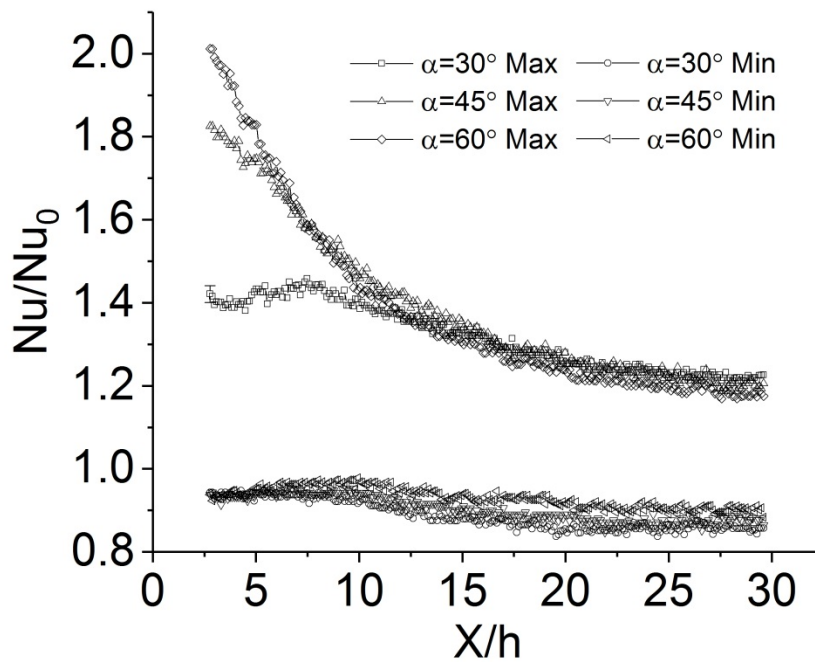
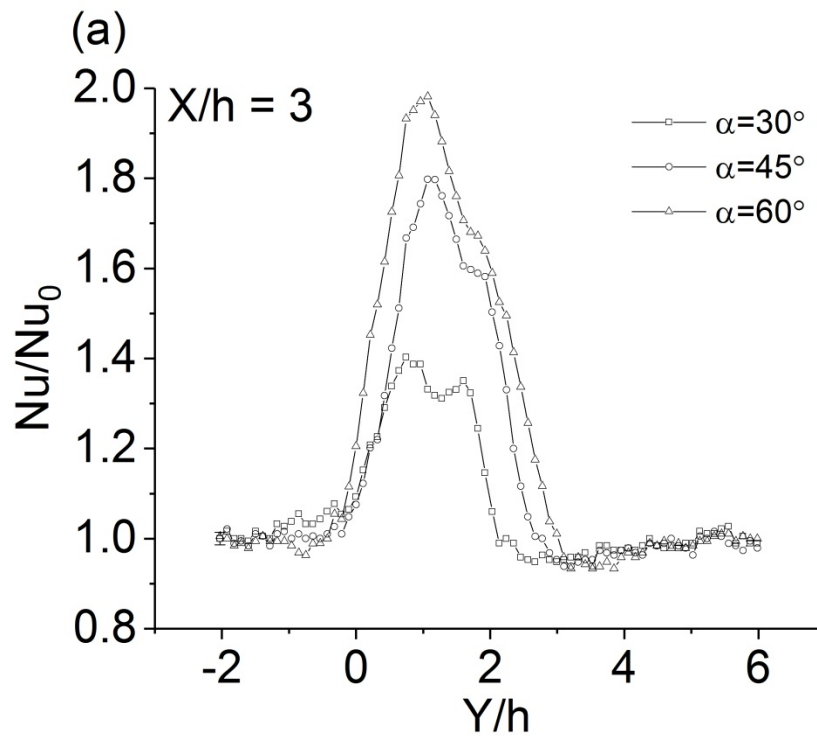


Figure 5. 4 Maximum and minimum local normalized Nusselt number for attack angles of 30, 45 and 60 degrees with respect to downstream distance.

To examine closely the heat transfer performance downstream of the winglet, the cross stream Nu/Nu_0 profiles at 3h and 20h are plotted in Figure 5.5. The uncertainty of Nu/Nu_0 is estimated to be around 0.02. Shortly behind the winglet at $X=3h$ (Figure 5.5a), the heat transfer is drastically enhanced. The heat transfer augmentation peaks around $Y/h = 1$, with the largest boost at the largest attack angle, where Nu approached twice the corresponding Nu_0 value. The markedly enhanced heat transfer stretch also broadens with the attack angle. Two distinguishable peaks can be observed, especially for $\alpha = 30$ degrees. The two peaks are probably brought about by the coexistence of fast-

decaying transverse and long-lasting longitudinal vortices. In contrast, only a single peak of lower heat transfer enhancement is seen farther downstream at $X=20h$ (Figure 5.5b), presumably because only the longer-lasting longitudinal vortices remained. Besides the maximum heat transfer augmentation at around $Y/h = 1$, a heat transfer dip at around $Y/h = 3$ can also be observed at $X = 20h$.



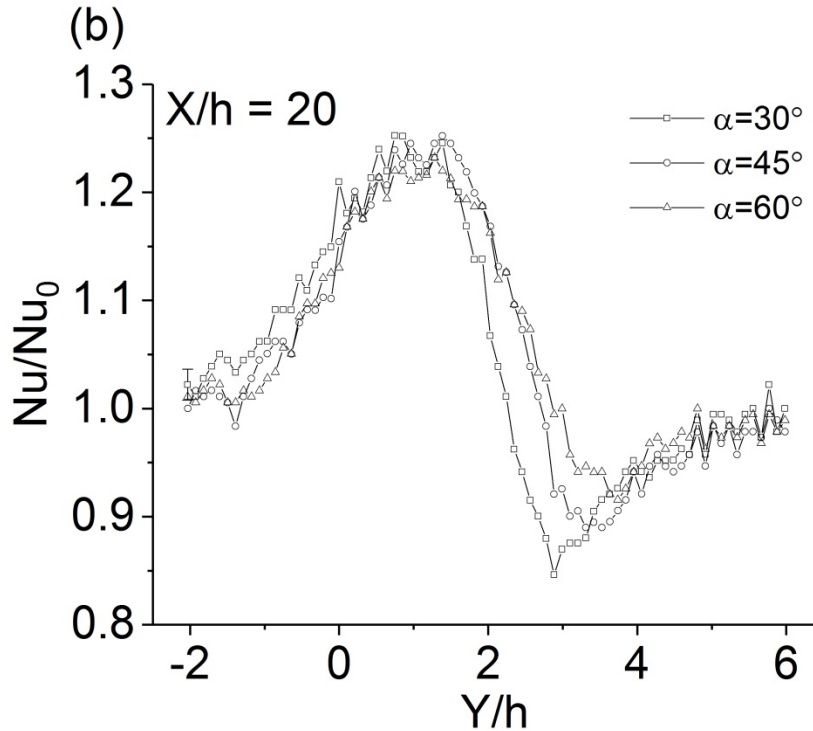
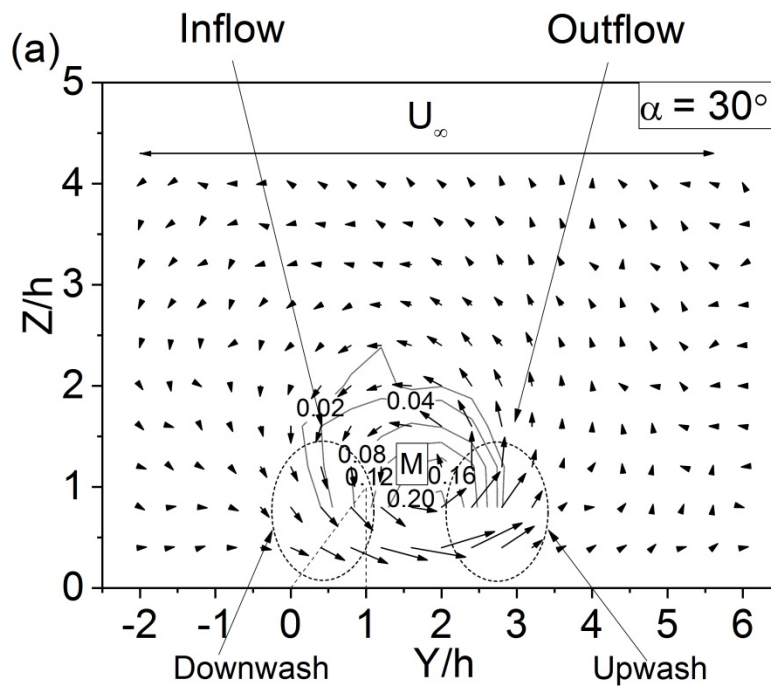


Figure 5.5 The normalized Nusselt number for attack angles of 30, 45 and 60 degrees at downstream distance of (a) 3h, (b) 20h.

To better understand the drastic and inhomogeneous heat transfer enhancement caused by the prevailing vortices, the flow details at $X = 20h$ are further scrutinized. Figures 5.6 to 5.8 depict contours of \bar{U}/U_∞ , q^2/U_∞^2 , and Ω at $X=20h$. The uncertainty for probe positioning is estimated to be $0.2h$ and the uncertainties in \bar{U}/U_∞ , q^2/U_∞^2 and Ω are approximately 0.03, 0.0007 and 0.004, respectively. A large longitudinal vortex structure, the Main vortex (marked as M), is recognizable in Figure 5.6. This Main vortex played a key role in the convective heat transfer characteristics. It brought cooler air toward the hot surface at the Inflow (Downwash) region ($Y/h \approx 1$). This, along with the reduction in the velocity boundary layer (the near wall region where the convection fluid, and thus heat, was constricted) by the Inflow, Figure 5.7, led to the maximum heat transfer augmentation. After receiving thermal energy from the hot plate, the heated air was scooped away via the Outflow (Upwash). The Outflow area, characterized by significant out-of-plate flow, corresponded well with the minimum Nu/Nu_0 region, where the heat transfer rate (Nu) is less than the corresponding flat plate without the winglet case (Nu_0).

The outgoing flow gathered the heated air and also increased the thermal boundary layer. The reduced temperature gradient along with the increased insulating layer (thermal resistance) contributed to the Nu/Nu_0 valley. Furthermore, a deficit in streamwise velocity at the Upwash region can also be detected. This added to the decline in the convective heat transfer rate. The combined warmer air, thickened boundary layer and reduced streamwise velocity outweighed any heat transfer enhancement by the higher turbulence fluctuation (Figure 5.8) in the Outflow region.



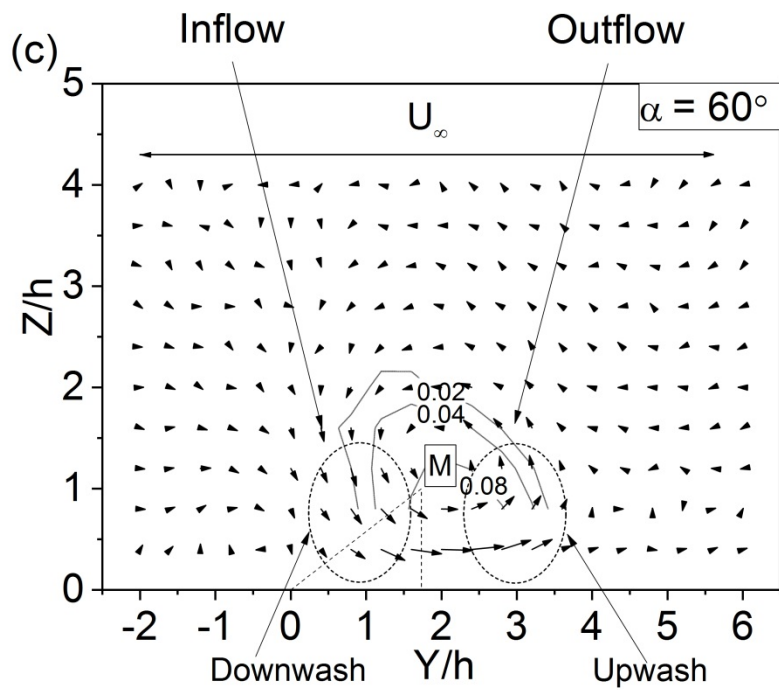
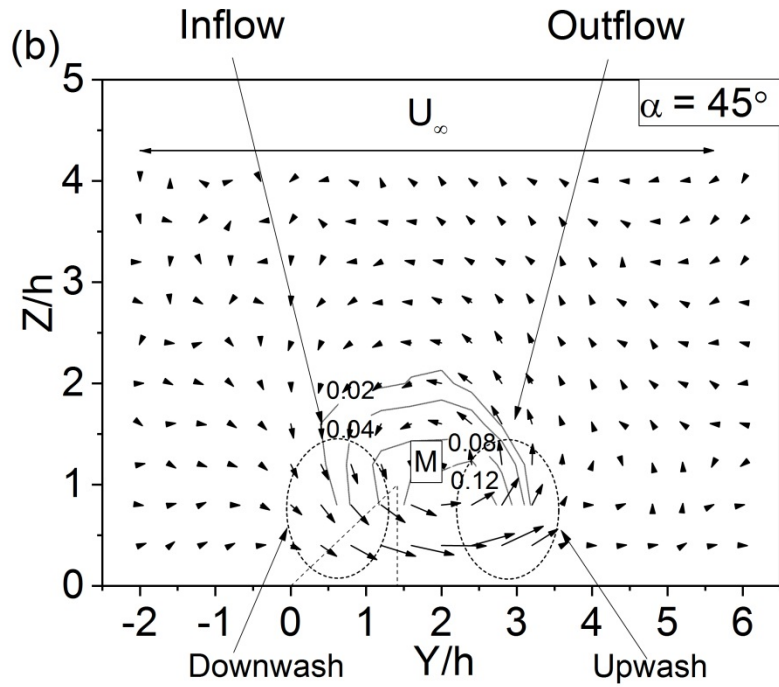
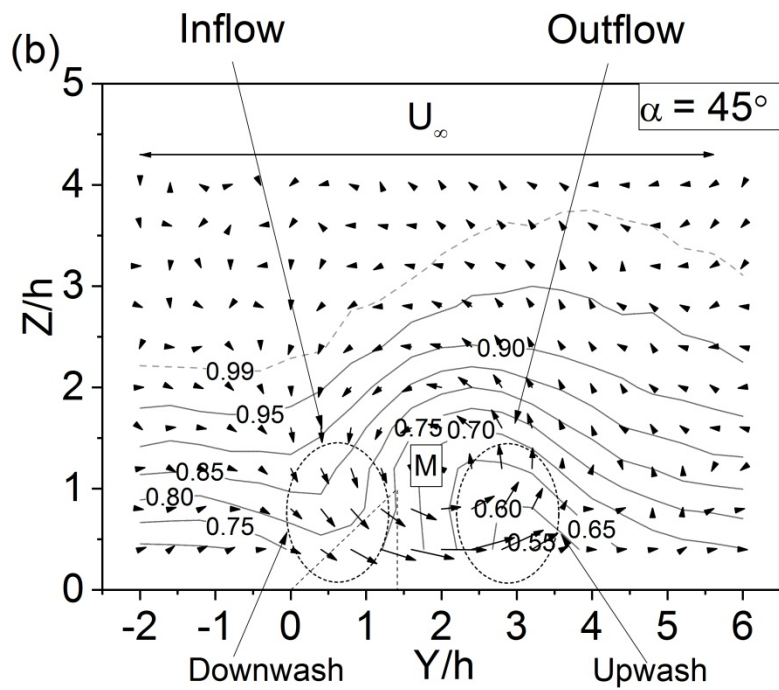
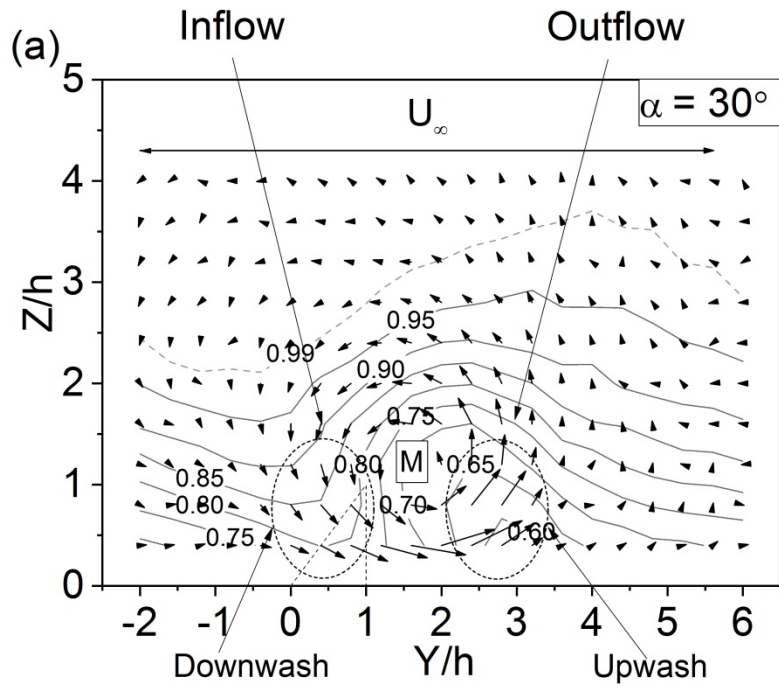


Figure 5. 6 Dimensionless vorticity contour and cross-stream velocity vector for attack angles of (a) 30, (b) 45, (c) 60 degrees.



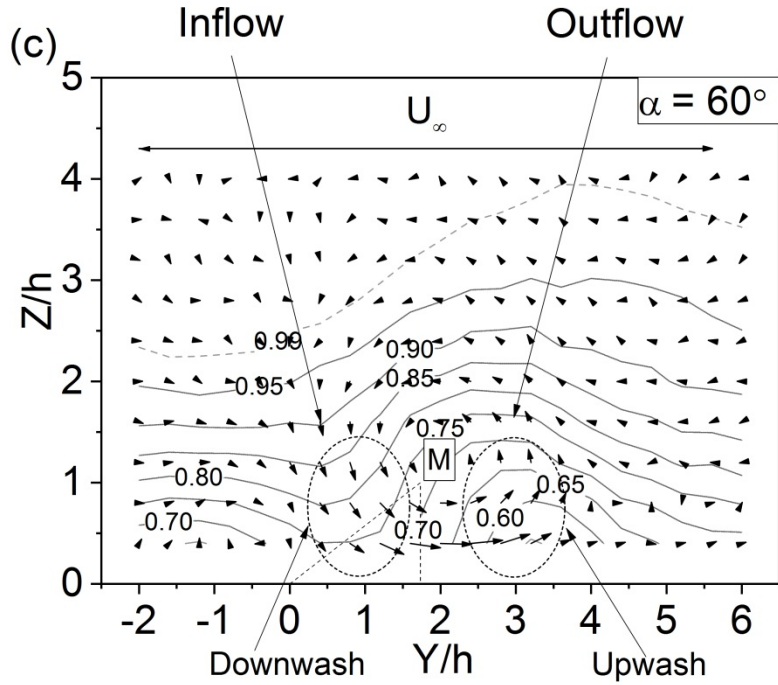
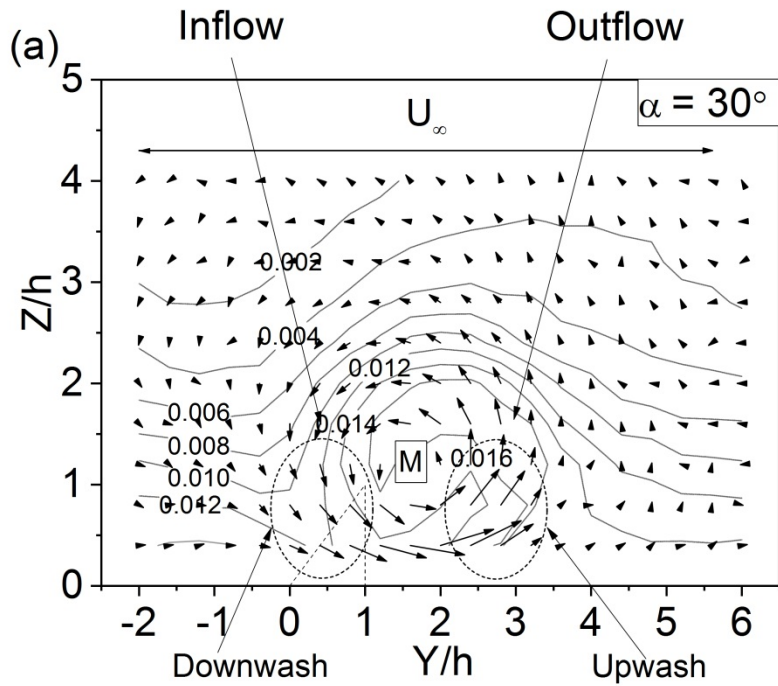


Figure 5.7 Normalized streamwise time-averaged velocity contours and cross-stream velocity vectors for attack angles of (a) 30, (b) 45, (c) 60 degrees.



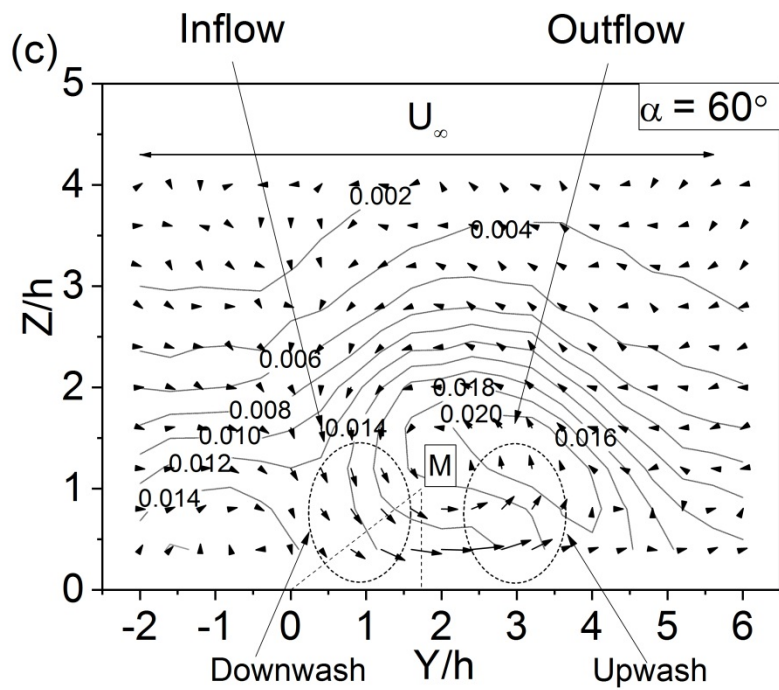
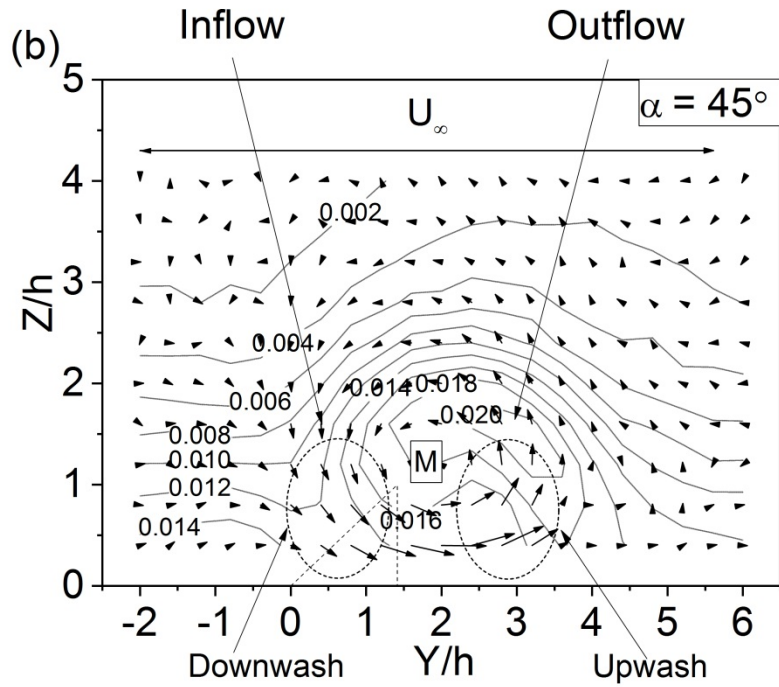


Figure 5. 8 Normalized total turbulence fluctuation (q^2/U_∞^2) contour and cross-stream velocity vector for attack angles of (a) 30, (b) 45, (c) 60 degrees.

The insensitivity of the maximum Nu/Nu_0 and the increase of minimum Nu/Nu_0 with respect to the attack angle at $X=20h$ (Figure 5.5b) are resulting from the integrated effects of multiple underlying mechanisms. These workings are hereby disclosed. 1) Figure 5.6 delineates a reduction in the cross-stream velocity magnitude and also the vorticity with increasing attack angle. These diminishments weakened both Downwash and Upwash, resulting in smaller heat transfer amplification in the Inflow (Downwash) region and lesser heat transfer attenuation in the Outflow (Upwash) area. 2) Figure 5.7 depicts that the thinning of boundary layer at Inflow weakened with increasing attack angle, while the boundary layer thickening at Outflow increased. As such, the boundary layer thinning induced heat transfer amplification around Inflow lessened with attack angle, while the heat transfer decline in the vicinity of Outflow grew larger due to boundary layer thickening. 3) The peak velocity deficit at the Upwash region worsened with the increase of attack angle, leading to larger heat transfer attenuation. 4) The escalation of turbulence fluctuation with increasing attack angle shown in Figure 5.8 suggests intensification of heat transfer rate.

The aforementioned mechanisms need to be decoupled to elucidate the independent individual impact. Due to severe coupling of the involved players, controlled experiments of varying only one parameter at a time while keeping the others fixed were not practicable. Thus, multiple regression analysis was employed. This method fits the independent and dependent variables into an equation following the least squares estimation. Based on the preceding explanations, the out-of-plate velocity \overline{W}/U_∞ , the velocity boundary layer thickness $(\delta - \delta_0)/\delta_0$, the local near-surface streamwise velocity (at the lowest measurement point, $Y = 0.4h$) $U_{0.4}/U_\infty$, and the averaged total turbulence fluctuation inside the velocity boundary layer $\overline{q^2}/U_\infty^2$ were singled out. The in-to-plate (out-of-plate) velocity set the Inflow (Outflow). The normalized total turbulence fluctuation was the average of all measurement points inside the velocity boundary layer, for it imposed the convective transport of heat within the heat transfer bottleneck, i.e., the boundary layer. The cross-stream vorticity was eliminated after preliminary results showing that it could not differentiate between Inflow and Outflow,

i.e., it gave ambiguous outcomes. To prevent unnecessary and unjustified complexity, the influence of each of these fluid parameters on Nu/Nu_0 was assumed to be linear.

Table 5. 1 Boundary conditions for regression.

Boundary conditions	Nu/Nu_0	\overline{W}/U_∞	$(\delta - \delta_0)/\delta_0$	$U_{0.4}/U_\infty$	$\overline{q^2}/U_\infty^2$
Smooth surface	1	0	0	0.65	0.0093
No wind	0.35	0	0	0	0

Figure 5.9 presents the multiple regression results. The measured data are shown in symbols and the lines represent the fitted curves. The curves are not smooth because they are calculated from flow measurement data with a spatial interval of 4 mm. The adjusted R-square for this regression is 98%, the standard error is 3.5%, and the P-values for all the factors are much smaller than 0.05. It is thus clear that the results are sound. Note that two boundary conditions were considered; see Table 1. The reference is the smooth surface case without the winglet, furnishing Nu/Nu_0 of one. The limiting condition occurs when there is no wind. For this condition all four considered factors would be zero, leaving Nu/Nu_0 equal to 0.35. The multiple regression result is:

$$Nu/Nu_0 = 0.35 - 3.84 \frac{\overline{W}}{U_\infty} - 0.06 \left(\frac{\delta - \delta_0}{\delta_0} \right) + 0.63 \frac{U_{0.4}}{U_\infty} + 27.35 \frac{\overline{q^2}}{U_\infty^2} \quad (5.11)$$

The coefficients β (values in front of each parameter) are then standardized by [33]

$$\beta_j^s = \beta_j \frac{\sigma_j}{\sigma_y} \quad (5.12)$$

where β_j^s is the standardized coefficient for the j^{th} factor, σ_j and σ_y are the standard deviations of the j^{th} factor and the dependent variable (Nu/Nu_0). The calculated standardized coefficient for \overline{W}/U_∞ , $(\delta - \delta_0)/\delta_0$, $U_{0.4}/U_\infty$, and $\overline{q^2}/U_\infty^2$ are -0.46, -0.14, 0.36, and 0.48, respectively. The absolute value of the standard coefficient indicates the weight of each factor. It is clear that the turbulence intensity has the largest impact on

the heat transfer rate, followed by the out-of-plate velocity. The near-surface velocity has moderate influence, while the effect of boundary layer thickness is relatively small.

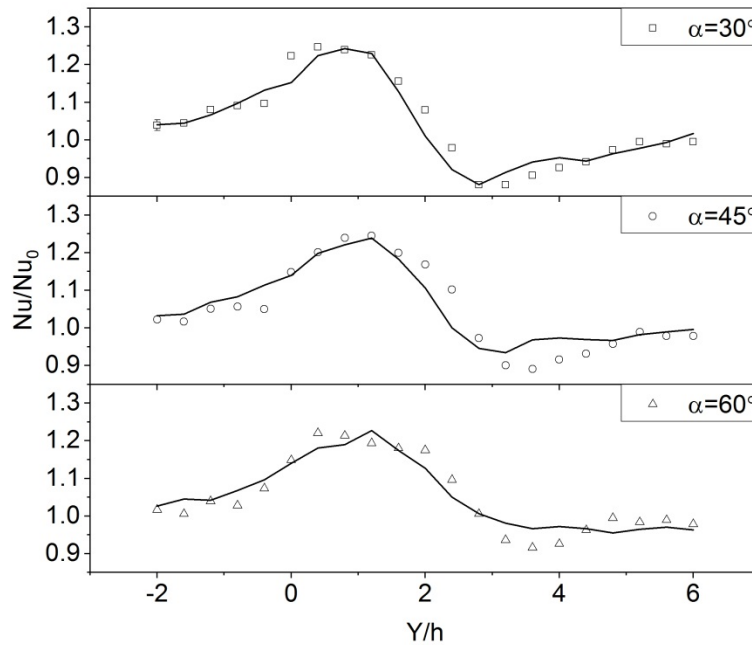
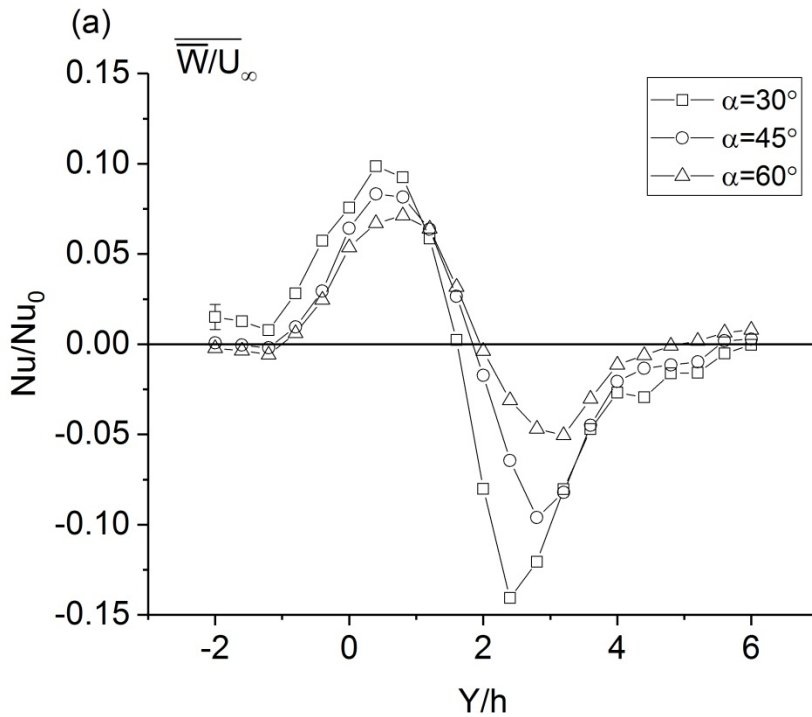
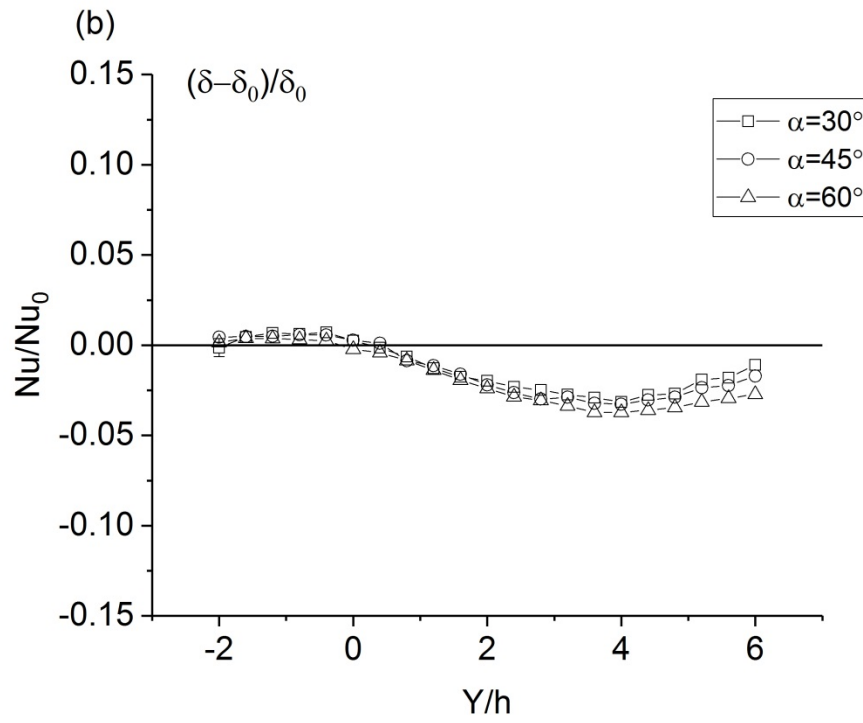


Figure 5.9 The multiple regression results. Lines signify fitted curves, and symbols are measured data.

Figure 5.10 illustrates the impact of individual fluid parameters on the heat transfer performance. As expected, the out-of-plate velocity (Figure 5.10a), which represents the downwash and upwash motions of primarily the longitudinal vortices, significantly contributes to the heat transfer enhancement at Inflow and even more so its diminishment at Outflow. With increasing attack angle, both heat transfer enhancement by Downwash and diminishment by Upwash lessened. However, the decrease in heat transfer diminishment is much more significant than that in heat transfer enhancement, making the increase of attack angle beneficial overall. An increase in the boundary layer thickness only slightly attenuated the heat transfer rate (Figure 5.10b), which agrees with its small standardized coefficient. This heat transfer attenuation increases marginally with the attack angle. The near-surface velocity shows a similar impact on the heat transfer rate as the out-of-plate velocity, i.e., augmentation at Inflow and reduction at Outflow

(Figure 5.10c). Similar to the out-of-plate velocity influence, the heat transfer enhancement by near-surface velocity decreased at larger attack angle. On the other hand, unlike the out-of-plate velocity effect, the Outflow heat transfer diminishment associated with the near-surface velocity increased with increasing attack angle. Thus increasing attack angle lessened the overall heat transfer performance caused by the near-surface velocity. The turbulence fluctuation has a forceful positive effect on the heat transfer performance near the center of the vortex, from $Y/h = 0$ to 4 (Figure 5.10d). With the increase of attack angle, the augmentation caused by turbulence escalated as well as widened. The insensitivity of the maximum Nu/Nu_0 and the increase of minimum Nu/Nu_0 with respect to the attack angle can hereby be explained: At Inflow, the negative impact with increasing attack angle related to the out-of-plate and near-surface velocities is roughly canceled out by the positive influence with increasing attack angle identified with turbulence fluctuation. On the other hand, at Outflow, the beneficial effect with attack angle affiliated with the out-of-plate velocity and the turbulence fluctuation outweighs the negative impact with attack angle associated with the near-surface velocity.





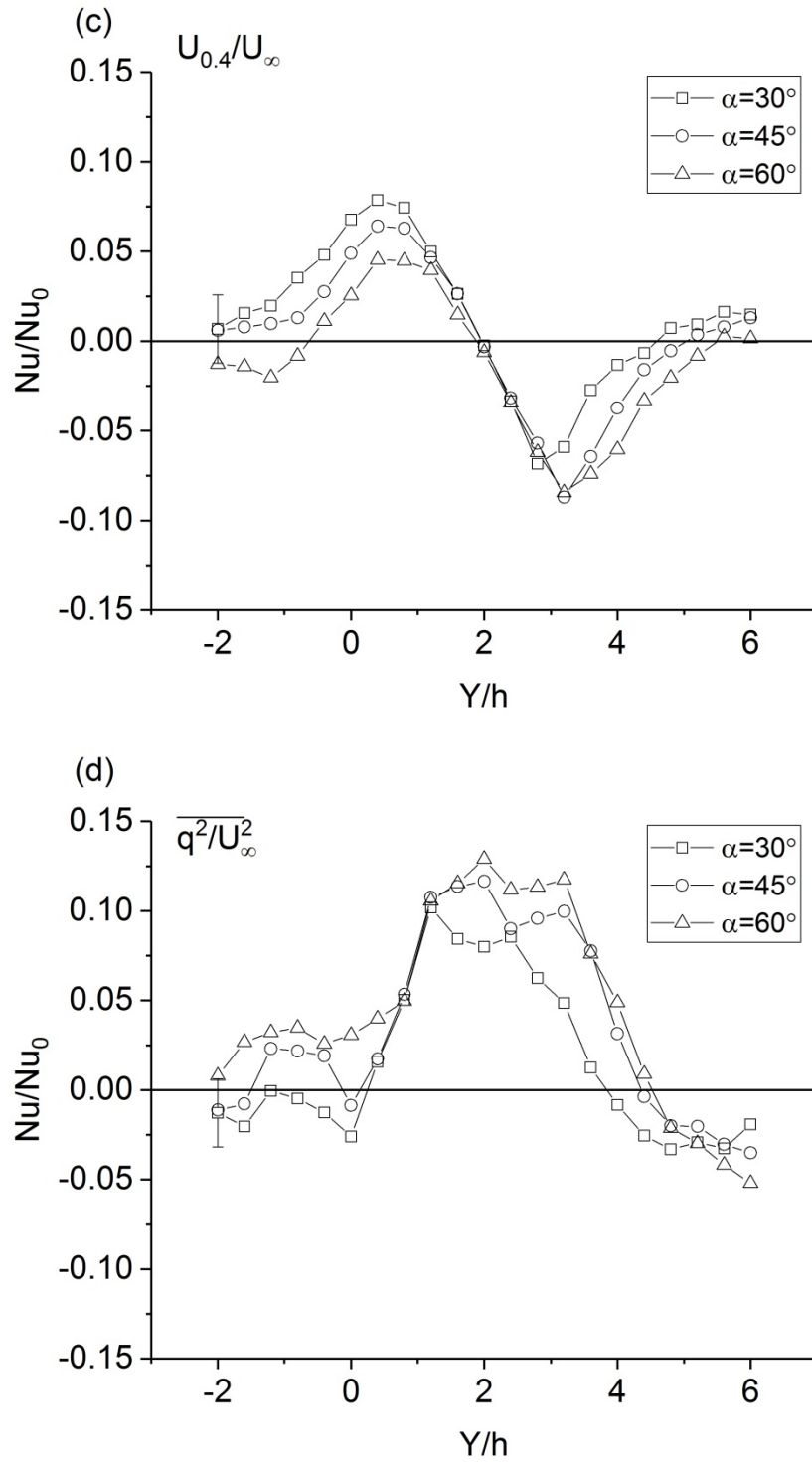


Figure 5.10 The impact of individual fluid parameters on the heat transfer rate. (a) \overline{W}/U_∞ , (b) $(\delta - \delta_0)/\delta_0$, (c) $U_{0.4}/U_\infty$, (d) $\overline{q^2}/U_\infty^2$.

5.5 Conclusion

The effect of winglet attack angle on the heat transfer performance of a flat plate with a 100 °C bottom surface was assessed with the help of a thermal camera. The attack angle of the 10 mm high (h) and 20 mm long winglet was varied from 30 to 60 degrees at a Reynolds number based on h of 6000. A heat transfer enhancement section and a narrower diminishment stripe which prevailed far downstream of the winglet were observed. The maximum heat transfer enhancement, which heightened with attack angle, dropped sharply in the near wake. It remained significant, but largely insensitive to attack angle, with a gradual decay farther downstream. The typical far stream convection heat transfer features, at 20h, were scrutinized and related to the detailed flow characteristics deduced with the help of a triple hot wire. The bulk flow was dominated by a string of longitudinal vortices. It induced Inflow corresponded to serious heat transfer augmentation, while the resulting Outflow correlated with noticeable heat transfer decline. Multiple regression analysis was invoked to isolate the impact of individual flow parameters on the heat transfer rate. The out-of-plate velocity contributed to the heat transfer enhancement at Inflow as well as the diminishment at Outflow. With the increase of attack angle, the heat transfer augmentation at Inflow decreased while the heat transfer rate at Outflow was reduced further. Thickening of the boundary layer slightly attenuated the heat transfer rate. This heat transfer attenuation increased marginally with the attack angle. The near-surface velocity correlated strongly with the heat transfer augmentation at Inflow and its reduction at Outflow. With increasing attack angle, the heat transfer enhancement (at Inflow) by increasing near-surface velocity weakened while the diminishment at Outflow increased. The turbulence fluctuation substantially enhanced the heat transfer rate near the center of the vortex. With the increase of attack angle, the augmentation caused by turbulence escalated. The coupled interworking of these impacts resulted in the insensitivity of the maximum Nu/Nu_0 and the increase of minimum Nu/Nu_0 with respect to the attack angle.

Acknowledgments

This work was made possible by Natural Sciences and Engineering Research Council of Canada and Ontario Centres of Excellence.

Reference

- [1] B. Kundu, P.K. Das, Performance and optimum dimensions of flat fins for tube-and-fin heat exchangers: A generalized analysis, *Int. J. Heat Fluid Flow*. 30 (2009) 658–668. doi:10.1016/j.ijheatfluidflow.2009.03.016.
- [2] A.M. Jacobi, R.K. Shah, Heat transfer surface enhancement through the use of longitudinal vortices : a review of recent progress, *Exp. Therm. Fluid Sci.* 11 (1995) 295–309.
- [3] P. Saha, G. Biswas, S. Sarkar, Comparison of winglet-type vortex generators periodically deployed in a plate-fin heat exchanger - a synergy based analysis, *Int. J. Heat Mass Transf.* 74 (2014) 292–305. doi:10.1016/j.ijheatmasstransfer.2014.03.015.
- [4] A. Sinha, K. Ashoke Raman, H. Chattopadhyay, G. Biswas, Effects of different orientations of winglet arrays on the performance of plate-fin heat exchangers, *Int. J. Heat Mass Transf.* 57 (2013) 202–214. doi:10.1016/j.ijheatmasstransfer.2012.10.034.
- [5] K. Song, S. Liu, L. Wang, Interaction of counter rotating longitudinal vortices and the effect on fluid flow and heat transfer, *Int. J. Heat Mass Transf.* 93 (2016) 349–360. doi:10.1016/j.ijheatmasstransfer.2015.10.001.
- [6] A. Sinha, H. Chattopadhyay, A.K. Iyengar, G. Biswas, Enhancement of heat transfer in a fin-tube heat exchanger using rectangular winglet type vortex generators, *Int. J. Heat Mass Transf.* 101 (2016) 667–681. doi:10.1016/j.ijheatmasstransfer.2016.05.032.

- [7] Y.L. He, H. Han, W.Q. Tao, Y.W. Zhang, Numerical study of heat-transfer enhancement by punched winglet-type vortex generator arrays in fin-and-tube heat exchangers, *Int. J. Heat Mass Transf.* 55 (2012) 5449–5458. doi:10.1016/j.ijheatmasstransfer.2012.04.059.
- [8] X. Wu, W. Zhang, Q. Gou, Z. Luo, Y. Lu, Numerical simulation of heat transfer and fluid flow characteristics of composite fin, *Int. J. Heat Mass Transf.* 75 (2014) 414–424. doi:10.1016/j.ijheatmasstransfer.2014.03.087.
- [9] J. Li, S. Wang, J. Chen, Y.G. Lei, Numerical study on a slit fin-and-tube heat exchanger with longitudinal vortex generators, *Int. J. Heat Mass Transf.* 54 (2011) 1743–1751. doi:10.1016/j.ijheatmasstransfer.2011.01.017.
- [10] A. Kumar, J.B. Joshi, A.K. Nayak, A comparison of thermal-hydraulic performance of various fin patterns using 3D CFD simulations, *Int. J. Heat Mass Transf.* 109 (2017) 336–356. doi:10.1016/j.ijheatmasstransfer.2017.01.102.
- [11] M.J. Li, W.J. Zhou, J.F. Zhang, J.F. Fan, Y.L. He, W.Q. Tao, Heat transfer and pressure performance of a plain fin with radiantly arranged winglets around each tube in fin-and-tube heat transfer surface, *Int. J. Heat Mass Transf.* 70 (2014) 734–744. doi:10.1016/j.ijheatmasstransfer.2013.11.024.
- [12] H. Huisseune, C. T'Joel, P. De Jaeger, B. Ameel, S. De Schampheleire, M. De Paepe, Influence of the louver and delta winglet geometry on the thermal hydraulic performance of a compound heat exchanger, *Int. J. Heat Mass Transf.* 57 (2013) 58–72. doi:10.1016/j.ijheatmasstransfer.2012.10.016.
- [13] H. Huisseune, C. T'Joel, P. De Jaeger, B. Ameel, S. De Schampheleire, M. De Paepe, Performance enhancement of a louvered fin heat exchanger by using delta winglet vortex generators, *Int. J. Heat Mass Transf.* 56 (2013) 475–487. doi:10.1016/j.ijheatmasstransfer.2012.09.004.
- [14] B. Ameel, J. Degroote, H. Huisseune, J. Vierendeels, M. De Paepe, Interaction effects between parameters in a vortex generator and louvered fin compact heat

- exchanger, *Int. J. Heat Mass Transf.* 77 (2014) 247–256.
doi:10.1016/j.ijheatmasstransfer.2014.04.073.
- [15] Y. Lei, F. Zheng, C. Song, Y. Lyu, Improving the thermal hydraulic performance of a circular tube by using punched delta-winglet vortex generators, *Int. J. Heat Mass Transf.* 111 (2017) 299–311. doi:10.1016/j.ijheatmasstransfer.2017.03.101.
- [16] Y. Xu, M.D. Islam, N. Kharoua, Numerical study of winglets vortex generator effects on thermal performance in a circular pipe, *Int. J. Therm. Sci.* 112 (2017) 304–317. doi:10.1016/j.ijthermalsci.2016.10.015.
- [17] H.E. Ahmed, M.Z. Yusoff, M.N.A. Hawlader, M.I. Ahmed, B.H. Salman, A.S. Kerbeet, Turbulent heat transfer and nanofluid flow in a triangular duct with vortex generators, *Int. J. Heat Mass Transf.* 105 (2017) 495–504.
doi:10.1016/j.ijheatmasstransfer.2016.10.009.
- [18] A. Khanjian, C. Habchi, S. Russeil, D. Bougeard, T. Lemenand, Effect of rectangular winglet pair roll angle on the heat transfer enhancement in laminar channel flow, *Int. J. Therm. Sci.* 114 (2017) 1–14.
doi:10.1016/j.ijthermalsci.2016.12.010.
- [19] C. Min, C. Qi, E. Wang, L. Tian, Y. Qin, Numerical investigation of turbulent flow and heat transfer in a channel with novel longitudinal vortex generators, *Int. J. Heat Mass Transf.* 55 (2012) 7268–7277.
doi:10.1016/j.ijheatmasstransfer.2012.07.055.
- [20] Y. Wang, Y.L. He, W.W. Yang, Z.D. Cheng, Numerical analysis of flow resistance and heat transfer in a channel with delta winglets under laminar pulsating flow, *Int. J. Heat Mass Transf.* 82 (2015) 51–65.
doi:10.1016/j.ijheatmasstransfer.2014.11.016.
- [21] L.T. Tian, Y.L. He, Y.G. Lei, W.Q. Tao, Numerical study of fluid flow and heat transfer in a flat-plate channel with longitudinal vortex generators by applying field synergy principle analysis, *Int. Commun. Heat Mass Transf.* 36 (2009) 111–120. doi:10.1016/j.icheatmasstransfer.2008.10.018.

- [22] M. Fiebig, Embedded Vortices in Internal Flow: heat transfer and pressure loss enhancement, *Int. J. Heat Fluid Flow*. 16 (1995) 376–388. doi:10.1016/0142-727X(95)00043-P.
- [23] M. Henze, J. von Wolfersdorf, B. Weigand, C.F. Dietz, S.O. Neumann, Flow and heat transfer characteristics behind vortex generators - a benchmark dataset, *Int. J. Heat Fluid Flow*. 32 (2011) 318–328. doi:10.1016/j.ijheatfluidflow.2010.07.005.
- [24] M. Sheikholeslami, M. Gorji-Bandpy, D.D. Ganji, Review of heat transfer enhancement methods: focus on passive methods using swirl flow devices, *Renew. Sustain. Energy Rev.* 49 (2015) 444–469.
- [25] A. Joardar, A.M. Jacobi, Impact of leading edge delta-wing vortex generators on the thermal performance of a flat tube, louvered-fin compact heat exchanger, *Int. J. Heat Mass Transf.* 48 (2005) 1480–1493. doi:10.1016/j.ijheatmasstransfer.2004.10.018.
- [26] A. Kumar, J.B. Joshi, A.K. Nayak, P.K. Vijayan, A review on the thermal hydraulic characteristics of the air-cooled heat exchangers in forced convection, *Indian Acad. Sci.* 40 (2015) 673–755. doi:10.1007/s12046-015-0362-x.
- [27] F. Edwards, C. Alker, N. Crompton, The improvement of forced convection surface heat transfer using surface protrusions in the form of (a) cubes and (b) vortex generators, in: *Proc. 5th Int. Heat Transf. Conf.*, 1974: pp. 244–248.
- [28] G. Zhou, Q. Ye, Experimental investigations of thermal and flow characteristics of curved trapezoidal winglet type vortex generators, *Appl. Therm. Eng.* 37 (2012) 241–248. doi:10.1016/j.applthermaleng.2011.11.024.
- [29] Y.G. Lei, Y.L. He, L.T. Tian, P. Chu, W.Q. Tao, Hydrodynamics and heat transfer characteristics of a novel heat exchanger with delta-winglet vortex generators, *Chem. Eng. Sci.* 65 (2010) 1551–1562. doi:10.1016/j.ces.2009.10.017.
- [30] Y. Chen, M. Fiebig, N. Mitra, Conjugate heat transfer of a finned oval tube with a punched longitudinal vortex generator in form of a delta winglet—parametric

investigations of the winglet, *Int. J. Heat Mass Transf.* 41 (1998) 3961–3978.
doi:10.1016/S0017-9310(98)00076-3.

- [31] D.S.-K. Ting, *Basics of engineering turbulence*, Academic Press, New York, 2016.
- [32] K. Torii, J.I. Yanagihara, The effects of longitudinal vortices on heat transfer of laminar boundary layers, *JSME Int. J. Ser. II.* 32 (1989) 395–402.
- [33] J. Myers, A. Well, R. Lorch, *Research design and statistical analysis*, Routledge, 2010.

CHAPTER 6

CONCLUSIONS

7.1 Summary and Conclusions

Delta winglet is a potential heat transfer enhancer for engineering applications such as the cooling of solar panels. The possible cooling effect by turbulence generators and the subsequent cell efficiency and energy output enhancement were estimated in Chapter 2. The total power output enhancement was projected to be larger than the energy conversion efficiency enhancement due to the synchronous solar irradiance and cell efficiency. The predicted decrease of energy output with the climate change calls for the improvement in solar efficiency.

In chapter 3, the wake structure of a base case delta winglet, i.e., aspect ratio of 2 and attack angle of 30 degrees, was experimentally investigated by hot-wire measurement. The longitudinal main vortex was observed downstream of the winglet. The flow was divided into two regions, Inflow and Outflow. The Inflow region had a higher streamwise velocity near the plate surface than the smooth surface case, while the Outflow region had a peak velocity deficit near the surface. High turbulence intensity was maintained inside the boundary layer. The scooping effect of the main vortex was expected to bring cold air toward the hot surface and cool the Inflow region. At the Outflow region the heated air and upwash effect should increase the thermal boundary layer thickness; together with the velocity deficit, the Outflow flow region was predicted to have a heat transfer decline.

The effect of the aspect ratio on flow structure was studied in Chapter 4. The winglet was positioned at an attack angle of 30 degrees, with aspect ratios of 1, 2 and 4. With the increase of the aspect ratio, the streamwise velocity deficit at the main vortex core lessened, while that at the upwash region remained unaltered. Moreover, the vortex moved downward and inward and its intensity decreased. The turbulence level decreased with a corresponding increase in Taylor microscale. The integral length was found to be independent of the aspect ratio. The impact of the aspect ratio on heat transfer was studied in Appendix A, with condensing stream heated plate and thermal camera. As

expected, there was a stripe of heat transfer enhancement behind the delta winglet at the Inflow region and a narrower stripe of heat transfer diminishment at the Outflow region. As the aspect ratio increased from 1 to 4, the heat transfer enhancement decreased, the influence area lessened and the heat transfer diminishment increased. By correlating this heat transfer behavior with the flow parameters, the lessened heat transfer enhancement with the aspect ratio was attributed to the decrease of in-to-plate velocity, turbulence intensity, and near-surface velocity. The increase of heat transfer diminishment with the aspect ratio was correlated with the drop of turbulence intensity, which outweighed any benefit brought by lessened out-of-plate velocity.

Chapter 5 studied the influence of the attack angle on both heat transfer and flow structure. The winglet had an aspect ratio of 2, with an attack angle which varied from 30 to 60 degrees in 15-degree increments. With the increase of the attack angle, the peak heat transfer enhancement increased. This augmentation was attributed to the larger share of the transverse vortex at a larger attack angle. For an attack angle of 45 and 60 degrees, the peak Nu dropped sharply in the near wake due to the rapid fading of the transverse vortex. At farther downstream, only the slowly-decaying longitudinal vortex persisted. The heat transfer enhancement became insensitive with the increasing attack angle, while the heat transfer diminishment decreased. The flow measurements indicated that the vortex strength decreased with the attack angle while the turbulence intensity increased. The multiple regression results showed that the insensitivity of the maximum Nu with the attack angle was the result of the negative impact with increasing attack angle related to the out-of-plate and near-surface velocities balanced by the positive influence with increasing attack angle identified with turbulence fluctuation. The decreasing heat transfer diminishment can be attributed to the beneficial effect with the attack angle affiliated with the out-of-plate velocity and the turbulence fluctuation outweighed the negative impact with the attack angle associated with the near-surface velocity.

7.2 Recommendations

Based on the current study, it is clear that the delta winglet can promote the heat transfer. The heat transfer enhancement can be improved by two ways. The first is decreasing the aspect ratio, which enlarges the longitudinal vortices and therefore augments the heat

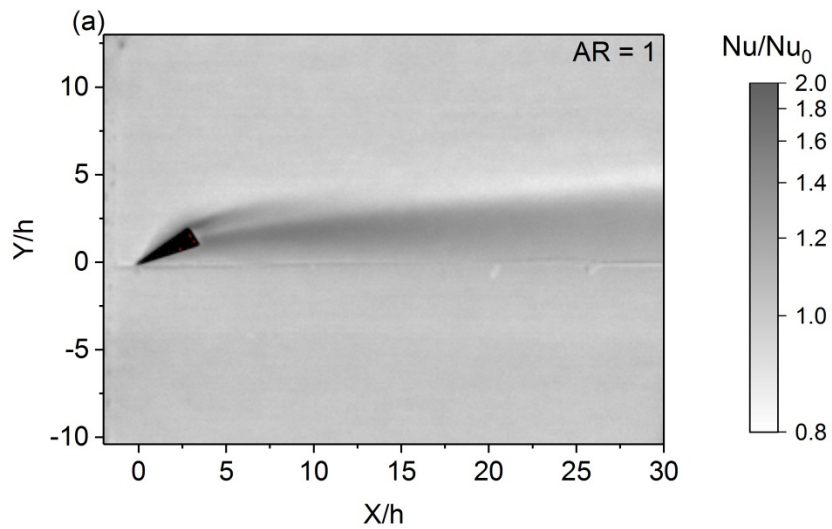
transfer for a long distance. The second is increasing the attack angle, which enlarges the share of transverse vortices and thus the augmentation is at near downstream. In the meantime, both of these ways can decrease the heat transfer diminishment. Decreasing the aspect ratio can reduce the heat transfer diminishment at near downstream while increasing the attack angle can reduce it for a long distance. More experiments need to be done to study the improvement limit for these two measures. Additionally, the combination of these two measures needs to be investigated to find the optimization.

Other parameters of the winglets need to be scrutinized, such as the size and stiffness. In the current studies, the winglet height was smaller or similar to the boundary layer thickness. A winglet with a much larger height than the boundary layer thickness may influence the heat transfer in a different way. A flexible winglet may vibrate in the wind and extract the energy from the free stream, thus the combined longitudinal vortices and vibrating vortices may couple and enhance the heat transfer. A pair of winglets or a row of winglets must be studied before putting the winglet into practical application. The spacing of the winglets could be the parameter for optimizing.

APPENDICES

Appendix A. The Effect of Aspect Ratio on Heat Transfer.

The effect of the aspect ratio on heat transfer was studied by the same setup as described in Chapter 5. Figure A.1 shows the normalized Nusselt number for aspect ratios of 1, 2 and 4. It is clear that with the increase of the aspect ratio, both the heat transfer enhancement and influenced area lessened. Moreover, the heat transfer decline stripe shows up earlier for a larger aspect ratio.



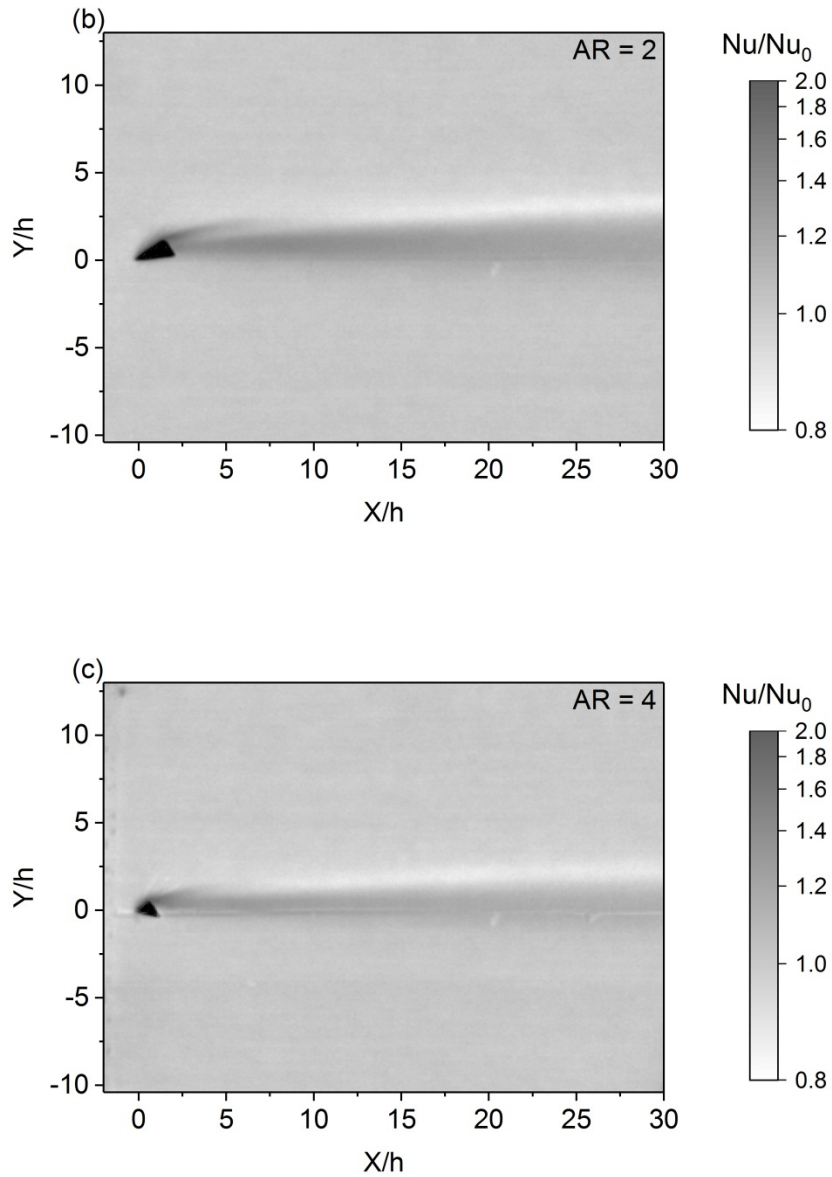


Figure A. 1 Variation of normalized Nusselt number profile with aspect ratio. (a) $AR = 1$, (b) $AR = 2$, (c) $AR = 4$.

Figure A.2 tracks the maximum and minimum Nusselt number with respect to the downstream distance. The peak heat transfer enhancement (maximum Nu/Nu_0) decreases with the aspect ratio at all the studied distance. However, with a larger aspect ratio, the heat transfer enhancement decays slower, thus the difference between the larger and smaller aspect ratio becomes less significant with the downstream distance. For the

minimum Nu/Nu_0 , it decreases with the downstream distance. Smaller aspect ratios decrease more gradually, but they all stabilized at around 0.85 after some distance.

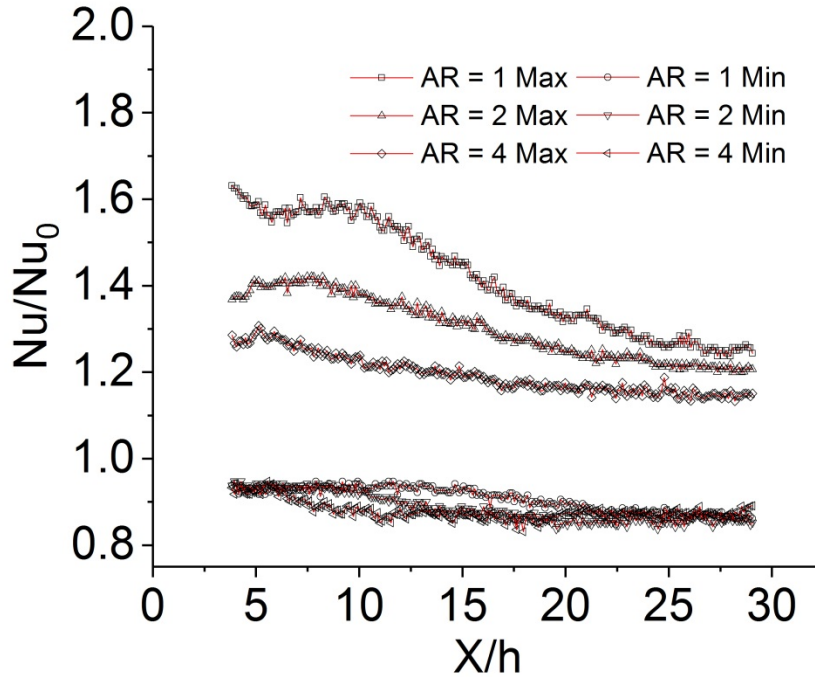


Figure A. 2 Maximum and minimum local normalized Nusselt number for aspect ratios of 1, 2 and 4 with respect to downstream distance.

Figure A.3 shows the cross stream Nu/Nu_0 profile at 10h downstream for aspect ratios of 1, 2 and 4. With the increase of the aspect ratio, the maximum Nu/Nu_0 lessened, as well as the minimum Nu/Nu_0 . The influenced area decreased and shifted towards negative Y direction.

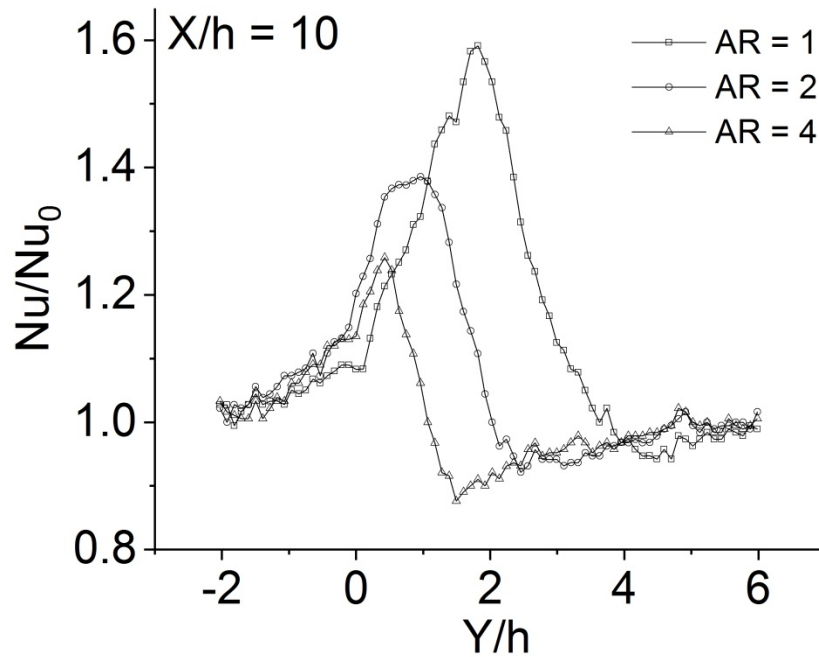


Figure A. 3 The normalized Nusselt number for aspect ratios of 1, 2 and 4 at downstream distance of 10h.

To relate this heat transfer behavior to the flow structure reported in Chapter 4, the flow measurement data was put into the equation obtained from multiple regression analysis in Chapter 5. Figure A.4 compares the calculated curves and measured data. The prediction roughly agrees with the measurement with a standard error of 5.9%, thus the multiple regression analysis results are validated.

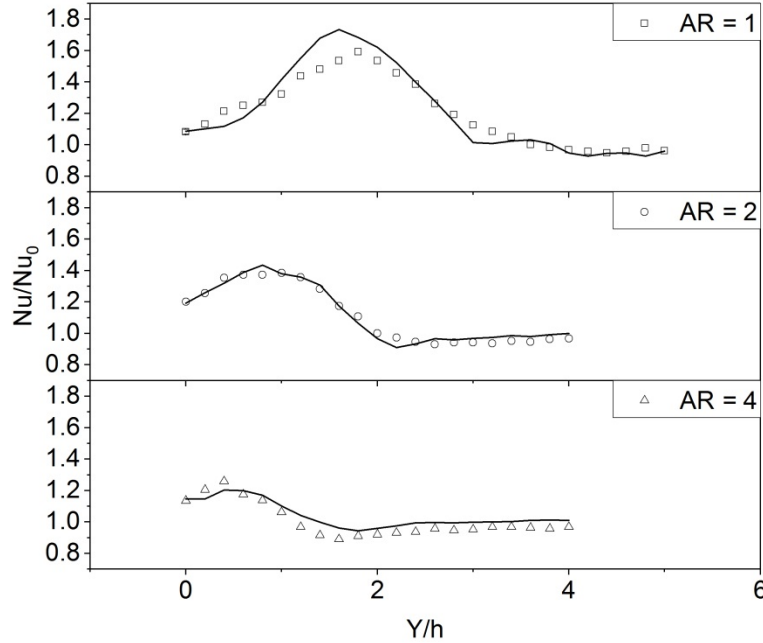
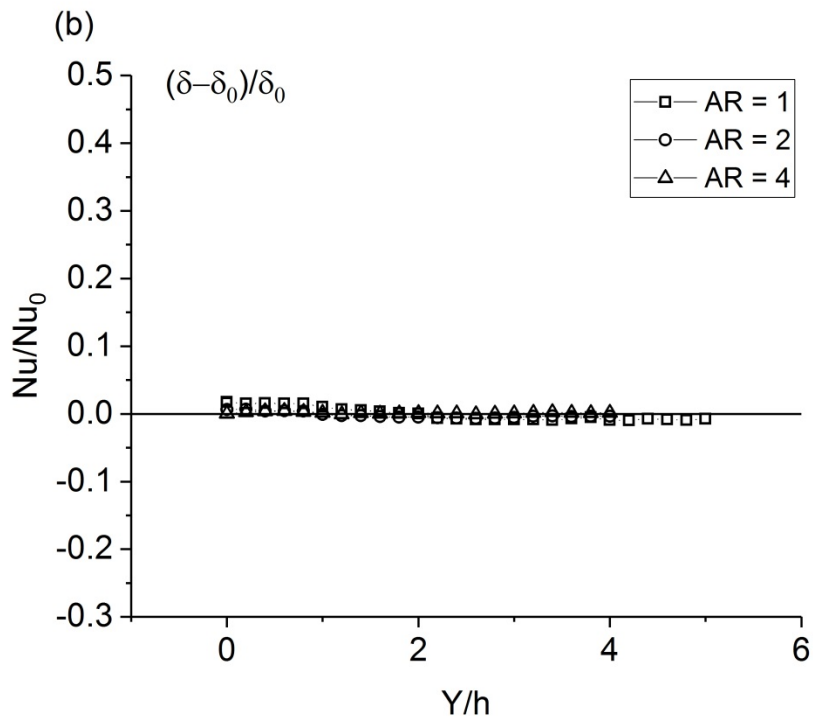
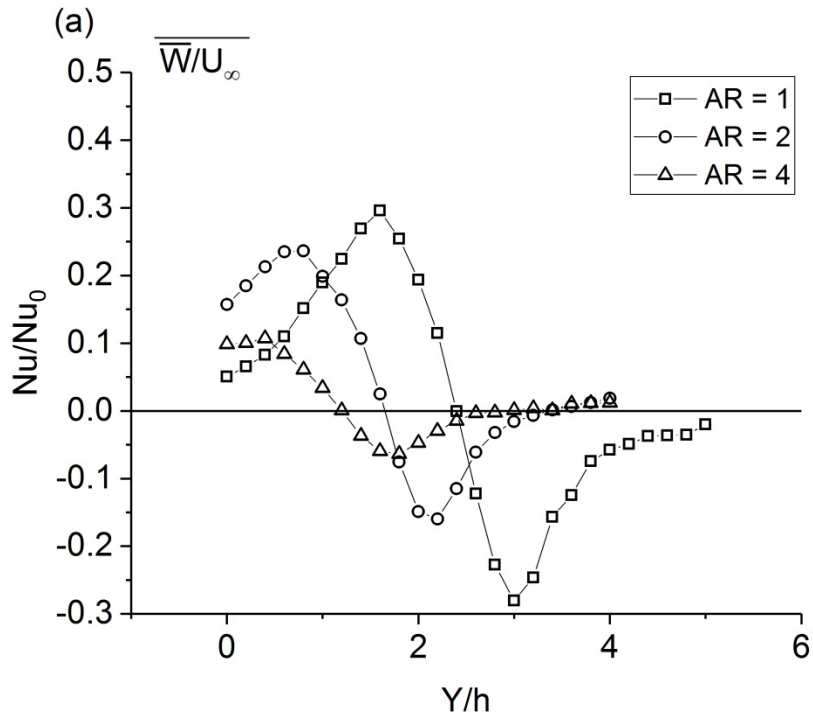


Figure A. 4 Comparison between calculated and measured Nusselt number. Lines signify calculated curves based on the data in chapter 4, and symbols are measured data.

Figure A.5 illustrates the impact of individual factors on the heat transfer performance. With the increasing aspect ratio, both the heat transfer enhancement and diminishment by out-of-plate (in-to-plate) velocity lessened. Both of the effects shift toward negative Y direction with the aspect ratio. No obvious impact from the boundary layer thickness can be seen. The enhancement by near-surface velocity decreases with the aspect ratio, while the diminishment remains the same. The enhancement by turbulence fluctuation drops dramatically with the aspect ratio. Thus the decrease of heat transfer enhancement with aspect ratio can be attributed to the decrease of in-to-plate velocity, near-surface velocity, and turbulence fluctuation. The increase of heat transfer diminishment with the aspect ratio is related to the significant drop caused by turbulence fluctuation, which outweighs the beneficial effect from decreasing out-of-plate velocity.



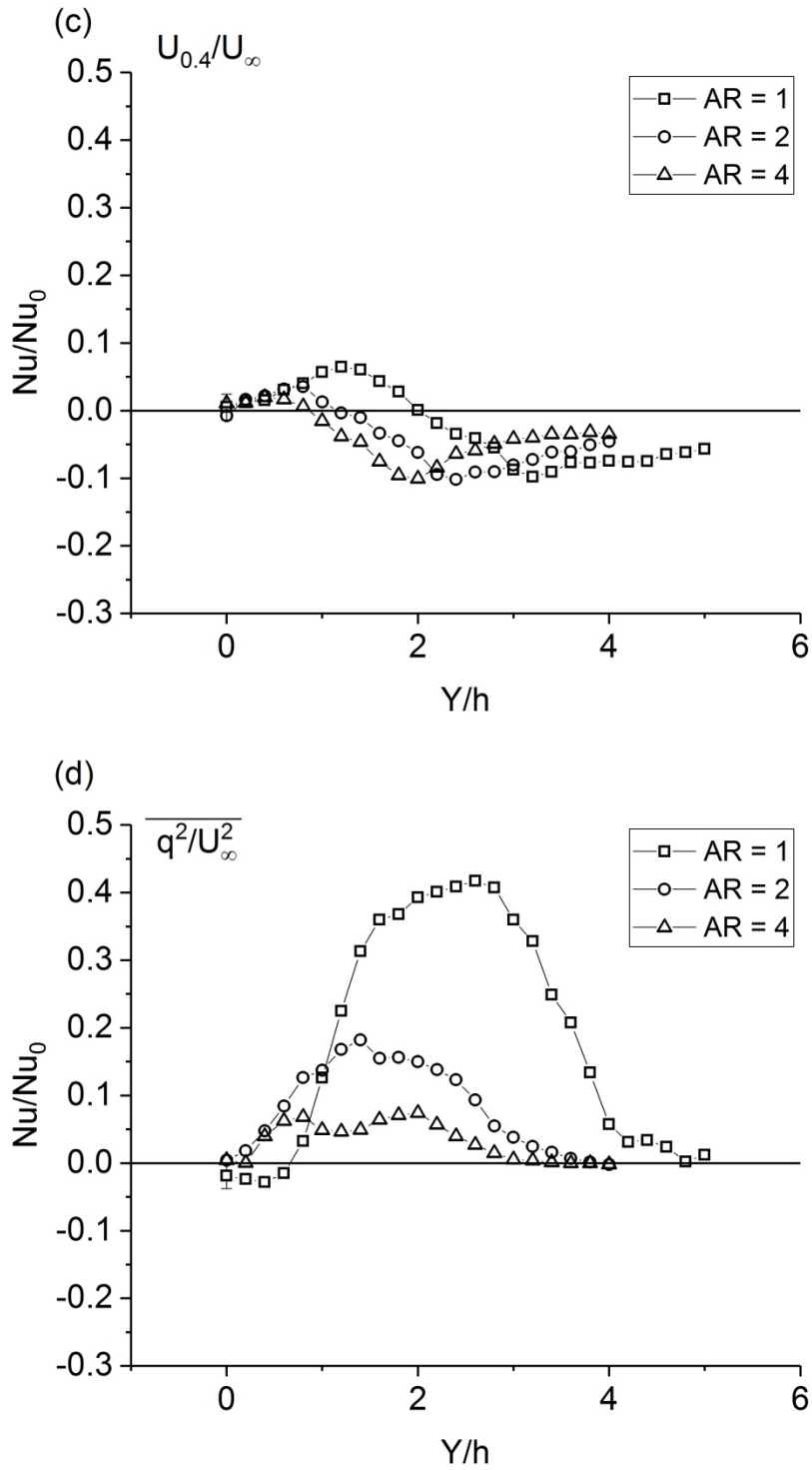


Figure A. 5 The impact of each factor on heat transfer for varying aspect ratio. (a) \overline{W}/U_∞ , (b) $(\delta - \delta_0)/\delta_0$, (c) $U_{0.4}/U_\infty$, (d) q^2/U_∞^2 .

Appendix B. Permissions for Previously Published Works

Chapter 3: An experimental study of turbulence flow behind a delta winglet

25/07/2017

RightsLink Printable License

ELSEVIER LICENSE TERMS AND CONDITIONS

Jul 25, 2017

This Agreement between Mr. Hao Wu ("You") and Elsevier ("Elsevier") consists of your license details and the terms and conditions provided by Elsevier and Copyright Clearance Center.

License Number	4156121423910
License date	Jul 25, 2017
Licensed Content Publisher	Elsevier
Licensed Content Publication	Experimental Thermal and Fluid Science
Licensed Content Title	An experimental study of turbulent flow behind a delta winglet
Licensed Content Author	Hao Wu,David S-K. Ting,Steve Ray
Licensed Content Date	Nov 1, 2017
Licensed Content Volume	88
Licensed Content Issue	n/a
Licensed Content Pages	9
Start Page	46
End Page	54
Type of Use	reuse in a thesis/dissertation
Portion	full article
Format	both print and electronic
Are you the author of this Elsevier article?	Yes
Will you be translating?	No
Title of your thesis/dissertation	Engineering Flow Turbulence for Transport Enhancement
Expected completion date	Aug 2017
Estimated size (number of pages)	150
Requestor Location	Mr. Hao Wu 531 Mill str-204 Windsor, ON N9C2R7 Canada Attn: Mr. Hao Wu
Total	0.00 USD
Terms and Conditions	

INTRODUCTION

1. The publisher for this copyrighted material is Elsevier. By clicking "accept" in connection with completing this licensing transaction, you agree that the following terms and conditions apply to this transaction (along with the Billing and Payment terms and conditions established by Copyright Clearance Center, Inc. ("CCC"), at the time that you opened your Rightslink account and that are available at <http://myaccount.copyright.com>).

GENERAL TERMS

2. Elsevier hereby grants you permission to reproduce the aforementioned material subject to the terms and conditions indicated.

<https://s100.copyright.com/AppDispatchServlet>

VITA AUCTORIS

NAME: Hao Wu

PLACE OF BIRTH: Yuncheng, Shaanxi, China

YEAR OF BIRTH 1993

EDUCATION: Xi'an Tie Yi High School, Xi'an, China,
2008-2011

Xi'an Jiaotong University, Xi'an, China,
2011-2015 B. Eng.

University of Windsor, Windsor, ON,
2015-2017 M. Sc.